Synthesis of weak acid polymers and investigation of electrical properties toward field-effect transistors (FETs)

ATHCHAYA SUWANSOONTORN

Japan Advanced Institute of Science and Technology

Doctoral Dissertation

Synthesis of weak acid polymers and investigation of electrical properties toward field-effect transistors (FETs)

ATHCHAYA SUWANSOONTORN

Supervisor: Associate Professor Yuki Nagao

Graduate School of Advanced Science and Technology
Japan Advanced Institute of Science and Technology
Materials Science

September 2021

General abstract

The investigation of proton transport is essential to explain the various biological systems, including interfacial proton transport. However, as commonly found in biomaterials, it is still unknown how carboxylic acid concentration affects interfacial proton conduction. A series of styrene-based polymers comprising of the carboxylic acid group were prepared to explore the effects of carboxylic acid group concentration on polymer thin films' electrical properties. The carboxylic acid group concentration influences the proton transport pathway of polymer thin film. The high concentration of carboxylic acid group polymer thin film provides an internal proton transport, while the low concentration of carboxylic acid group polymer thin film allows an interfacial proton transport. The studying of proton transport properties in field-effect transistors (FETs) is a promising candidate for bridging biological and electronic systems. The electrical properties' investigation in FETs without the effect of palladium (Pd) electrode reaction using an alternative (AC)-current is challenging. The FETs with parallel-shaped electrodes (PFETs) were successfully fabricated. The fabricated polymer with weak-acid functionalized and low water uptake ability was applied to the PFETs to examine the electrical properties of polymer thin film. However, the electrical response of polymer thin film was dominated by the electrode/ polymer thin film interfacial response due to the relatively low proton conductivity and high resistance of the fabricated polymer thin film. Therefore, the comb-shaped electrode FETs (CFETs) were developed with an extra-long channel width and short channel length. Without the dominated double layer capacitance response, the impedance response of polymer thin films on CFETs was successfully observed. This study overcomes the drawbacks of dominated double-layer capacitance response and the short circuit between two electrodes through the thin dielectric layer in the AC-impedance measurement method.

Keywords: Carboxylic acid; FETs; Interfacial proton transport; Internal proton transport; Impedance measurement

Table of contents

Page

List of figures

Figure **Page**

List of tables

Table **Page**

List of schemes

Scheme **Page**

Chapter 1

General information

1.1 Proton conductive polymers

Proton transport acts as an essential role in various systems, including biological systems. Since 1961, the proton transfer in protein ionic channels starts to attract much attention from researchers.[1] The proton transport in biological systems was investigated through the purple membrane, including bacteriorhodopsin.[2–11] Many researchers were interested and studied the proton transport at the lipid monolayer.[12–16] As one of the most well-known systems in living cells, the adenosine triphosphate (ATP) formation during photosynthesis also involves a proton translocation across a membrane, as shown in Figure 1.1.[17,18] Recently, proton translocation through the biomembrane surface was also reported.[19–22] The translocation of protons across biological membranes is also found in the proton pump, such as cytochrome c oxidase (CcO).[19,20] This information presents the importance of proton transport in various biological systems.

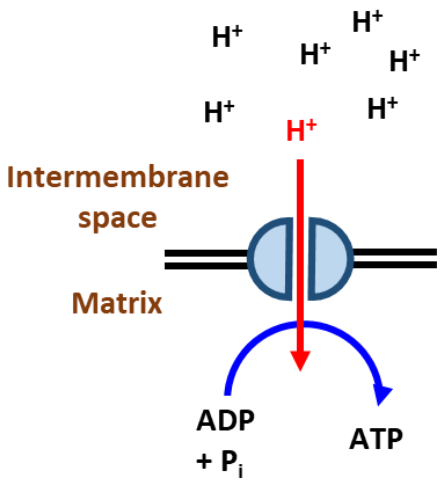

Figure 1.1 The adenosine triphosphate (ATP) synthase.[23]

Proton transport is one of the critical mechanisms of fuel cells as well as biological systems. For example, in the proton-exchange membrane fuel cells (PEMFCs), the proton movement between cathode and anode is the main part of power generation, as shown in Figure 1.2.[24] This PEMFC is a promising fuel cell for transportation and mobile applications due to its various advantages: good efficiency, high tolerance, and quick response to power demand.[24,25] During the operation, the hydrogen gas as a fuel is oxidized and produced protons at the anode catalyst layer. These produced protons are then transported to the cathode catalyst layer side through a proton exchange membrane. At the same time, the electrons move to the cathode side through the external circuit and react with oxygen gas and protons to produce water. Therefore, this PEMFC operation produces only water and heat without any pollution as byproducts.

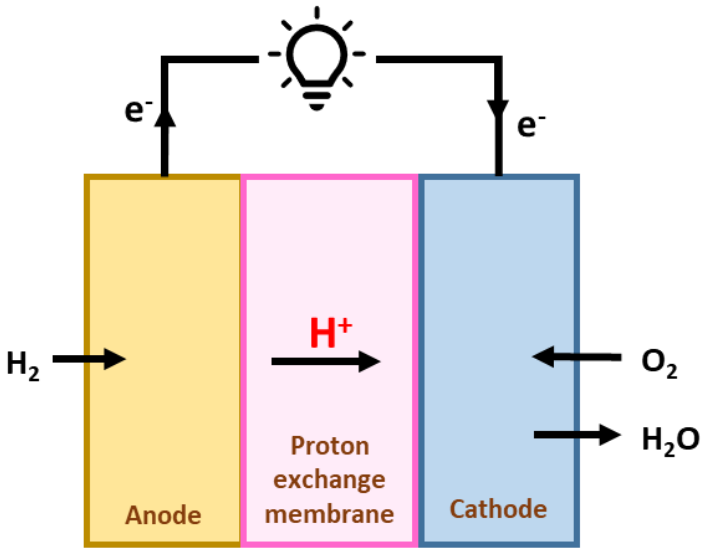

Figure 1.2 Schematic of a proton-exchange membrane fuel cell (PEMFC) operation.[24]

Many proton-conductive materials have been developed and studied to understand more insight and improve the performance of the proton transport mechanism. Because of its performance, efficiency, stability, and capacity to function at low temperatures, proton-conductive ceramics have been extensively studied.[26–28] Many polymers were also gained much attention as proton conductive material due to their high proton conductivity and good mechanical properties.[29–33]

Acids or proton-donating functional groups in proton conductive polymers, which can conduct protons over long distances, can provide free protons as the carrier to facilitate proton transport. Strong acids as derivatives of sulfonic acid were widely used due to their high deprotonation ability. For example, commercial Nafion™ and sulfonated poly(ether ether ketone) (SPEEK) which containing a sulfonic acid group in their structure (Figure 1.3). Especially Nafion ™, which have gained much attention and have been intensively studied due to their phase segregation between the hydrophilic sulfonic acid group side chain and hydrophobic backbone, and oriented structure.[34–40]

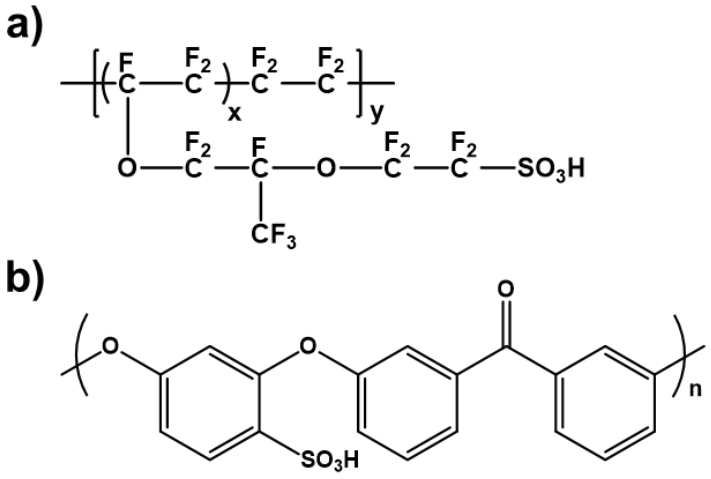

Figure 1.3 Chemical structure of commercial proton conductive polymers with a strong sulfonic acid functional group a) Nafion™ and b) SPEEK.

Many experiments using acid-base proton conductor combinations to promote proton transport in an anhydrous condition have been published.[41–47] Proton donors in this system are acid groups with low pK_a values since protons are easily dissociated. On the other hand, the basic groups operate as proton acceptors, allowing proton reception and release to continue the transportation process.[47] The effects of acid and base functional group concentration on the proton conductivity across protein biopolymers have been reported.[48,49]

The biopolymers, such as sugar and protein derivatives, also gain much attention for proton conductive materials. Figure 1.4 shows the chemical structure of biopolymers with polar

functional groups as carboxylic, amine, and hydroxyl that support the proton conduction: maleic chitosan and glutamic acid. According to Wang et al., adding amino acid functionalized nanofibers to a sulfonated poly(ether sulfone) (SPES) membrane improved proton conductivity.[50] Pena-Francesch et al. found that cephalopod proteins-based synthetic tandem repeat polypeptides show excellent proton conductivity and self-healing.[51] In this system, protons can transport across the hydrogen-bonding network between the biopolymer's hydrophilic residuals and water.[41,48,49,52–54] The high proton conductivity was reported in glycosaminoglycans with many acidic groups.[55] These hydrophilic biopolymers with many acidic groups may be able to form many hydrogen-bonding networks and support proton transport. The addition of hydroxyl, amine, and carboxylic acid functionalized carbon dots to bovine serum albumin (BSA)-mat improved proton conductivity.[48] On the other hand, hydrophobic substitution on carboxylic acid or amine functional groups of BSA protein mat prevents proton conduction.[49] This study supports the idea that the concentration of acid-base functional groups significantly impacts charge carrier density and proton conduction. However, biopolymers' proton conductivity is lower than polymers containing sulfonic acids since the hydrophilic residuals in biopolymers are weak acids with much higher pK_a than a strong acid. The high pK_a of weak acid directly affects the amount of proton carrier or proton carrier density of the conductive material. Although the proton conductivity of biopolymers containing weak acid groups is rarely comparable to polymers with strong acid groups, the study of proton transport in these weak acid-containing materials is necessary to understand the working mechanism in many biological systems.

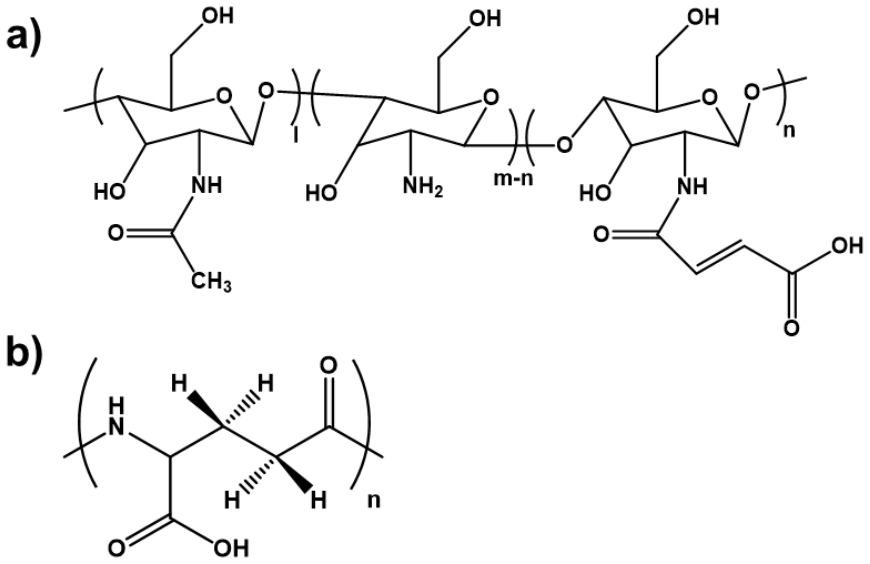

Figure 1.4 Chemical structure of biopolymer containing weak acid group (i.e., carboxylic acid) a) maleic chitosan and b) glutamic acid.

1.2 Field-effect transistors (FETs)

A field-effect transistor or FET is a transistor type that uses an external electric field to modulate charge carriers' flow between source and drain terminals.[56–58] A FET consists of 3 terminals, source, drain, and gate, as shown in Figure 1.5. An external electric field or gate voltage (V_G) can be applied through a gate terminal separated from the source and drain terminals by an insulator oxide layer. Due to its abilities in charge carriers flow controlled, FETs have been applied in many application fields. Many FETs were applied for biosensor applications due to their abundant advantages: high sensitivity, portability, near real-time response, and fabrication compatibility.[59–64] The graphene FET is one of the candidates for biomedical analysis such as influenza infection detection and drug discovery.[65] The surface-immobilized graphene can act as a cell surface and be used as a channel for graphene FETs. The graphene can also be used for small peptide or biomolecules detection.[65–67] The report of pH sensor based on graphene nanoplatelet and gold nanoparticle Hybrid was also published recently.[68] The ion-sensitive FETs (ISFETs) were developed for health monitoring flexible sensors which performance can be modulated through the bending of devices.[69] The metal–oxide–semiconductor (MOSFET) was widely used in digital and analog integrated circuits and power devices.[70–72]

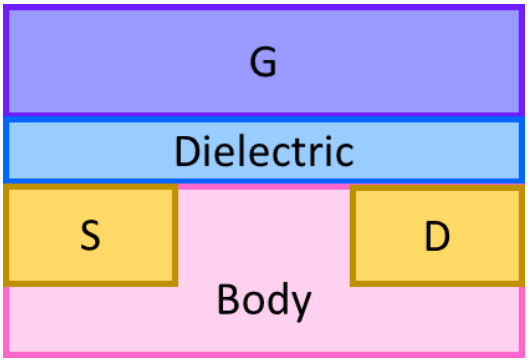

Figure 1.5 Cross-sectional view of a field-effect transistor. S, D, and G denote as the source, drain, and gate terminals, respectively.

Organic FETs (OFETs) are one type of FETs that received much attention due to their various advantages: low-temperature deposition, low cost, good solution processability, and possible to be fabricated on flexible substrates as displays, electronic papers, and sensors.[73,74] OFETs consist of an organic semiconducting part, an insulator layer, and three electrode terminals.[75] In OFET fabrication, the thin semiconducting layer can be fabricated through vacuum evaporation, thin-film alignment, or liquid deposition (spin-coating, drop-casting, printing, meniscus-guided coating).[74,76]

There are four different types of OFETs, as shown in Figure 1.6.[75] A bottom gate/ bottom contact has a semiconductor material placed on the top. A bottom gate/ top contact has a semiconductor material between the insulator layer and source-drain electrodes. A top gate/ top contact has a semiconductor material as the lowest layer. A top gate/ bottom contact has a semiconductor material between the insulator layer and source-drain as the bottom gate/ top contact type, but the insulator layer and gate terminal locate at the top of the device. However, even though their configurations are different, the insulator layer always separates the source and drain terminals from the gate terminal, and the semiconducting layer must contact the source and drain terminals.

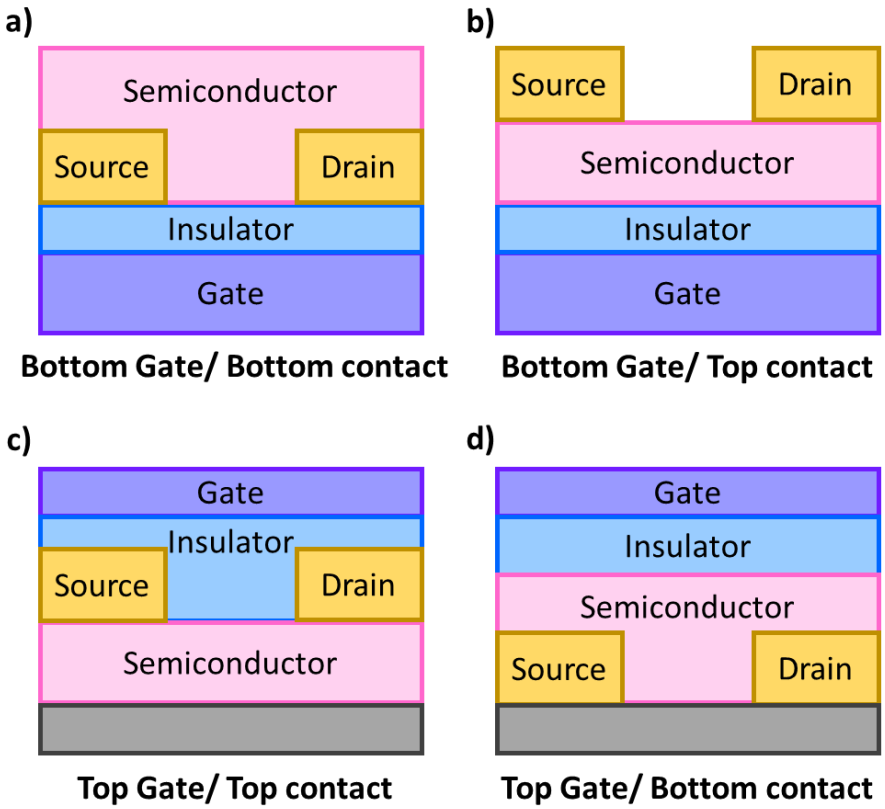

Figure 1.6 The different types of OFETs. a) Bottom gate/ bottom contact, b) Bottom gate/ top contact, c) top gate/ top contact, and d) Top gate/ bottom contact.[75]

With this structure configuration of OFETs that source and drain terminal separated from gate terminal by an insulator, the ion conductivity can be modulated in these devices through an external applied voltage. For example, when a negative V_G is applied to OFET with proton conductive material, proton carriers are attracted to the semiconductor and dielectric or insulator layer interface. Thus, as the negative voltage increases, proton concentration at the interface becomes higher and increases the current between source and drain.

In contrast, the positive V_G repels proton carriers from the interface, reduces the source and drain current. With this mechanism, the current flow can be manipulated through the external electric field application or applied V_G, as shown in Figure 1.7. Nevertheless, the charge conduction occurs at the organic semiconductor-dielectric layer interface or the thickness region of only ~10 nm.[77–79]

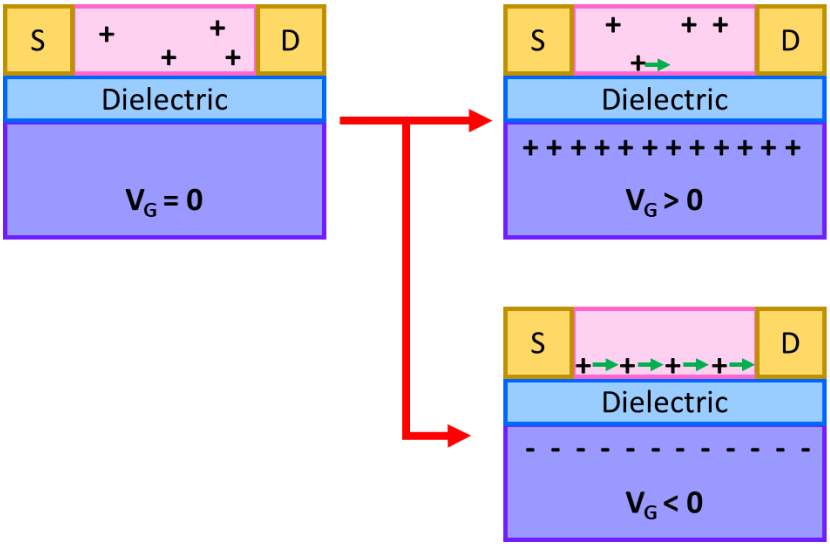

Figure 1.7 Schematic of the interfacial charge carrier concentration in a bottom gate/ bottom contact OFET with proton conductive material modulated by positive and negative V_G (+, proton or positive charge; -, electron or negative charge).

Due to the ability to modulate ion conductivity, the working mechanism of OFET with various materials was extensively investigated.[80–84] In OFETs, many parameters can affect the device's performance. Charge carrier mobility is one of the most important factors. The charge carrier mobility represents the carrier's ability to move through the material, which determines the electrical performance of the device.[85] Another essential parameter is charge carrier density which refers to the number of charge carriers. The charge carrier density also affects conductivity and the device's performance since it influences the charge carrier mobility and charge carrier transport.[86,87]

Much research studied and reported on the electronic properties of OFETs. For example, the ON/ OFF ratio in OFETs was often mentioned since the charge carrier mobility in OFETs can be modulated through an applied gate voltage (V_G). Zhong and co-workers claimed that negative V_G results in enhancing S-D current (I_{DS}), or ON state, of a polysaccharide protonic FET (H^+-FET). At the same time, positive V_G decreases the I_{DS} into an almost OFF state.[77] The I_{DS} modulation with the applied V_G was also reported in porous organic polymer membranes and metal-organic frameworks (MOF) with protons as a charge

carrier.[88,89] Like other FETs with a positive charge carrier, a negative V_G increases the I_{DS} while a positive V_G decreases the $I_{DS.}$

In contrast, the FETs with negative charge carriers show the opposite trend of I_{DS} modulated with V_G. A negative V_G decreases the $I_{DS,}$ while a positive V_G enhances the I_{DS}.[53] The above information indicates that an applied V_G can control the flow of charge carriers in the organic semiconducting material of OFETs.

Protonic FETs or H^+-FETs are one type of FET in which protons are the charge carrier, and the proton carrier transport can be modulated through an external applied voltage. The study of the protonic conductor also received much attention for the proton transport investigation in biological systems. Zhong et al. fabricated a maleic-chitosan nanofibers H^+-FET which an applied potential can control the protonic current.[77] The H^+-FET with a cephalopod protein was reported.[54] The report of porous organic polymer membrane and H^+-FET combination was also published.[88] The bionic FETs, which mimicked real biosystems, were built to study the working mechanism in biosystems.[89] However, most H^+-FET used palladium as electrode metal material under direct current (DC) conditions for relatively low proton conductivity materials because palladium can react with hydrogen and produce extra protons under hydrogen atmosphere.[53,88–90] In this case, the effect of extra protons on the material's proton conductivity and transport properties cannot be prevented. Therefore, the development of proton transport properties investigation in protonic FETs using alternative current (AC) conditions is challenging.

1.3 Purpose

This research mainly aims to synthesize polymers with defined weak acid concentrations and use them as proton conductive materials in H^+-FET. The purpose of this research can be divided into two parts, as follows:

1. To synthesize a series of styrene-based copolymers containing various weak carboxylic acid concentrations and investigate as proton conductive polymers.
2. To develop the ion conduction of synthesized weak acid polymer thin films in device with FETs electrode shape, cooperated with gold electrodes and AC impedance measurement to prevent the effect of electrode reaction.

1.4 Outlines

In chapter 1, the general background of proton conductive polymers and field-effect transistors (FETs) were explained.

In chapter 2, the polymers containing various carboxylic acid concentrations were successfully synthesized and characterized. The fabricated polymers were prepared as thin films and investigated as proton conductive materials. The electrical properties of polymer thin films were investigated, as shown in Figure 1.8. The difference in carboxylic acid concentrations was found to influence polymer thin films' main proton transport pathway.

In chapter 3, devices with a parallel-shaped channel (PFETs) were fabricated for in-plane proton conductivity measurement by the alternative circuit (AC)-impedance measurement, as shown in Figure 1.8. The gold was sputtered on the silicon wafer (Si-wafer) surface and acted as electrodes. The fabricated polymers from Chapter 2 were prepared as a thin film on the PFETs. The AC impedance measurement was performed to evaluate the proton transport in PFETs to avoid the electrode reaction.

In chapter 4, a new design of comb-shaped electrodes (CFETs) for the AC-impedance measurement method has been designed to improve the impedance response. The ionic conductivity of polymer thin film with relatively low conductivity using these improved CFETs was investigated, as shown in Figure 1.8.

In chapter 5, the general conclusion was presented. The finding of this research was expected to provide more insight into the influence of weak-acid group concentration of polymer on the proton conduction pathway in thin films. Moreover, the newly developed CFETs were expected to be applied for the AC-impedance measurement of relatively low proton conductivity polymer thin films.

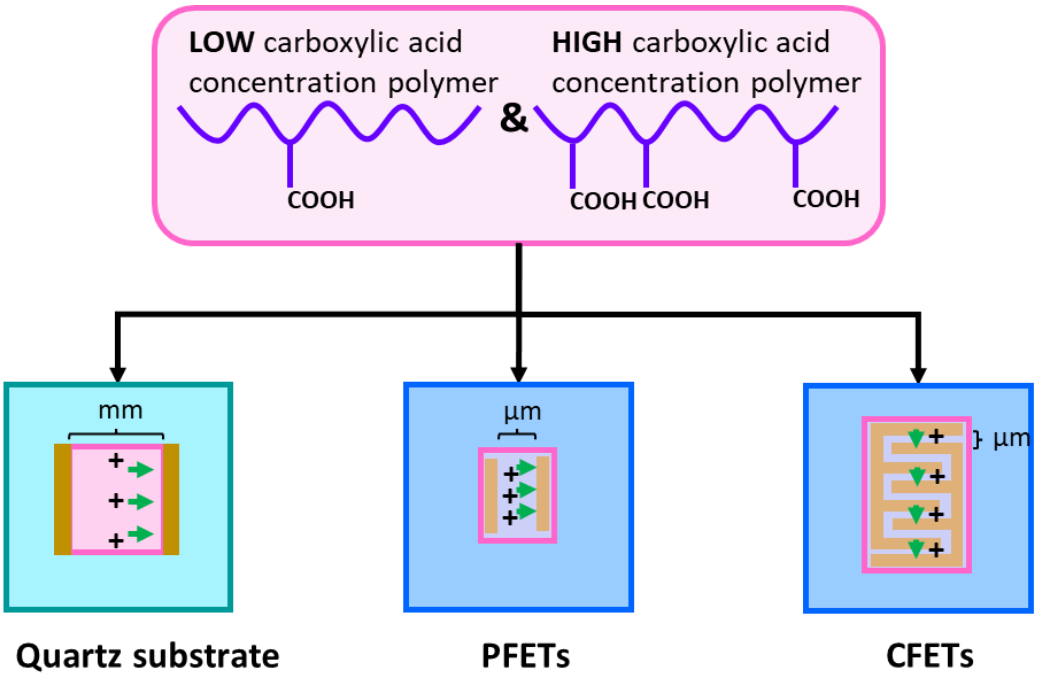

Figure 1.8 The schematic represents the research strategies.

References

(1) MITCHELL, P. Coupling of Phosphorylation to Electron and Hydrogen Transfer by a Chemi-Osmotic Type of Mechanism. *Nature* **1961**, *191* (4784), 144–148. https://doi.org/10.1038/191144a0.

(2) Váró, G.; Keszthelyi, L. Photoelectric Signals from Dried Oriented Purple Membranes of Halobacterium Halobium. *Biophys. J.* **1983**, *43* (1), 47–51. https://doi.org/10.1016/S0006-3495(83)84322-7.

(3) Butt, H. J.; Fendler, K.; Bamberg, E.; Tittor, J.; Oesterhelt, D. Aspartic Acids 96 and 85 Play a Central Role in the Function of Bacteriorhodopsin as a Proton Pump. *EMBO J.* **1989**, *8* (6), 1657–1663. https://doi.org/10.1002/j.1460-2075.1989.tb03556.x.

(4) Krimm, S.; Dwivedi, A. M. Infrared Spectrum of the Purple Membrane: Clue to a Proton Conduction Mechanism? *Science* **1982**, *216* (4544), 407–408. https://doi.org/10.1126/science.6280277.

(5) Lozier, R. H.; Bogomolni, R. A.; Stoeckenius, W. Bacteriorhodopsin: A Light-Driven Proton Pump in Halobacterium Halobium. *Biophys. J.* **1975**, *15* (9), 955–962. https://doi.org/10.1016/S0006-3495(75)85875-9.

(6) Nachliel, E.; Gutman, M.; Kiryati, S.; Dencher, N. A. Protonation Dynamics of the Extracellular and Cytoplasmic Surface of Bacteriorhodopsin in the Purple Membrane. *Proc. Natl. Acad. Sci. U. S. A.* **1996**, *93* (20), 10747–10752. https://doi.org/10.1073/pnas.93.20.10747.

(7) Needleman, R.; Chang, M.; Ni, B.; Váró, G.; Fornés, J.; White, S. H.; Lanyi, J. K. Properties of Asp212—-Asn Bacteriorhodopsin Suggest That Asp212 and Asp85 Both Participate in a Counterion and Proton Acceptor Complex near the Schiff Base. *J. Biol. Chem.* **1991**, *266* (18), 11478–11484. https://doi.org/10.1016/S0021-9258(18)98982-9.

(8) Racker, E.; Stoeckenius, W. Reconstitution of Purple Membrane Vesicles Catalyzing Light-Driven Proton Uptake and Adenosine Triphosphate Formation. *J. Biol. Chem.*

1974, *249* (2), 662–663. https://doi.org/10.1016/S0021-9258(19)43080-9.

(9) Tittor, J.; Schweiger, U.; Oesterhelt, D.; Bamberg, E. Inversion of Proton Translocation in Bacteriorhodopsin Mutants D85N, D85T, and D85,96N. *Biophys. J.* **1994**, *67* (4), 1682–1690. https://doi.org/10.1016/S0006-3495(94)80642-3.

(10) Trissl, H. W. Photoelectric Measurements of Purple Membranes. *Photochem. Photobiol.* **1990**, *51* (6), 793–818. https://doi.org/10.1111/php.1990.51.6.793.

(11) Dér, A.; Száraz, S.; Tóth-Boconádi, R.; Tokaji, Z.; Keszthelyi, L.; Stoeckenius, W. Alternative Translocation of Protons and Halide Ions by Bacteriorhodopsin. *Proc. Natl. Acad. Sci. U. S. A.* **1991**, *88* (11), 4751–4755. https://doi.org/10.1073/pnas.88.11.4751.

(12) Sakurai, I.; Kawamura, Y. Lateral Electrical Conduction along a Phosphatidylcholine Monolayer. *Biochim. Biophys. Acta - Biomembr.* **1987**, *904* (2), 405–409. https://doi.org/10.1016/0005-2736(87)90391-9.

(13) Teissié, J.; Prats, M.; Soucaille, P.; Tocanne, J. F. Evidence for Conduction of Protons along the Interface between Water and a Polar Lipid Monolayer. *Proc. Natl. Acad. Sci.* **1985**, *82* (10), 3217 LP – 3221. https://doi.org/10.1073/pnas.82.10.3217.

(14) Morgan, H.; Martin Taylor, D.; Oliveira, O. N. Proton Transport at the Monolayer-Water Interface. *Biochim. Biophys. Acta - Biomembr.* **1991**, *1062* (2), 149–156. https://doi.org/10.1016/0005-2736(91)90386-M.

(15) Polle, A.; Junge, W. Proton Diffusion along the Membrane Surface of Thylakoids Is Not Enhanced over That in Bulk Water. *Biophys. J.* **1989**, *56* (1), 27–31. https://doi.org/10.1016/S0006-3495(89)82649-9.

(16) Leberle, K.; Kempf, I.; Zundel, G. An Intramolecular Hydrogen Bond with Large Proton Polarizability within the Head Group of Phosphatidylserine. An Infrared Investigation. *Biophys. J.* **1989**, *55* (4), 637–648. https://doi.org/10.1016/S0006-3495(89)82861-9.

(17) Kreuer, K. D. Proton Conductivity: Materials and Applications. *Chem. Mater.* **1996**, *8*

(3), 610–641. https://doi.org/10.1021/cm950192a.

(18) Godbey, W. T. Chapter 3 - Cellular Transport; Godbey, W. T. B. T.-A. I. to B., Ed.; Woodhead Publishing, 2014; pp 35–64. https://doi.org/10.1016/B978-1-907568-28-2.00003-4.

(19) Georgievskii, Y.; Medvedev, E. S.; Stuchebrukhov, A. A. Proton Transport via the Membrane Surface. *Biophys. J.* **2002**, *82* (6), 2833–2846. https://doi.org/10.1016/S0006-3495(02)75626-9.

(20) Blomberg, M. R. A.; Siegbahn, P. E. M. Different Types of Biological Proton Transfer Reactions Studied by Quantum Chemical Methods. *Biochim. Biophys. Acta - Bioenerg.* **2006**, *1757* (8), 969–980. https://doi.org/10.1016/j.bbabio.2006.01.002.

(21) Amdursky, N.; Lin, Y.; Aho, N.; Groenhof, G. Exploring Fast Proton Transfer Events Associated with Lateral Proton Diffusion on the Surface of Membranes. *Proc. Natl. Acad. Sci. U. S. A.* **2019**, *116* (7), 2443–2451. https://doi.org/10.1073/pnas.1812351116.

(22) Agam, Y.; Nandi, R.; Bulava, T.; Amdursky, N. The Role of the Protein-Water Interface in Dictating Proton Conduction across Protein-Based Biopolymers. *Mater. Adv.* **2021**, 1739–1746. https://doi.org/10.1039/d0ma00951b.

(23) Schäfer, G.; Engelhard, M.; Müller, V. Bioenergetics of the Archaea. *Microbiol. Mol. Biol. Rev.* **1999**, *63* (3), 570–620. https://doi.org/10.1128/MMBR.63.3.570-620.1999.

(24) Zuo, Z.; Fu, Y.; Manthiram, A. Novel Blend Membranes Based on Acid-Base Interactions for Fuel Cells. *Polymers (Basel).* **2012**, *4* (4), 1627–1644. https://doi.org/10.3390/polym4041627.

(25) Shao, Y.; Yin, G.; Wang, Z.; Gao, Y. Proton Exchange Membrane Fuel Cell from Low Temperature to High Temperature: Material Challenges. *J. Power Sources* **2007**, *167* (2), 235–242. https://doi.org/10.1016/j.jpowsour.2007.02.065.

(26) Le, L. Q.; Hernandez, C. H.; Rodriguez, M. H.; Zhu, L.; Duan, C.; Ding, H.; O'Hayre,

R. P.; Sullivan, N. P. Proton-Conducting Ceramic Fuel Cells: Scale up and Stack Integration. *J. Power Sources* **2021**, *482* (August 2020), 228868. https://doi.org/10.1016/j.jpowsour.2020.228868.

(27) Duan, C.; Kee, R.; Zhu, H.; Sullivan, N.; Zhu, L.; Bian, L.; Jennings, D.; O'Hayre, R. Highly Efficient Reversible Protonic Ceramic Electrochemical Cells for Power Generation and Fuel Production. *Nat. Energy* **2019**, *4* (3), 230–240. https://doi.org/10.1038/s41560-019-0333-2.

(28) Meng, Y.; Gao, J.; Zhao, Z.; Amoroso, J.; Tong, J.; Brinkman, K. S. Review: Recent Progress in Low-Temperature Proton-Conducting Ceramics. *J. Mater. Sci.* **2019**, *54* (13), 9291–9312. https://doi.org/10.1007/s10853-019-03559-9.

(29) Ranjeesh, K. C.; Illathvalappil, R.; Veer, S. D.; Peter, J.; Wakchaure, V. C.; Goudappagouda; Raj, K. V.; Kurungot, S.; Babu, S. S. Imidazole-Linked Crystalline Two-Dimensional Polymer with Ultrahigh Proton-Conductivity. *J. Am. Chem. Soc.* **2019**, *141* (38), 14950–14954. https://doi.org/10.1021/jacs.9b06080.

(30) Zuo, P.; Li, Y.; Wang, A.; Tan, R.; Liu, Y.; Liang, X.; Sheng, F.; Tang, G.; Ge, L.; Wu, L.; et al. Sulfonated Microporous Polymer Membranes with Fast and Selective Ion Transport for Electrochemical Energy Conversion and Storage. *Angew. Chemie - Int. Ed.* **2020**, *59* (24), 9564–9573. https://doi.org/10.1002/anie.202000012.

(31) Kim, S.; Kwon, M. S.; Han, J. H.; Yuk, J.; Lee, J. Y.; Lee, K. T.; Kim, T. H. Poly(Ethylene-Co-Vinyl Acetate)/Polyimide/Poly(Ethylene-Co-Vinyl Acetate) Tri-Layer Porous Separator with High Conductivity and Tailored Thermal Shutdown Function for Application in Sodium-Ion Batteries. *J. Power Sources* **2021**, *482* (July 2020). https://doi.org/10.1016/j.jpowsour.2020.228907.

(32) Li, Z.; Liu, Z.; Li, H.; Hasan, M.; Suwansoontorn, A.; Du, G.; Wang, D.; Zhang, Y.; Nagao, Y. Sulfonated Triazine-Based Porous Organic Polymers for Excellent Proton Conductivity. *ACS Appl. Polym. Mater.* **2020**, *2* (8), 3267–3273. https://doi.org/10.1021/acsapm.0c00425.

(33) Li, Z.; Yao, Y.; Wang, D.; Hasan, M. M.; Suwansoontorn, A.; Li, H.; Du, G.; Liu, Z.; Nagao, Y. Simple and Universal Synthesis of Sulfonated Porous Organic Polymers with High Proton Conductivity. *Mater. Chem. Front.* **2020**, *4* (8), 2339–2345. https://doi.org/10.1039/D0QM00276C.

(34) Nagao, Y. Proton-Conductivity Enhancement in Polymer Thin Films. *Langmuir* **2017**, *33* (44), 12547–12558. https://doi.org/10.1021/acs.langmuir.7b01484.

(35) Bass, M.; Berman, A.; Singh, A.; Konovalov, O.; Freger, V. Surface-Induced Micelle Orientation in Nafion Films. *Macromolecules* **2011**, *44* (8), 2893–2899. https://doi.org/10.1021/ma102361f.

(36) Ono, Y.; Nagao, Y. Interfacial Structure and Proton Conductivity of Nafion at the Pt-Deposited Surface. *Langmuir* **2016**, *32* (1), 352–358. https://doi.org/10.1021/acs.langmuir.5b02623.

(37) Nagao, Y.; Enta, A.; Suwansoontorn, A.; Ono, Y. Proton Conductivity and Oriented Structure of Nafion Thin Films on the Au-Deposited Surface and MgO Substrate. *ECS Trans.* **2018**, *88* (1), 249–258. https://doi.org/10.1149/08801.0249ecst.

(38) Kusoglu, A.; Weber, A. Z. New Insights into Perfluorinated Sulfonic-Acid Ionomers. *Chem. Rev.* **2017**, *117* (3), 987–1104. https://doi.org/10.1021/acs.chemrev.6b00159.

(39) Krishnan, K.; Iwatsuki, H.; Hara, M.; Nagano, S.; Nagao, Y. Influence of Molecular Weight on Molecular Ordering and Proton Transport in Organized Sulfonated Polyimide Thin Films. *J. Phys. Chem. C* **2015**, *119* (38), 21767–21774. https://doi.org/10.1021/acs.jpcc.5b03292.

(40) Nagao, Y. Highly Oriented Sulfonic Acid Groups in a Nafion Thin Film on Si Substrate. *J. Phys. Chem. C* **2013**, *117* (7), 3294–3297. https://doi.org/10.1021/jp311622p.

(41) Tsuksamoto, M.; Ebata, K.; Sakiyama, H.; Yamamoto, S.; Mitsuishi, M.; Miyashita, T.; Matsui, J. Biomimetic Polyelectrolytes Based on Polymer Nanosheet Films and Their Proton Conduction Mechanism. *Langmuir* **2019**, *35* (9), 3302–3307. https://doi.org/10.1021/acs.langmuir.8b04079.

(42) Nagao, Y.; Naito, N.; Iguchi, F.; Sata, N.; Yugami, H. Synthesis of Oligomeric Poly [(1 , 2-Propanediamine) - Alt - (Oxalic Acid)] and Anomalous Proton Conductivities of the Thin Fi Lms. *Solid State Ionics* **2009**, *180* (6–8), 589–591. https://doi.org/10.1016/j.ssi.2008.09.022.

(43) Li, Q.; Jensen, J. O.; Savinell, R. F.; Bjerrum, N. J. High Temperature Proton Exchange Membranes Based on Polybenzimidazoles for Fuel Cells. *Prog. Polym. Sci.* **2009**, *34* (5), 449–477. https://doi.org/10.1016/j.progpolymsci.2008.12.003.

(44) Yang, C.; Costamagna, P.; Srinivasan, S.; Benziger, J.; Bocarsly, A. B. Approaches and Technical Challenges to High Temperature Operation of Proton Exchange Membrane Fuel Cells. *J. Power Sources* **2001**, *103* (1), 1–9. https://doi.org/10.1016/S0378-7753(01)00812-6.

(45) Greaves, T. L.; Drummond, C. J. Protic Ionic Liquids: Properties and Applications. *Chem. Rev.* **2008**, *108* (1), 206–237. https://doi.org/10.1021/cr068040u.

(46) Nagao, Y.; Haneda, A.; Naito, N.; Iguchi, F.; Sata, N.; Yugami, H. Synthesis and Protonic Conductivity of the Oligomeric Amides with Different Average Molecular Weights. *Solid State Ionics* **2008**, *179*, 1142–1145. https://doi.org/10.1016/j.ssi.2008.01.051.

(47) Huang, H.; Nia, L.; Xu, S.; Luo, F.; Fan, J.; Li, H.; Wang, H. Novel Proton Exchange Membrane with Long-Range Acid–Base-Pair Proton Transfer Pathways Based on Functionalized Polyethyleneimine. *ACS Sustain. Chem. Eng.* **2021**, *9* (10), 3963–3974. https://doi.org/10.1021/acssuschemeng.1c00154.

(48) Mondal, S.; Agam, Y.; Amdursky, N. Enhanced Proton Conductivity across Protein Biopolymers Mediated by Doped Carbon Nanoparticles. *Small* **2020**, *2005526* (16), 2005526. https://doi.org/10.1002/smll.202005526.

(49) Mondal, S.; Agam, Y.; Nandi, R.; Amdursky, N. Exploring Long-Range Proton Conduction, the Conduction Mechanism and Inner Hydration State of Protein Biopolymers. *Chem. Sci.* **2020**, *11* (13), 3547–3556.

https://doi.org/10.1039/c9sc04392f.

(50) Wang, H.; Ma, Y.; Cheng, B.; Kang, W.; Li, X.; Shi, L.; Cai, Z.; Zhuang, X. Solution Blown Biofunctionalized Poly(Vinylidene Fluoride) Nanofibers for Application in Proton Exchange Membrane Fuel Cells. *Electrochim. Acta* **2017**, *258*, 24–33. https://doi.org/10.1016/j.electacta.2017.10.071.

(51) Pena-Francesch, A.; Jung, H.; Hickner, M. A.; Tyagi, M.; Allen, B. D.; Demirel, M. C. Programmable Proton Conduction in Stretchable and Self-Healing Proteins. *Chem. Mater.* **2018**, *30* (3), 898–905. https://doi.org/10.1021/acs.chemmater.7b04574.

(52) Sato, T.; Tsukamoto, M.; Yamamoto, S.; Mitsuishi, M.; Miyashita, T.; Nagano, S.; Matsui, J. Acid-Group-Content-Dependent Proton Conductivity Mechanisms at the Interlayer of Poly(N-Dodecylacrylamide-Co-Acrylic Acid) Copolymer Multilayer Nanosheet Films. *Langmuir* **2017**, *33* (45), 12897–12902. https://doi.org/10.1021/acs.langmuir.7b03160.

(53) Deng, Y.; Josberger, E.; Jin, J.; Rousdari, A. F.; Helms, B. A.; Zhong, C.; Anantram, M. P.; Rolandi, M. H + -Type and OH - -Type Biological Protonic Semiconductors and Complementary Devices. *Sci. Rep.* **2013**, *3*. https://doi.org/10.1038/srep02481.

(54) Ordinario, D. D.; Phan, L.; Van Dyke, Y.; Nguyen, T.; Smith, A. G.; Nguyen, M.; Mofid, N. M.; Dao, M. K.; Gorodetsky, A. A. Photochemical Doping of Protonic Transistors from a Cephalopod Protein. *Chem. Mater.* **2016**, *28* (11), 3703–3710. https://doi.org/10.1021/acs.chemmater.6b00336.

(55) Selberg, J.; Jia, M.; Rolandi, M. Proton Conductivity of Glycosaminoglycans. *PLoS One* **2019**, *14* (3), 1–8. https://doi.org/10.1371/journal.pone.0202713.

(56) Kinik, F. P.; Kampouri, S.; Ebrahim, F. M.; Valizadeh, B.; Stylianou Molecular Sciences and Chemical Engineering, K. C. B. T.-R. M. in C. Porous Metal-Organic Frameworks for Advanced Applications; Elsevier, 2020. https://doi.org/10.1016/B978-0-08-102688-5.00011-8.

(57) Porkovich, A. J.; Danielson, E. 8 - Cluster Decoration of Semiconductor

Nanostructures toward Gas Sensors and Biosensors. In *Cluster Beam Deposition of Functional Nanomaterials and Devices*; Milani, P., Sowwan, M. B. T.-F. of N., Eds.; Elsevier, 2020; Vol. 15, pp 215–246. https://doi.org/10.1016/B978-0-08-102515-4.00008-8.

(58) Amal, H.; Haick, H. Chapter 14 - Point of Care Breath Analysis Systems. In *Micro and Nano Technologies*; Llobet, E. B. T.-A. N. for I. G. M., Ed.; Elsevier, 2020; pp 315–334. https://doi.org/10.1016/B978-0-12-814827-3.00014-1.

(59) Liang, Y.; Xiao, M.; Wu, D.; Lin, Y.; Liu, L.; He, J.; Zhang, G.; Peng, L.-M.; Zhang, Z. Wafer-Scale Uniform Carbon Nanotube Transistors for Ultrasensitive and Label-Free Detection of Disease Biomarkers. *ACS Nano* **2020**. https://doi.org/10.1021/acsnano.0c03523.

(60) Kwon, J.; Lee, Y.; Lee, T.; Ahn, J.-H. Aptamer-Based Field-Effect Transistor for Detection of Avian Influenza Virus in Chicken Serum. *Anal. Chem.* **2020**, *92* (7), 5524–5531. https://doi.org/10.1021/acs.analchem.0c00348.

(61) Zafar, S.; Lu, M.; Jagtiani, A. Comparison between Field Effect Transistors and Bipolar Junction Transistors as Transducers in Electrochemical Sensors. *Sci. Rep.* **2017**, *7* (January). https://doi.org/10.1038/srep41430.

(62) Cui, Y.; Wei, Q.; Park, H.; Lieber, C. M. Nanowire Nanosensors for Highly Sensitive and Selective Detection of Biological and Chemical Species. *Science (80-.).* **2001**, *293* (5533), 1289–1292. https://doi.org/10.1126/science.1062711.

(63) Zhang, A.; Lieber, C. M. Nano-Bioelectronics. *Chem. Rev.* **2016**, *116* (1), 215–257. https://doi.org/10.1021/acs.chemrev.5b00608.

(64) Chen, X.; Zhou, G.; Mao, S.; Chen, J. Rapid Detection of Nutrients with Electronic Sensors: A Review. *Environ. Sci. Nano* **2018**, *5* (4), 837–862. https://doi.org/10.1039/c7en01160a.

(65) Ono, T.; Kanai, Y.; Ohno, Y.; Maehashi, K.; Inoue, K.; Matsumoto, K. Electrical Biosensor Using Graphene Field-Effect Transistor and Small Receptor Molecules;

2020; pp 91–101. https://doi.org/10.1007/978-981-15-7610-2_5.

(66) Ushiba, S.; Miyakawa, N.; OKINO, T.; SHINAGAWA, A.; OKA, Y.; KIMURA, M.; ONO, T.; KANAI, Y.; INOUE, K.; MATSUMOTO, K. Biosensing Platforms Based on Graphene Field Effect Transistors. *Vac. Surf. Sci.* **2020**, *63*, 358–363. https://doi.org/10.1380/vss.63.358.

(67) Ono, T.; Kanai, Y.; Inoue, K.; Watanabe, Y.; Nakakita, S.; Kawahara, T.; Suzuki, Y.; Matsumoto, K. Electrical Biosensing at Physiological Ionic Strength Using Graphene Field-Effect Transistor in Femtoliter Microdroplet. *Nano Lett.* **2019**, *19*. https://doi.org/10.1021/acs.nanolett.9b01335.

(68) Medhat, A.; Salah, D.; Boichuk, N.; Hassan, I.; Vitusevich, S.; Kasry, A. Graphene Nanoplatelet-Au Nanoparticle Hybrid as a Capacitive-Metal-Oxide-Semiconductor PH Sensor. *ACS Appl. Electron. Mater.* **2021**, *3* (1), 430–436. https://doi.org/10.1021/acsaelm.0c00968.

(69) Vilouras, A.; Christou, A.; Manjakkal, L.; Dahiya, R. Ultrathin Ion-Sensitive Field-Effect Transistor Chips with Bending-Induced Performance Enhancement. *ACS Appl. Electron. Mater.* **2020**, *2* (8), 2601–2610. https://doi.org/10.1021/acsaelm.0c00489.

(70) Roshini, C.; Inbaraj, P.; Mathew, R. J.; Ulaganathan, R. K.; Sankar, R.; Kataria, M.; Lin, H. Y.; Chen, Y.; Hofmann, M.; Lee, C.; et al. A Bi-Anti-Ambipolar Field E Ff Ect Transistor. **2021**. https://doi.org/10.1021/acsnano.1c00762.

(71) Wu, P.; Appenzeller, J. Artificial Sub-60 Millivolts/Decade Switching in a Metal-Insulator-Metal-Insulator-Semiconductor Transistor without a Ferroelectric Component. *ACS Nano* **2021**. https://doi.org/10.1021/acsnano.0c10344.

(72) Stanley, L. J.; Chuang, H. J.; Zhou, Z.; Koehler, M. R.; Yan, J.; Mandrus, D. G.; Popović, D. Low-Temperature 2D/2D Ohmic Contacts in WSe2Field-Effect Transistors as a Platform for the 2D Metal-Insulator Transition. *ACS Appl. Mater. Interfaces* **2021**. https://doi.org/10.1021/acsami.0c21440.

(73) Su, Y.; Ouyang, M.; Liu, P.; Luo, Z.; Xie, W.; Xu, J. Insights into the Interfacial

Properties of Low-Voltage CuPc Field-Effect Transistor. *ACS Appl. Mater. Interfaces* **2013**, *5* (11), 4960–4965. https://doi.org/10.1021/am4006447.

(74) Chang, J.; Lin, Z.; Zhang, C.; Hao, Y. Organic Field-Effect Transistor: Device Physics, Materials, and Process. *Intech* **2013**, *32* (July), 137–144. https://doi.org/10.5772/intechopen.68215.

(75) Wang, C.; Dong, H.; Hu, W.; Liu, Y.; Zhu, D. Semiconducting π-Conjugated Systems in Field-Effect Transistors: A Material Odyssey of Organic Electronics. *Chem. Rev.* **2012**, *112* (4), 2208–2267. https://doi.org/10.1021/cr100380z.

(76) Kus, M.; Alic, T. Y.; Kirbiyik, C.; Baslak, C.; Kara, K.; Kara, D. A. Chapter 24 - Synthesis of Nanoparticles. In *Micro and Nano Technologies*; Mustansar Hussain, C. B. T.-H. of N. for I. A., Ed.; Elsevier, 2018; pp 392–429. https://doi.org/10.1016/B978-0-12-813351-4.00025-0.

(77) Zhong, C.; Deng, Y.; Roudsari, A. F.; Kapetanovic, A.; Anantram, M. P.; Rolandi, M. A Polysaccharide Bioprotonic Field-Effect Transistor. *Nat. Commun.* **2011**, *2* (1), 2–6. https://doi.org/10.1038/ncomms1489.

(78) Dodabalapur, A.; Torsi, L.; Katz, H. E. Organic Transistors: Two-Dimensional Transport and Improved Electrical Characteristics. *Science (80-.).* **1995**, *268* (5208), 270–271. https://doi.org/10.1126/science.268.5208.270.

(79) Horowitz, G. Organic Thin Film Transistors: From Theory to Real Devices. *J. Mater. Res.* **2004**, *19* (7), 1946–1962. https://doi.org/DOI: 10.1557/JMR.2004.0266.

(80) Lu, G.; Kong, X.; Ma, P.; Wang, K.; Chen, Y.; Jiang, J. Amphiphilic (Phthalocyaninato) (Porphyrinato) Europium Triple-Decker Nanoribbons with Air-Stable Ambipolar OFET Performance. *ACS Appl. Mater. Interfaces* **2016**, *8* (9), 6174–6182. https://doi.org/10.1021/acsami.5b12368.

(81) Hsieh, C. T.; Chen, C. Y.; Lin, H. Y.; Yang, C. J.; Chen, T. J.; Wu, K. Y.; Wang, C. L. Polymorphic Behavior of Perylene and Its Influences on OFET Performances. *J. Phys. Chem. C* **2018**, *122* (28), 16242–16248.

https://doi.org/10.1021/acs.jpcc.8b02199.

(82) Huang, Y. F.; Wang, C. K.; Lai, B. H.; Chung, C. L.; Chen, C. Y.; Ciou, G. T.; Wong, K. T.; Wang, C. L. Influences of Structural Modification of S, N-Hexacenes on the Morphology and OFET Characteristics. *ACS Appl. Mater. Interfaces* **2019**, *11* (24), 21756–21765. https://doi.org/10.1021/acsami.9b04284.

(83) Yuvaraja, S.; Surya, S. G.; Chernikova, V.; Vijjapu, M. T.; Shekhah, O.; Bhatt, P. M.; Chandra, S.; Eddaoudi, M.; Salama, K. N. Realization of an Ultrasensitive and Highly Selective OFET NO2Sensor: The Synergistic Combination of PDVT-10 Polymer and Porphyrin-MOF. *ACS Appl. Mater. Interfaces* **2020**, *12* (16), 18748–18760. https://doi.org/10.1021/acsami.0c00803.

(84) Hsu, L. C.; Isono, T.; Lin, Y. C.; Kobayashi, S.; Chiang, Y. C.; Jiang, D. H.; Hung, C. C.; Ercan, E.; Yang, W. C.; Hsieh, H. C.; et al. Stretchable OFET Memories: Tuning the Morphology and the Charge-Trapping Ability of Conjugated Block Copolymers through Soft Segment Branching. *ACS Appl. Mater. Interfaces* **2021**, *13* (2), 2932–2943. https://doi.org/10.1021/acsami.0c18820.

(85) Gaubert, P.; Teramoto, A. Carrier Mobility in Field-Effect Transistors. *Intech* **2013**, *32* (July), 137–144. https://doi.org/10.5772/67885.

(86) Roichman, Y.; Tessler, N. Generalized Einstein Relation for Disordered Semiconductors - Implications for Device Performance. *Appl. Phys. Lett.* **2002**, *80* (11), 1948–1950. https://doi.org/10.1063/1.1461419.

(87) Vissenberg, M. C. J. M.; Matters, M. Theory of the Field-Effect Mobility in Amorphous Organic Transistors. *Phys. Rev. B* **1998**, *57* (20), 12964–12967. https://doi.org/10.1103/PhysRevB.57.12964.

(88) Zhong, H.; Wu, G.; Fu, Z.; Lv, H.; Xu, G.; Wang, R. Flexible Porous Organic Polymer Membranes for Protonic Field-Effect Transistors. *Adv. Mater.* **2020**, *32* (21), 1–7. https://doi.org/10.1002/adma.202000730.

(89) Wu, G.-D.; Zhou, H.-L.; Fu, Z.-H.; Li, W.-H.; Xiu, J.-W.; Yao, M.-S.; Li, Q.; Xu, G. MOF

Nanosheet Reconstructed Two-Dimensional Bionic Nanochannel for Protonic Field-Effect Transistors. *Angew. Chemie Int. Ed.* **2021**, *60* (18), 9931–9935. https://doi.org/10.1002/anie.202100356.

(90) Lee, W.-K.; Pietron, J. J.; Kidwell, D. A.; Robinson, J. T.; McGann, C. L.; Sheehan, P. E.; Mulvaney, S. P. Enhanced Protonic Conductivity and IFET Behavior in Individual Proton-Doped Electrospun Chitosan Fibers. *J. Mater. Chem. C* **2019**, *7* (35), 10833–10840. https://doi.org/10.1039/C9TC02452B.

Chapter 2

Proton transport pathways of weak-acid functionalized styrene-based copolymers thin films

Abstract

The study of interfacial proton transport is required to understand biological systems. As commonly found in biomaterials, the carboxylic acid group has been shown to act as a proton-conducting group. This study examined the effect of carboxylic acid concentration on both interfacial and internal proton transport. Several styrene-based polymers containing the carboxylic acid group were synthesized. The amount of carboxylic acid group in the polymer chain was varied to explore the influence of weak acid concentration on polymer thin films' electrical properties. The IR p-polarized multiple-angle incidence resolution spectrometry (pMAIR) spectra show the higher ratio of the free carboxylic acid groups than cyclic dimers in the films with a higher carboxylic acid group concentration, facilitating the more hydrogen bonding networks in films. The water uptake results reveal a similar number of adsorbed water molecules per carboxylic acid group in all thin films. Remarkably, polymer thin films with high carboxylic acid concentrations offer internal proton conduction because of the proportionate increase in the amount of the free carboxylic acid group. In contrast, interfacial proton conduction was found in low carboxylic acid concentration polymers due to the relatively large amount of cyclic dimer carboxylic acid group and little amount of free carboxylic acid group. This research provides insight into interfacial proton transport behavior that differs depending on the weak acid concentration, which could help to explain proton transport in biological systems.

2.1 Introduction

Mostly, acids or proton-donating functional groups in proton conductive polymers give free protons as the charge carrier, allowing proton movement over extended distances. As biopolymers, sugar and protein derivatives have attracted much attention as proton conductive materials because proton-donating functional groups were contained.[1–3] Despite the reported biomaterials' outstanding proton conduction potential, more research into the proton transportation mechanism is required.

Protons may usually move via hydrogen bonding networks. According to reports, the hydrophilic functional groups persuade proton transportation routes from interactions between hydrophilic polymer residues and water molecules, as shown in Figure 2.1.[4–9] Several reports have found that utilizing acid-base combinations of proton conductors improve proton conduction in an anhydrous state.[10–16] The influences of acid and base functional group density on the proton conductivity through proteins-based materials have been described. Enhancement of proton conductivity was discovered in bovine serum albumin(BSA)-mat with the addition of hydroxyl, amine, and carboxylic acid functionalized carbon dots.[4] Hydrophobic substitution on carboxylic acid or amine functional groups of BSA-mat, on the other hand, prevents proton conduction.[5] This study supports the hypothesis that the acid-base functional groups' concentration has a major impact on the charge carrier density and proton conduction. It has been established that polar functional group variations influence proton conductivity in materials.[17] Functional groups with a high polarity or hydrophilicity have higher proton conductivity than functional groups with low hydrophilicity. It has also been claimed that materials having a carboxylic acid functional group have better proton conductivity than those with amine or other hydrophobic groups.[5] Overall, these data support the carboxylic acid's ability and importance as a proton-conducting group.

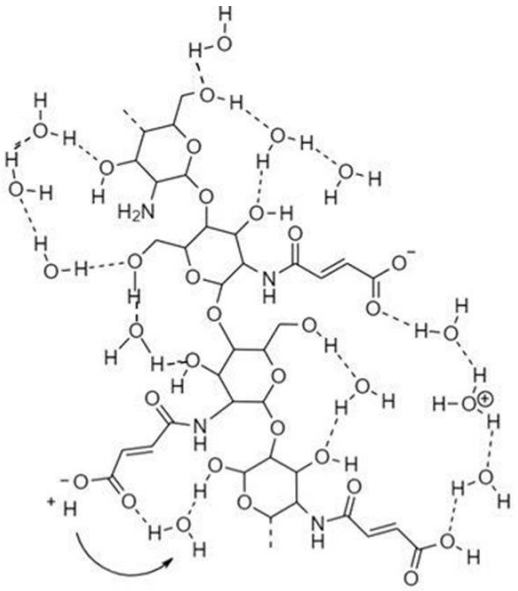

Figure 2.1. The schematic presents the hydrogen-bonding network between water molecules and polar groups of maleic chitosan.[18]

Because protons can move via both the internal and the surface materials, understanding how they work in many biological systems necessitates research into proton transport. The biomaterial surface must be taken into account because it has an impact on a variety of properties, for example, the polarity and electrical properties.[19,20] Numerous studies of proton transport at the lipid monolayer surface have been published.[21–25] Several research have looked into proton translocation over the biomembrane surface.[26–29] Nagao and Kubo discovered the surface proton transport on a fully protonated poly(aspartic acid) thin film containing the carboxylic acid group, as shown in Figure 2.2.[30] Despite the fact that carboxylic acid is abundant on biomaterial surfaces, the influences of carboxylic acid concentrations on interfacial proton transport are unknown.

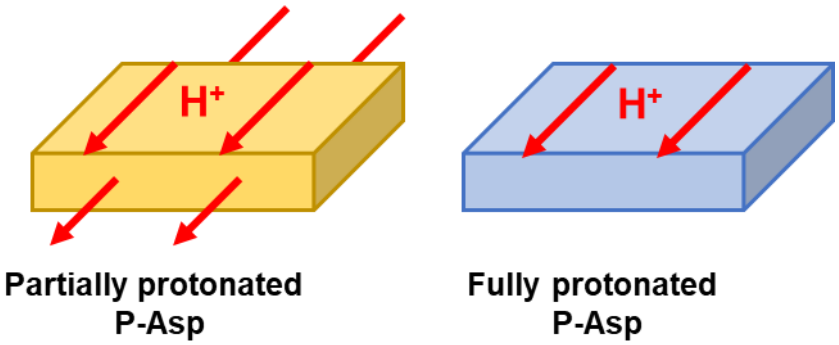

Figure 2.2. Proton transport pathway of poly(aspartic acid) (P-Asp): a) the surface and internal proton conduction in the partially protonated P-Asp thin film and b) the surface conduction in the fully protonated P-Asp thin film.[30]

The effect of carboxylic acid concentrations in styrene (St)-based copolymers on proton conductivity, including both internal and interfacial proton conduction and water uptake, was examined in this work. The St-based polymer was synthesized with well-defined carboxylic acid concentrations. Because of the reactivity difference between St and St containing carboxylic acid monomers, the ester derivative monomer was selected for the polymerization reaction. To investigate the impact of carboxylic acid concentration on proton transport behavior, the polymers were functionalized with various amounts of carboxylic acid group. And to study the interfacial proton conduction capabilities, the polymers were made as thin films to improve the ratio of film surface area to bulk.

2.2 Materials and methods

2.2.1 Materials

Styrene with TBC stabilizer (St, >99.0%) and 2,2'-azobis(isobutyronitrile) (AIBN, >98.0%) were purchased from Tokyo Chemical Industry Co. Ltd., Japan. 4-Vinylbenzoic acid (4VBA, >97.0%) was purchased from Fujifilm Wako Pure Chemical Corp., Japan. Toluene, super dehydrated, was purchased from Wako Pure Chemical Industries Ltd., Japan, and used without further purification. Methanol, ethanol, ethyl acetate, tetrahydrofuran (THF), N,N-dimethylformamide (DMF), sodium hydroxide, sulfuric acid, hydrochloric acid, sodium sulfate, and sodium chloride were used as received from Wako Pure Chemical Industries Ltd., Japan. DI water was used in the hydrolysis reaction. The chemical structure of AIBN initiator, St, and 4VBA monomers were shown in Figure 2.3.

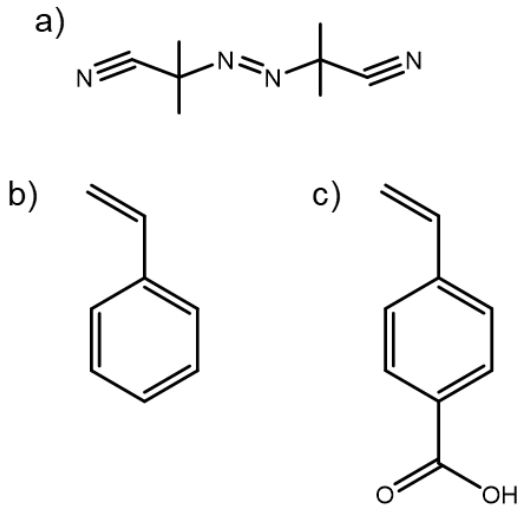

Figure 2.3. Chemical structure of a) AIBN, b) St, and c) 4VBA.

2.2.2 Purification of AIBN

AIBN was recrystallized before use. AIBN was slowly dissolved in a small amount of hot methanol (55 °C) and filtered through a filter paper. The filtered solution was then cooled down and kept in the fridge overnight for crystallization. The crystal AIBN was collected via vacuum filtration, washed with cold methanol, and dried under vacuum before being stored in the fridge.

2.2.3 Purification of St

The stabilizer was eliminated from the St solution by the vacuum distillation. Pure St solution was immediately used for the reaction after the purification.

2.2.4 Purification of 4VBA

4VBA was recrystallized from a mixture of water and ethanol with a ratio of 3:2 to remove the stabilizer. The crystallized 4VBA was immediately used for the reaction after being filtered and dried under vacuum overnight.

2.2.5 Synthesis of 4VBZA

4VBA was dissolved in methanol and mixed with sulfuric acid, then refluxed for 3 h. The 4-vinylbenzoate (4VBZA) product was extracted with ethyl acetate and washed with brine. Then finally dried under vacuum to eliminate the high boiling point solvent.

2.2.6 Polymerization

Free-radical polymerization was used to synthesize many styrene-based polymers with ester groups. The polymer product consists of two different monomer units, St monomer and St monomer with an ester group located at the benzene ring, 4VBZA monomer. AIBN was used as the initiator. Scheme 2.1 displays the reaction scheme mechanisms of the radical initiator formation and polymerization. Table 2.1 shows that the ratio of 4VBZA and St monomers amount added for the reaction varied from 1:4 to 1:0. However, the monomer ratio inputted is differed from the monomer ratio achieved. The polymerization products were defined as P4VBZA100 (poly-4-vinylbenzoate100) and PS4VBZA75, 50, and 33 (polystyrene-*co*-4-vinylbenzoate75, 50, and 33) according to the monomer input ratios.

Scheme 2.1. The reaction scheme mechanisms of the radical initiator formation and polymerization.

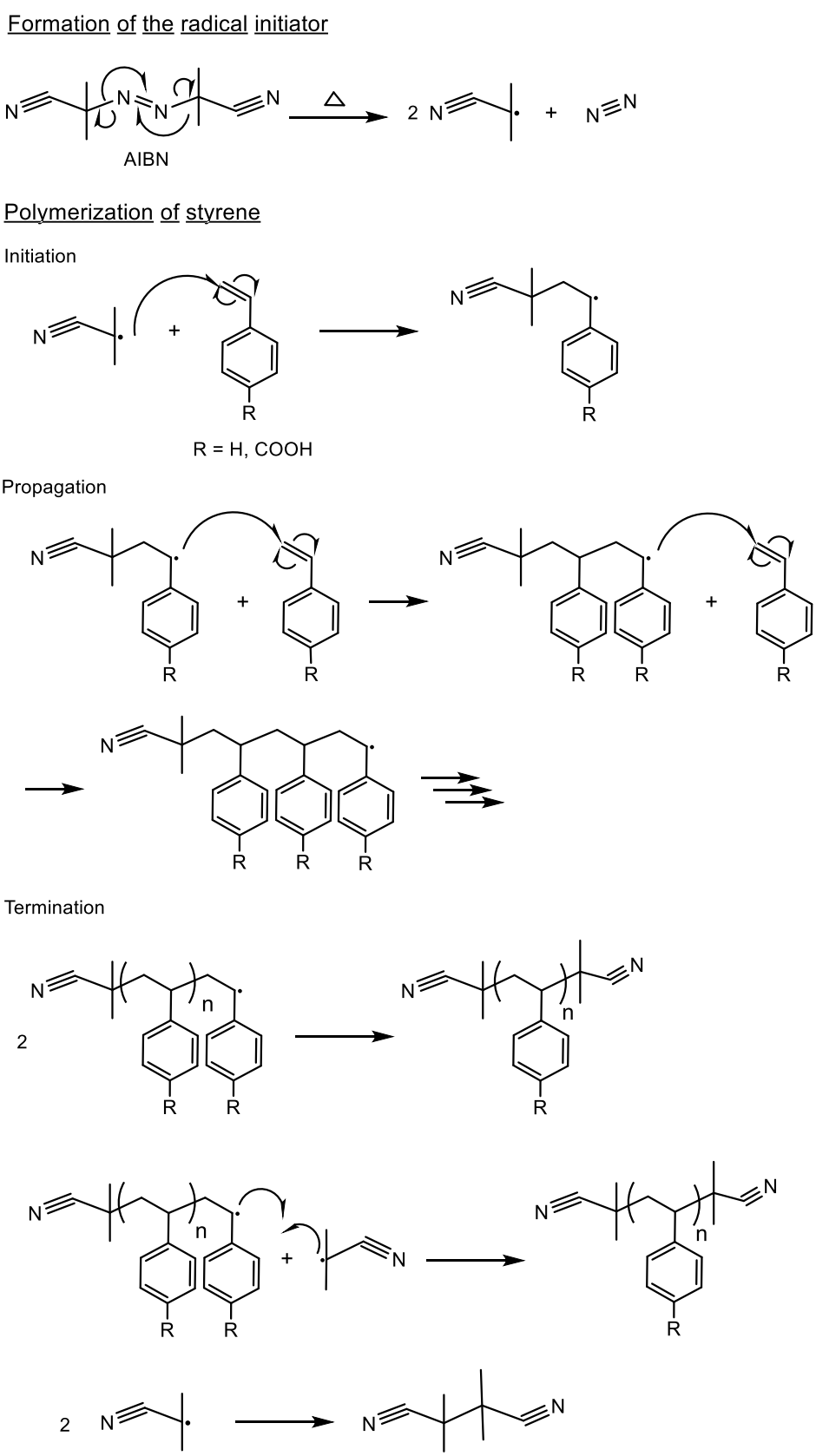

Table 2.1. The ratio of monomers added for the polymerization and the final ratio of obtained polymers.

Polymers	Molar ratio (4VBZA:St)	
	Added	Obtained
P4VBZA100	4:0	4:0
PS4VBZA75	3:1	3:1
PS4VBZA50	2:2	2:2
PS4VBZA33	1:3	1:2

2.2.6.1 P4VBZA100

0.2 mmol of AIBN was added after dissolved 18 mmol of 4VBZA in 3 mL ethyl acetate and 4 mL toluene. Then degassed the mixture solution by three freeze–evacuate–thaw cycles. Polymerization was reacted at 80 °C for 24 h under an inert atmosphere, and then the reaction was stopped by put the reaction flask in the ice bath. The P4VBZA100 polymer was precipitated from warm methanol and dried under a vacuum with an 82% yield.

2.2.6.2 PS4VBZA75

This polymer used 13.5 mmol of 4VBZA and 4.5 mmol of St. The reaction was done using the same polymerization procedure as that used for P4VBZA100 polymerization, as shown in Scheme 2.2. As a result, PS4VBZA75 polymer was collected with a yield of 62%.

Scheme 2.2. Polymerization of PS4VBA.

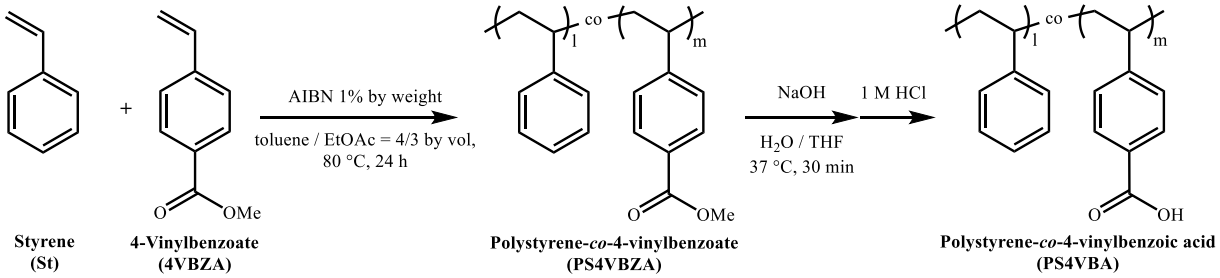

2.2.6.3 PS4VBZA50

For PS4VBZA50, 9 mmol of 4VBZA and 9 mmol of St were used. The same procedure as that used for the preparation of P4VBZA100 was performed. As a result, PS4VBZA50 polymer was achieved with a 40% yield.

2.2.6.4 PS4VBZA33

4.5 mmol of 4VBZA and 13.5 mmol of St were mixed in the toluene and ethyl acetate solvent. The reaction was proceeded using the same method as the P4VBZA100 preparation. Then PS4VBZA33 polymer was collected with a yield of 67%.

2.2.7 Hydrolysis

The solution of polymer, sodium hydroxide in methanol, water, and THF was mixed together. The reaction was done at 37 °C for 30 min. The polymer product in sodium salt form was precipitated in tetrahydrofuran (THF) solvent and then dried under vacuum without heating.

2.2.8 Ion exchange

To do the ion exchange, the polymer in sodium salt form was immersed in 1 M HCl solution, shaken until the pale-yellow color of a polymer change to white and become water-insoluble (around 1 min). Then polymer was separated from the solution using a centrifuge. And the new acid solution was replaced, repeated this step for three times. The final polymer product, polystyrene-*co*-4-vinylbenzoic acid (PS4VBA) or poly-4-vinylbenzoic acid 100 (P4VBA100) were washed with water until the water became neutral. Then it was respectively dried under vacuum at room temperature and 35 °C.

2.2.9 Characterization

2.2.9.1 Nuclear magnetic resonance (NMR)

The ^{1}H and ^{13}C nuclear magnetic resonance (NMR, Bruker Avance III (400 MHz) spectrometer; Bruker Analytik GmbH) spectra were recorded using dimethyl sulfoxide-d_6 (DMSO-d_6), chloroform-*d* ($CDCl_3$), or deuterium oxide (D_2O) as a solvent. The ^{13}C was done at a high temperature of 50 °C.

2.2.9.2 Infrared (IR) spectroscopy

The IR spectra of polymers powder were collected by Attenuated total reflection Fourier-transform infrared (ATR-FTIR, Nicolet 6700; Thermo Fisher Scientific Inc.) spectroscopy in the range of 400-4000 cm^{-1}.

2.2.9.3 Gel permeation chromatography (GPC)

The weight average molecular weights (M_w) and the polydispersity indexes (PDI) of the polymer were estimated by gel permeation chromatography (GPC, LC-2000plus; JASCO). DMF with 0.01 M lithium bromide was used as a mobile phase, and polystyrene standards (M_w = 786-23.6×10^3) were applied for the calibration.

2.2.9.4 Thermogravimetric analyzer (TGA)

Thermal analyses were performed using the thermogravimetric analyzer (TGA, TG-DTA2010 SA; NETZSCH) under nitrogen atmosphere. The temperature was increased from room temperature to 800 °C with a heating rate of 10 °C/ min.

2.2.9.5 X-ray photoelectron spectroscopy (XPS)

The difference in carboxylic acid concentration at the thin film surface between the fabricated polymers was confirmed using X-ray photoelectron spectroscopy (XPS). The XPS was performed using a delay-line detector (DLD) spectrometer (Kratos Axis-Ultra; Kratos Analytical Ltd.) with an Al Kα radiation source (1486.6 eV).

2.2.9.6 Infrared (IR) p-polarized multiple-angle incidence resolution spectrometry (p-MAIRS)

The p-MAIR spectra were collected by Fourier-transform infrared (FTIR, Nicolet 6700; Thermo Fisher Scientific Inc.) spectroscopy installed with a mercury-cadmium-telluride (MCT) detector. Figure 2.4 shows the optical configuration. Single-beam spectra were recorded by 6° steps between the angle of incidence in a range of 38° – 8°. The aperture was fully opened in a size of 150. A metal plate with small pores was put in the light path of the incidental beam to prevent saturation. Nitrogen gas was flow through the sample chamber to reduce the effect of water vapor absorption. For each angle of incidence, 64 scans were performed with a

wavenumber resolution of 4 cm^{-1}. The p-MAIRS analysis was proceeded using p-MAIRS analyzer software (Thermo Fisher Scientific Inc.).

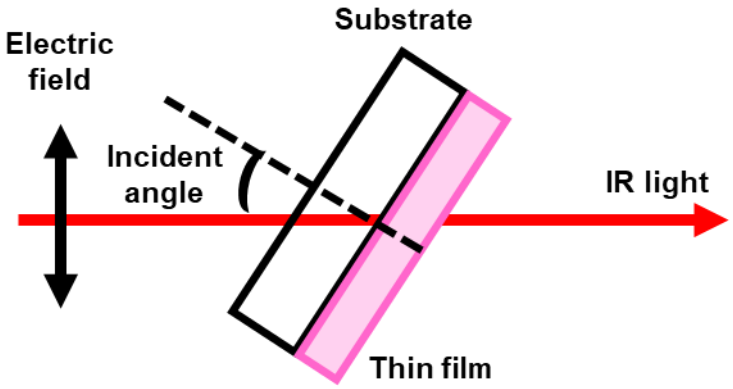

Figure 2.4. Configuration of the polarized incident beam path and incident angle.[31]

2.2.10 Preparation of polymer thin films

The polymer with 2-4 wt% was dissolved in the dimethylformamide (DMF) and THF (2:3) mixed solvent, then spin-coating (ACT-200 spin-coater; Active) on the substrate. Next, the quartz substrates were washed with toluene, acetone, and 2-propanol, respectively, followed by plasma treatment (Cute-MP; Femto Science Inc., Korea). Then, to eliminate the high boiling point solvent, the film was dried overnight under vacuum at 60 °C. Finally, the film thickness was determined using a white light interferometric microscope (BW-S506; Nikon Corp.).

2.2.11 Water uptake measurement

The polymer thin film's water uptake ability was estimated by relative humidity (RH)-controlled in-situ quartz crystal microbalance (QCM) system. A QCM substrate (QA-A9M-SIO2-S(M)(SEP); Seiko EG&G Co. Ltd.) was connected to a frequency counter (53131 A; Agilent Technologies, Inc.). The frequency difference between the bare and film-coated substrates was measured. The Sauerbrey equation was used to estimate dry film's mass under a nitrogen atmosphere.

$$\Delta m = {S \times \sqrt{\rho\mu}}\Big/{2 \times F^2} \times (-\Delta F), \quad (1)$$

where S, ρ, and μ, respectively, denote the electrode's surface area, density of quartz, and quartz shear modulus. F indicates the substrate fundamental frequency.

The humidity environments were controlled by mixing humidified and dry N_2 using a relative humidity (RH) controller (BEL Flow; MicrotracBEL Corp.). The hydration number (λ) as the moles of water per carboxylate group, was calculated as

$$\lambda = \left({}^{m}/_{m_0} - 1\right) \times {}^{EW}/_{M_{H_2O}}, \quad (2)$$

where m is the mass of film at each relative humidity (RH) and m_0 denotes the mass of dry film. Also, *EW* and M_{H2O} respectively stand for the equivalent weight of the polymer and the molecular mass of water. The illustration that represents the QCM measurement was shown in Figure 2.5.

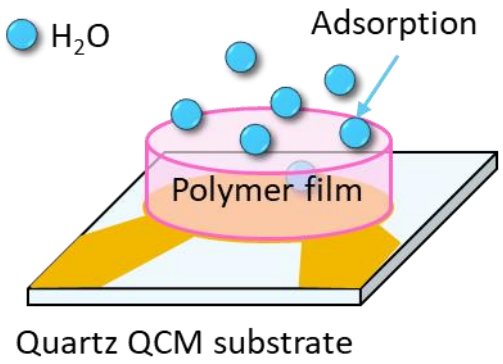

Figure 2.5. Schematic represents the structure of polymer thin film on quartz QCM substrate.

2.2.12 Proton conductivity measurements

The proton conductivity of polymer thin film was examined inside the RH-controlled and temperature-controlled chamber (SH-221; Espec Corp.) using impedance spectroscopy measurements obtained with a frequency response analyzer equipped with a high-frequency dielectric interface (SI1260 and SI1293; Solartron Analytical). The in-plane conductivity was investigated using the two-probe method (Figure 2.6). The electrodes were made with porous gold paste (SILBEST No. 8560; Tokuriki Chemical Research Co. Ltd.). The conductivity (σ) of the polymer thin film was calculated using the following equation.

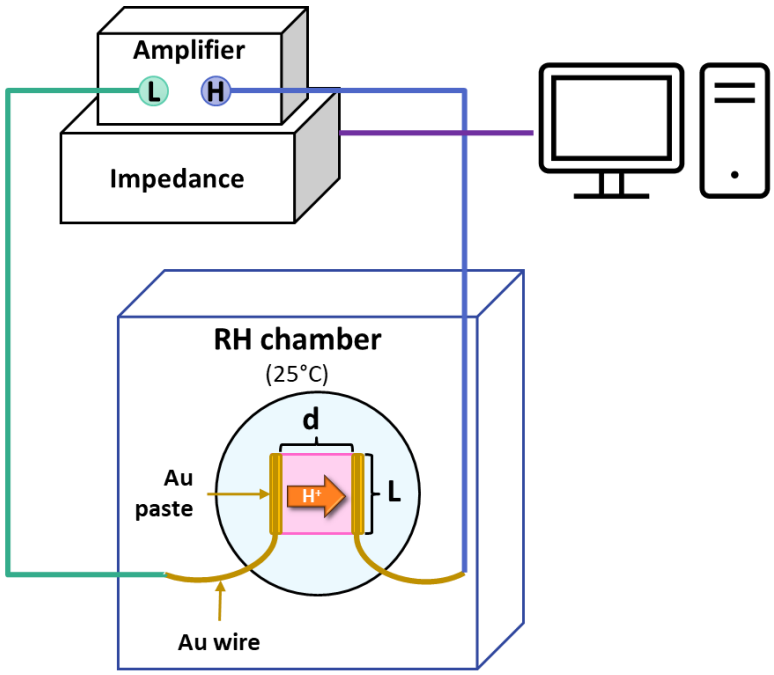

Figure 2.6. Schematic represents the proton conductivity measurement.

$$\sigma = {}^{d}/_{RLt} \quad (3)$$

In the equation above, d stands for the distance between two electrodes. R, L, and t denote the resistance value recorded from the impedance, the electrode length contacted with a polymer film, and the thickness of polymer film.

To observe the interfacial proton conduction, the normalized resistance (*R*') was calculated using the following equation.[30]

$$R' = {}^{RL}/_{d} \quad (4)$$

Since water can be adsorbed on both air/ film and film/ substrate surface interfaces, interfacial proton conduction can occur at both interfaces. Therefore, the normalized resistance is independent of the film thickness if the interfacial proton conduction dominantly happens. In contrast, the normalized resistance depends on the film thickness if the internal proton conduction occurs at the thin film interfaces region.

The temperature-dependent proton conductivity was observed by measuring the conductivity under various temperatures and constant RH of 90%. The activation energy of polymer thin film was estimated using the following equation.[32]

$$\sigma T = \sigma_0 \exp\left(^{-E_a}/_{RT}\right), \quad (5)$$

where T, σ_0, E_a, and *R* represent the temperature, pre-exponential factor, activation energy, and gas constant.

2.3 Results and Discussion

2.3.1 The preparation of monomers

Styrene monomer was purified through the vacuum distillation technique. The stabilizer, 4-tert-butylcatechol (TBC), which has a higher boiling point, can be eliminated from St monomer in this step. The chemical structure of the purified St monomer was confirmed by the ^{1}H-NMR spectrum. The peaks at the region of 5-8 ppm were assigned as protons from the St monomer, as shown in Figure 2.7. All peak intensity ratios were conformable with the number of protons in each position, approved the success of purification by vacuum distillation.

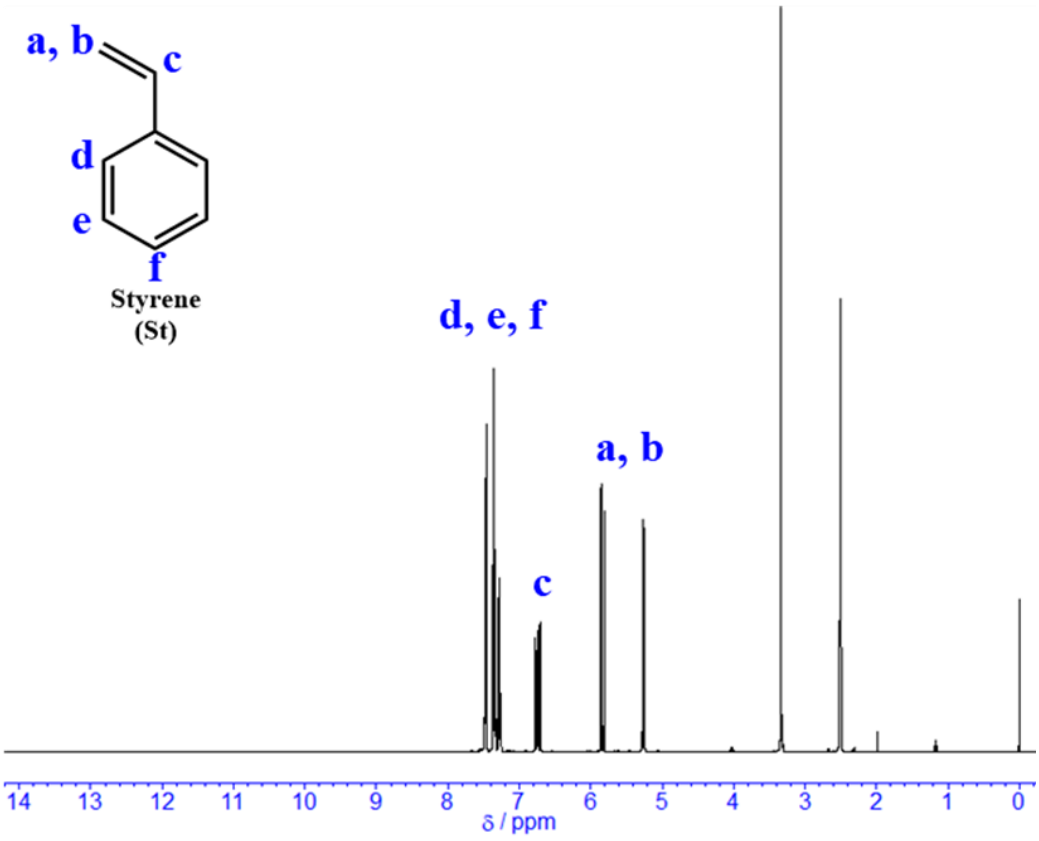

Figure 2.7. ^{1}H-NMR spectrum and chemical structure of recrystallized St in DMSO-d_6 solvent.

4VBA monomer was also purified but through the recrystallization technique. The chemical structure of 4VBA was identified through the ^{1}H-NMR spectrum, as shown in Figure 2.8. A singlet peak of the carboxylic acid group was clearly shown at 12.9 ppm. All peak intensity

ratios were consistent with the number of protons in the 4VBA structure, confirm the purified product of the 4VBA monomer.

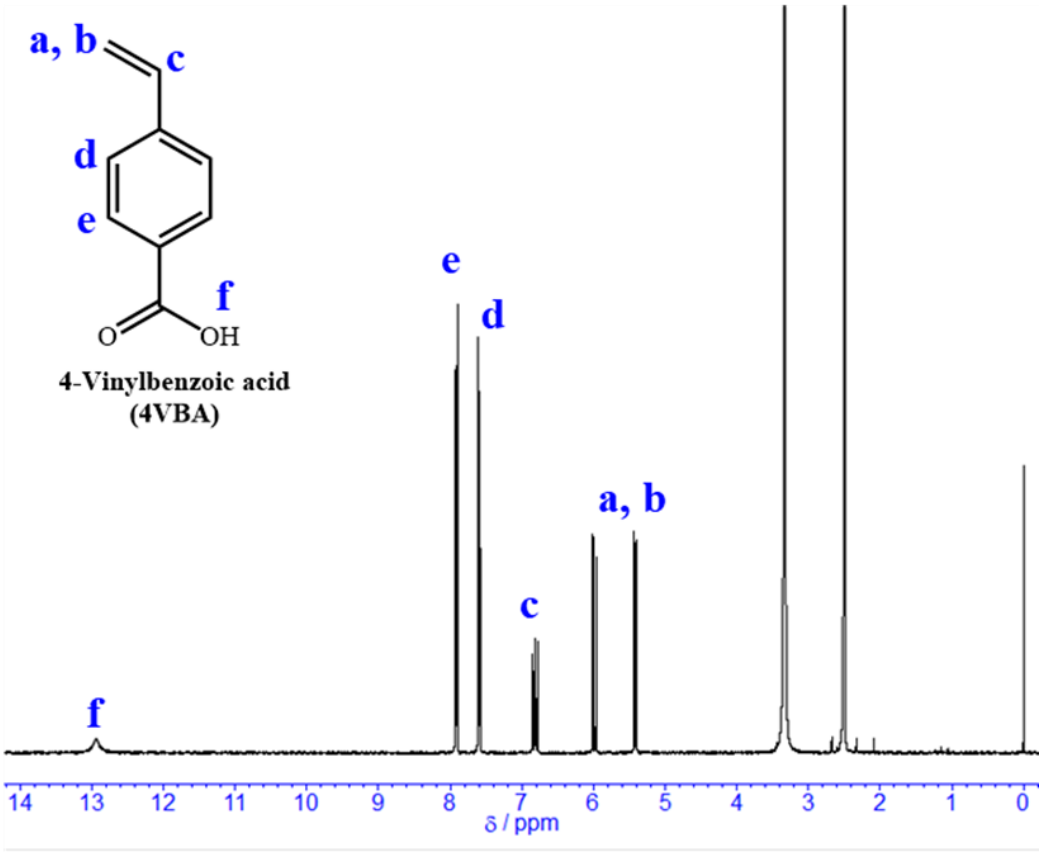

Figure 2.8. ^{1}H-NMR spectrum and chemical structure of recrystallized 4VBA in DMSO-d_6 solvent.

The conversion of a carboxylic acid group in the 4VBA monomer was performed through the esterification reaction. The ester product, 4VBZA monomer, was ensured by the ^{1}H-NMR spectrum, as shown in Figure 2.9. A peak at 12.9 ppm was completely disappeared from the spectrum. On the other hand, a sharp peak of the ester group was shown at 3.8 ppm. This information confirms the success of the esterification reaction and chemical structure of the 4VBZA monomer product.

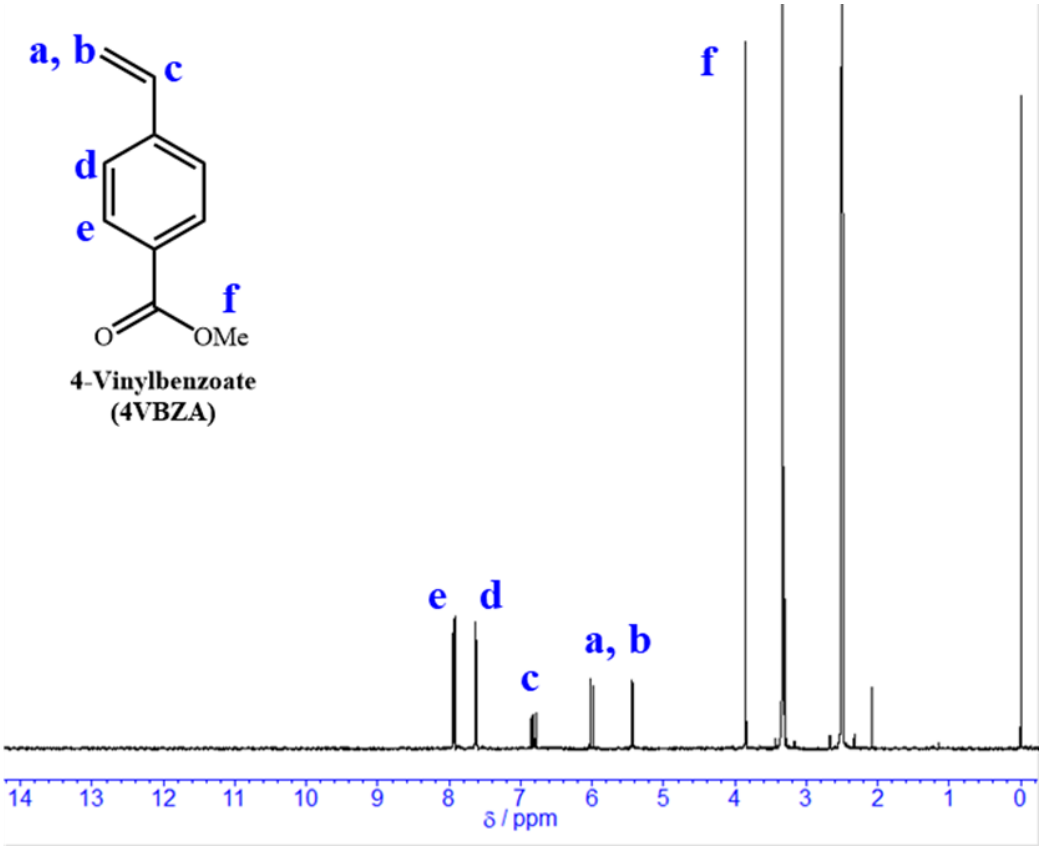

Figure 2.9. ^{1}H-NMR spectrum and chemical structure of recrystallized 4VBZA in DMSO-d_6 solvent.

2.3.2 Establishment of polymerization route and characterization

Their significant polymerization reactivity differences made it difficult to obtain a copolymer by mixing St and 4VBA monomers directly into the reaction solution. 4VBA monomer is able to interact with other 4VBA monomers through the hydrogen bonding interaction of the carboxylic acid group.[33–35] This intermolecular interaction might cause the higher reactivity of the 4BVA monomer than the St monomer during the polymerization due to the aggregation of 4VBA monomers.

To prevent this situation, the hydrogen bonding interaction between 4VBA monomers should be relieved. Because of the weaker interaction among the ester groups, converting a carboxylic acid group to an ester group is one technique to lessen the effect of hydrogen bonding interactions.[36,37] Therefore, several styrene polymers with varying quantities of the carboxylic group were produced through free-radical polymerization of St monomer and St-based monomer substituted with ester groups. First, the 4VBA monomer's acid group was converted to the methyl ester, 4VBZA, through an esterification reaction. Then, this lowered reactivity monomer was directly polymerized with a St monomer, as shown in Scheme 1.

The ^{1}H-NMR spectra were used to confirm the chemical structure of polymer products and the ester group's amount ratio, as shown in Figure 2.10. The signal of an ester group was appeared at around 3.8 ppm in all polymers' spectra. According to the ratio of the 4VBZA monomer unit, the different ester signal intensity ratio reveals the varied ester group concentration in each produced polymer. A polymer in which all monomer units contain an ester group (P4VBZA100) shows the highest peak integral ratio followed by PS4VBZA75, 50, and 33, respectively. They were compatible with the integral ratio of peak 'b', which reduced with enhancing an ester group and then vanished entirely in the spectrum of P4VBZA100. However, the polymer with a 33% ester group ratio (PS4VBZA33) was obtained from the 1:3 (25%) 4VBZA monomer initial ratio. The GPC was performed to investigate the M_w of the polymer in an ester form, as shown in Table 2.2.

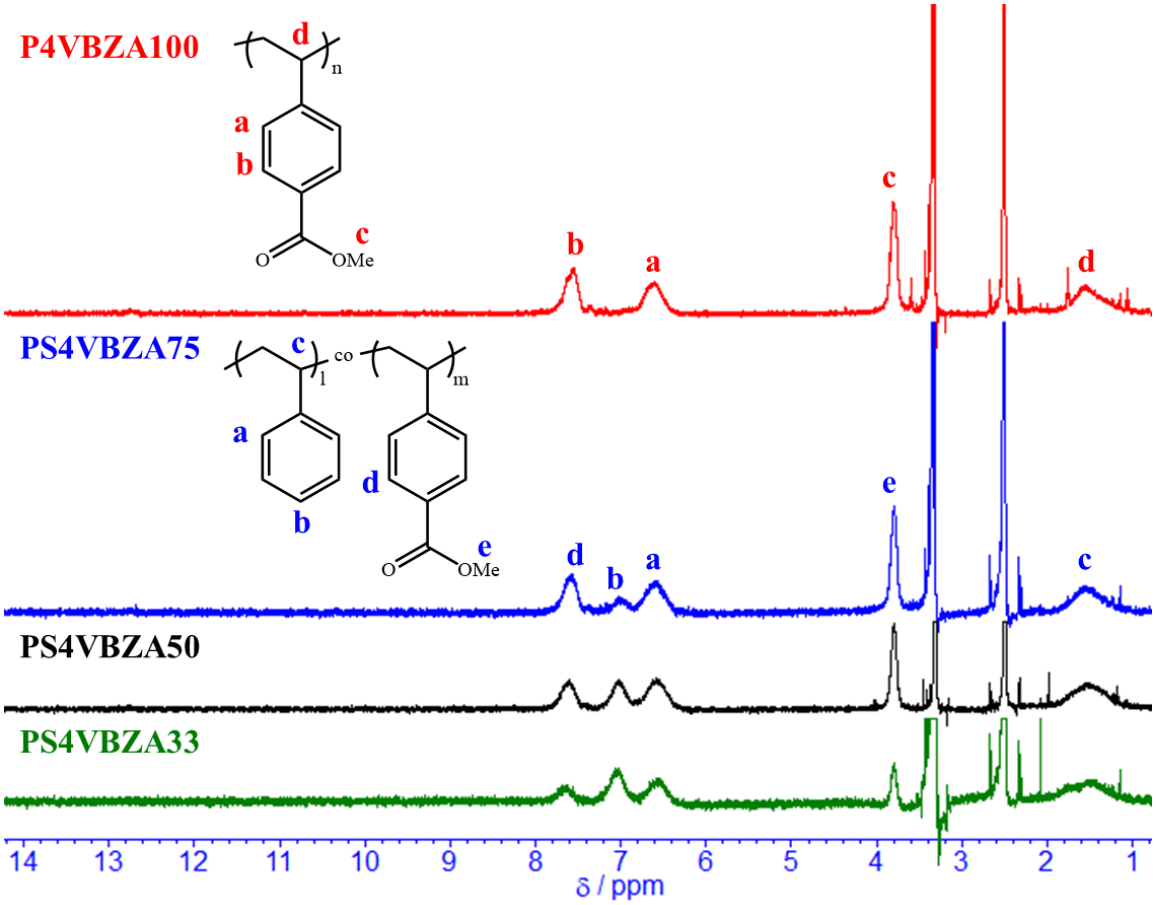

Figure 2.10. ^{1}H-NMR spectra and chemical structure of synthesized polymers in DMSO-d_6 solvent: P4VBZA100 (red), PS4VBZA75 (blue), PS4VBZA50 (black), and PS4VBZA33 (green).

Table 2.2. The summarized molecular weight and polydispersity index of the synthesized copolymers with various ratios of monomer.

Polymers	Molar ratio of monomers in polymer chain (4VBZA:St)	M_w	PDI
P4VBZA100	4:0	99000	1.7
PS4VBZA75	3:1	80000	1.9
PS4VBZA50	2:2	54000	1.8
PS4VBZA33	1:2	42000	1.4

The ^{13}C-NMR spectra (Figure 2.11) show a signal of the carbonyl group around 167 ppm, attesting to the existence of an ester group. To identify the block and random copolymer, the change of ^{13}C-NMR signals between the block and random copolymers was investigated.[38–40] The random copolymers tend to show split and slightly broad signals due to different environments in the polymer chain. In comparison, the block copolymers provide sharp signals with less peak splitting.[39] The examination of quaternary carbon connected with polymer backbone ('c' and 'h' positions) signals were reported.[40] Figure 2.11b displays the slightly broader 'c' and 'h' signals of PS4VBZA75, 50, and 33 copolymers than the P4VBZA100 homopolymer, leading to the assumption that the synthesized copolymers might be not the block copolymers. Moreover, the carbon signals were slightly shifted with the varying ester group concentration of copolymers, summarized in Table 2.3. However, the block copolymer should not show the chemical shift of the signals due to the almost unchanged environment in the polymer chain. Therefore, this trend of chemical shift might be indicated that the fabricated copolymers are not block copolymers.

To confirm the structure of copolymers, the reactivity ratio of two monomers was estimated through Fineman-Ross and inverted Fineman-Ross equations, as respectively shown below.[41–43]

$$\mathrm{G} = r_1\mathrm{H} - r_2\,, \tag{6}$$

$$G/_H = -r_2\,1/_H + r_1\,, \tag{7}$$

where

$$G = \left(f_1/_{f_2}\right)\left[\left(F_1/_{F_2}\right) - 1\right] \Big/ \left(F_1/_{F_2}\right), \tag{8}$$

$$H = \left(f_1/_{f_2}\right)^2 \Big/ \left(F_1/_{F_2}\right), \tag{9}$$

therein, r indicates the reactive of monomer. F and f respectively denote the mole fraction of monomers and mole fraction of each monomer in the copolymer.

Figure 2.12 represents the Fineman-Ross and inverted plots, including the linear fitting line. The reactivity of St (r_{St}) and 4VBZA (r_{4VBZA}) were estimated as 0.50 and 0.87, respectively. Both monomers' reactivity and the product of $r_{St} \times r_{4VBZA}$ are less than 1, indicating the tendency towards an alternating copolymer of the synthesized copolymers.[44–46]

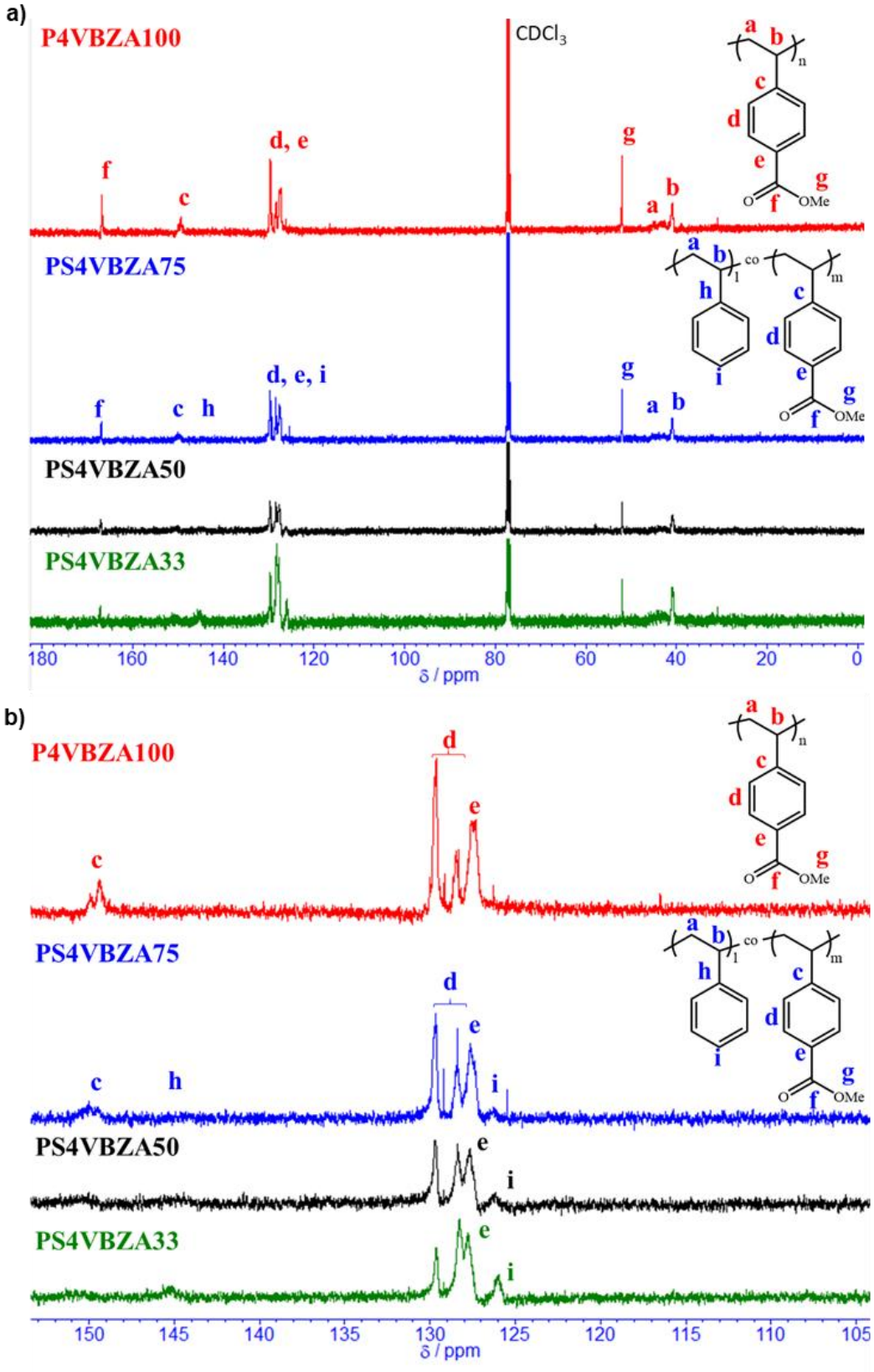

Figure 2.11. a) ^{13}C-NMR spectra and chemical structure of final polymer products in $CDCl_3$ solvent: P4VBZA100 (red), PS4VBZA75 (blue), PS4VBZA50 (black), and PS4VBZA33 (green). b) Enlargement of ^{13}C-NMR spectra a) from 105-153 ppm.

Table 2.3. The summarized ^{13}C-NMR signal positions of the synthesized copolymers with various ester concentrations.

Polymers	Signal position (ppm)				
	Carbonyl of ester	*Para*- of 4VBZA	*Para*- of St	Methyl of ester	Polymer backbone
P4VBZA100	166.8	127.4	-	52.1	41.0
PS4VBZA75	166.9	127.6	126.4	52.0	41.0
PS4VBZA50	167.1	127.7	126.2	52.0	40.9
PS4VBZA33	167.2	127.8	126.0	52.0	40.9

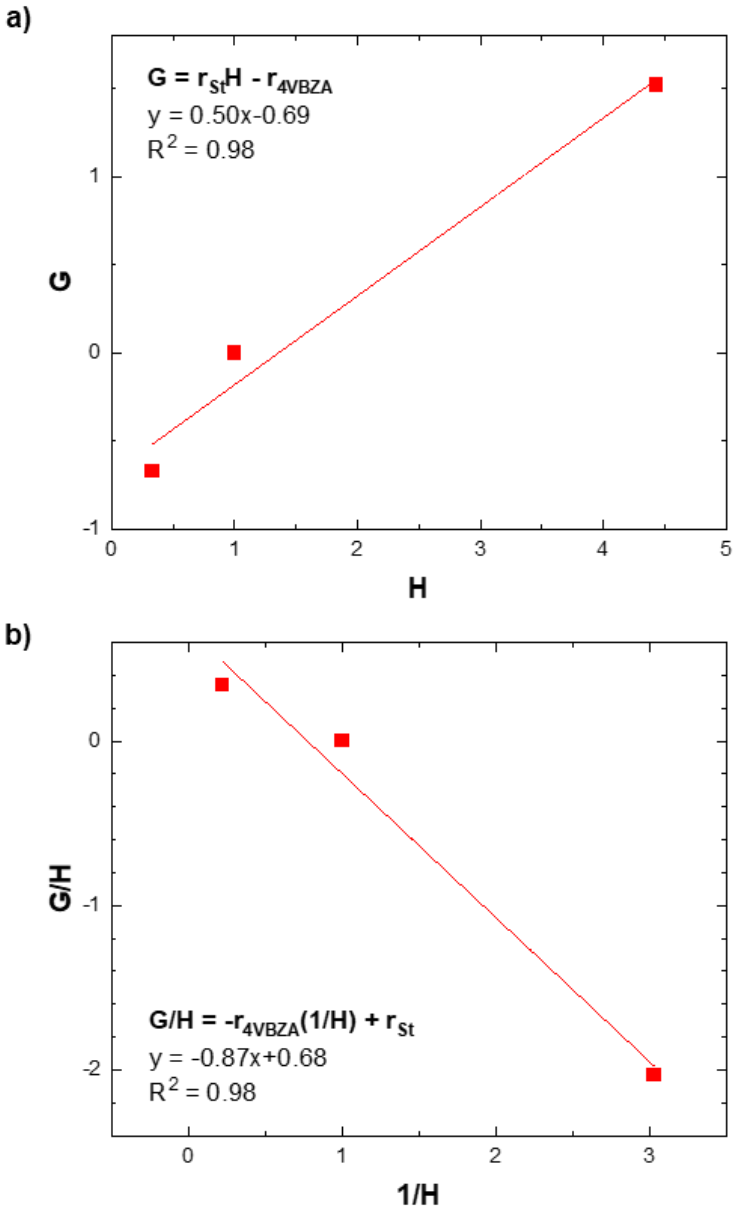

Figure 2.12. a) Fineman-Ross and b) inverted Fineman-Ross plots for PS4VBZA copolymers.

The ester group polymer was then hydrolyzed using a strong base, followed by an ion-exchange reaction in an acidic solution to restore the carboxylic acid functional group (Scheme 2.2). The peak of the ester group (3.8 ppm) was vanished after the hydrolysis reaction, as shown in Figure 2.13. In addition, the signal of the carboxylic acid group of all polymers was clearly visible in the spectra at around 12.7 ppm, as shown in Figure 2.14. The carboxylic acid peak intensity ratio is consistent with the amount of an ester group present before the hydrolysis reaction for all polymers spectra, indicating the 100% success of hydrolysis and ion exchange procedures. Moreover, these ^{1}H-NMR spectra also ensure the various carboxylic acid concentrations for each prepared polymer.

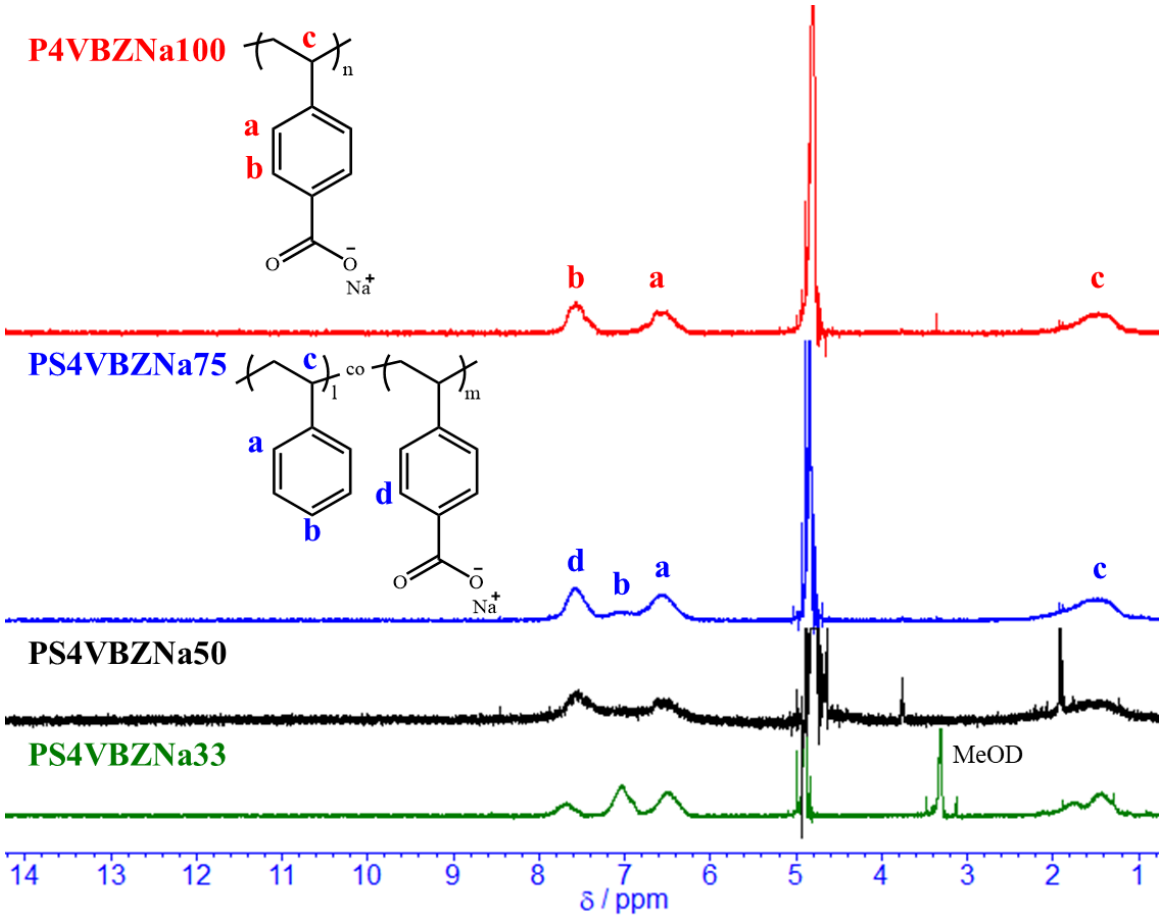

Figure 2.13. ^{1}H-NMR spectra and chemical structure of synthesized polymer in sodium salt-form after hydrolysis reaction in D_2O solvent: P4VBZNa100 (red), PS4VBZNa75 (blue), and PS4VBZNa50 (black), and in MeOD-d_4 solvent for PS4VBZNa33 (green).

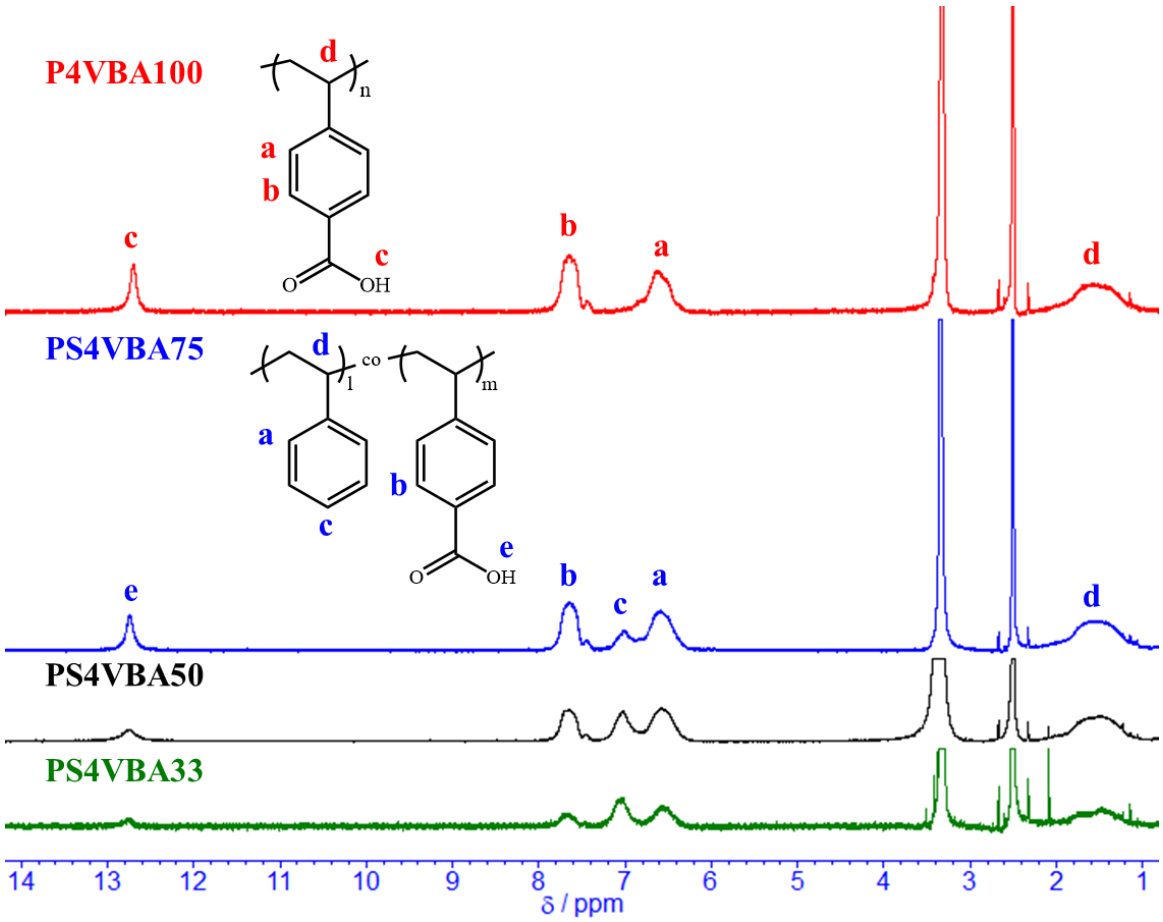

Figure 2.14. ^{1}H-NMR spectra and chemical structure of synthesized polymers in DMSO-d_6 solvent: P4VBA100 (red), PS4VBA75 (blue), PS4VBA50 (black), and PS4VBA33 (green).

Then ATR-FTIR spectroscopy was performed to examine the produced polymer products. The bands of C=O (1690 cm^{-1}) and C-O (1250 cm^{-1}) were examined, confirming the existence of the carboxylic acid group in the polymer chain (Figure 2.15).[47,48] The thermal stability of the produced polymer was investigated using TGA (Figure 2.16). Two steps weight loss was observed in all polymers. The first weight loss attribute to the evaporation of water in the polymer, starting from 50 °C. The second weight loss is attributable to polymer backbone degradation, which started at 350 °C. After 500 °C, the polymers were degraded entirely, and the amount of char[47] leftover from chemical interactions with organic substances was similarly agreed with the amount of carboxylic acid group in the polymer chain. The carboxylic acid group might cause dehydration, carbonization, and oxidation, resulting in a higher amount of char left in the higher carboxylic acid concentration polymer.

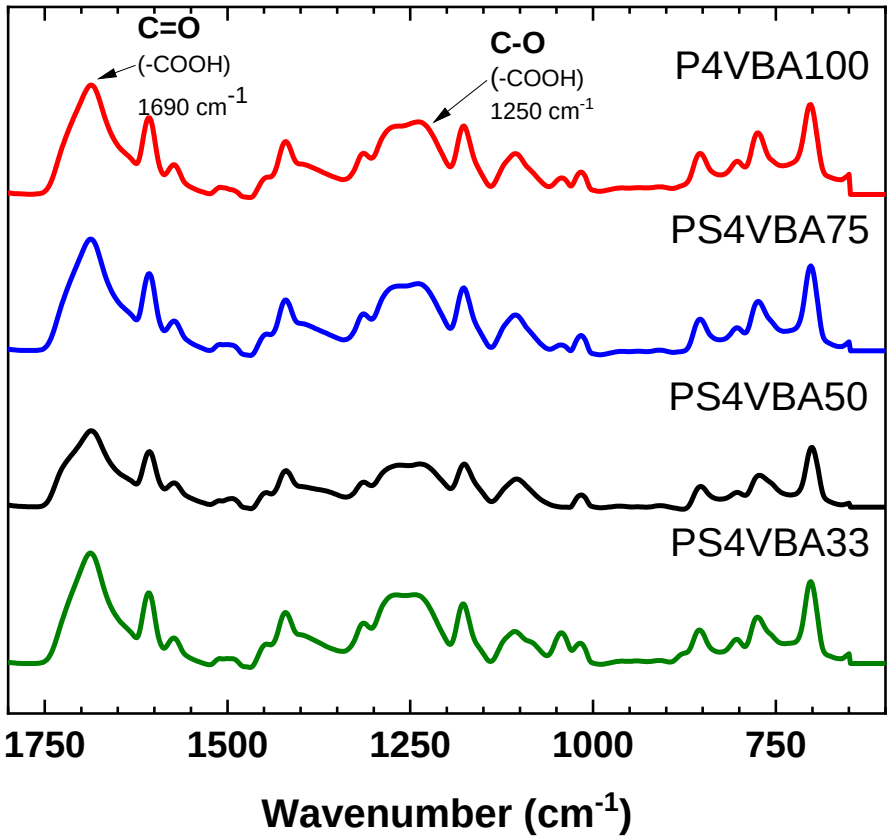

Figure 2.15. ATR-FTIR spectra of final polymer products: P4VBA100 (red), PS4VBA75 (blue), PS4VBA50 (black), and PS4VBA33 (green). All polymers show the band of C=O (1685 cm^{-1}), C-O (1250 cm^{-1}), and the hydrogen-bonding interaction (1420 cm^{-1}).

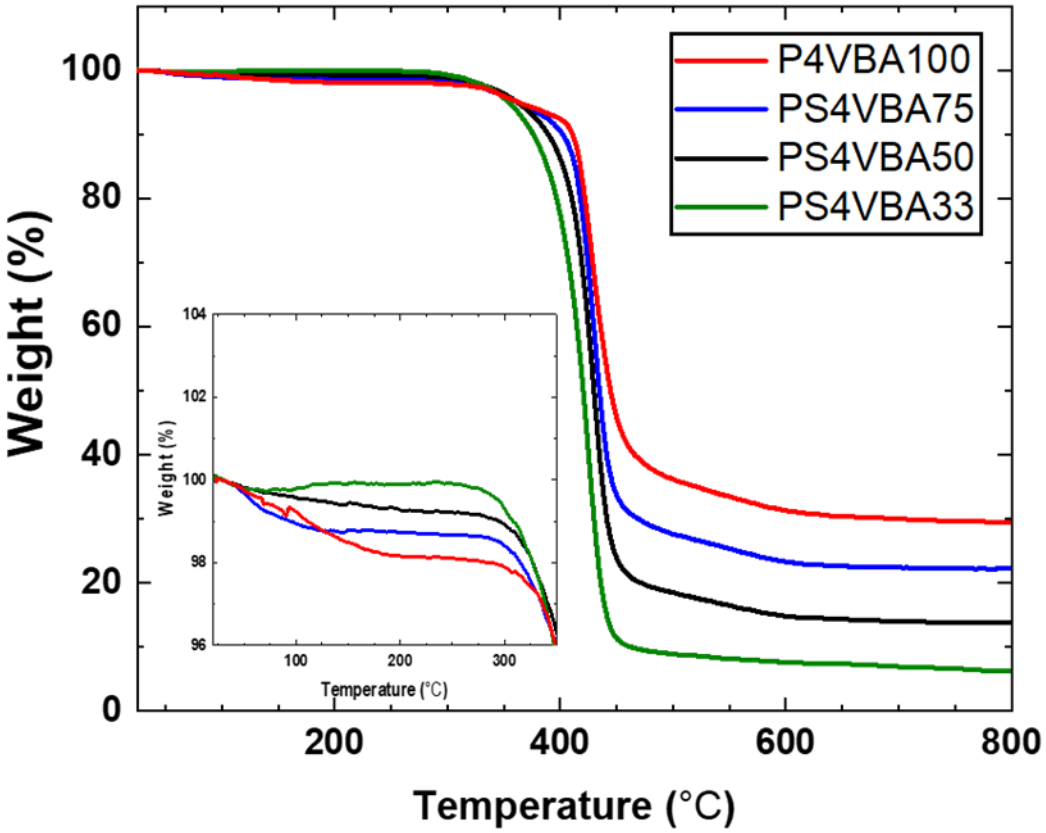

Figure 2.16. TGA thermograms of P4VBA100 (red), PS4VBA75 (blue), PS4VBA50 (black), and PS4VBA33 (green).

2.3.3 The characterization of fabricated polymers thin films

The polymer thin films were prepared by spin-coating technique. The polymer solution was dropped on a clean substrate, and the solvent can be evaporated during the spin-coating process. However, the high boiling point DMF, which is difficult to evaporate at room temperature, was used for polymer dissolution. Therefore, a post-treatment of prepared polymer thin film is required. Figure 2.17a shows the IR spectra of DMF comparing with PS4VBA75. The peak position of C=O in DMF was different from that in PS4VBA75 polymer, in which a peak in PS4VBA75 appeared at a little higher frequency. With this difference, Figure 2.17b (red) confirmed the existence of residue DMF in PS4VBA75 thin film after spin-coated at room temperature. In addition, a small peak of C=O from DMF can be observed along with a C=O peak from PS4VBA75 polymer. However, this small peak from DMF vanished after heated the thin film at 60 °C under vacuum, as shown in Figure 2.17b (blue).

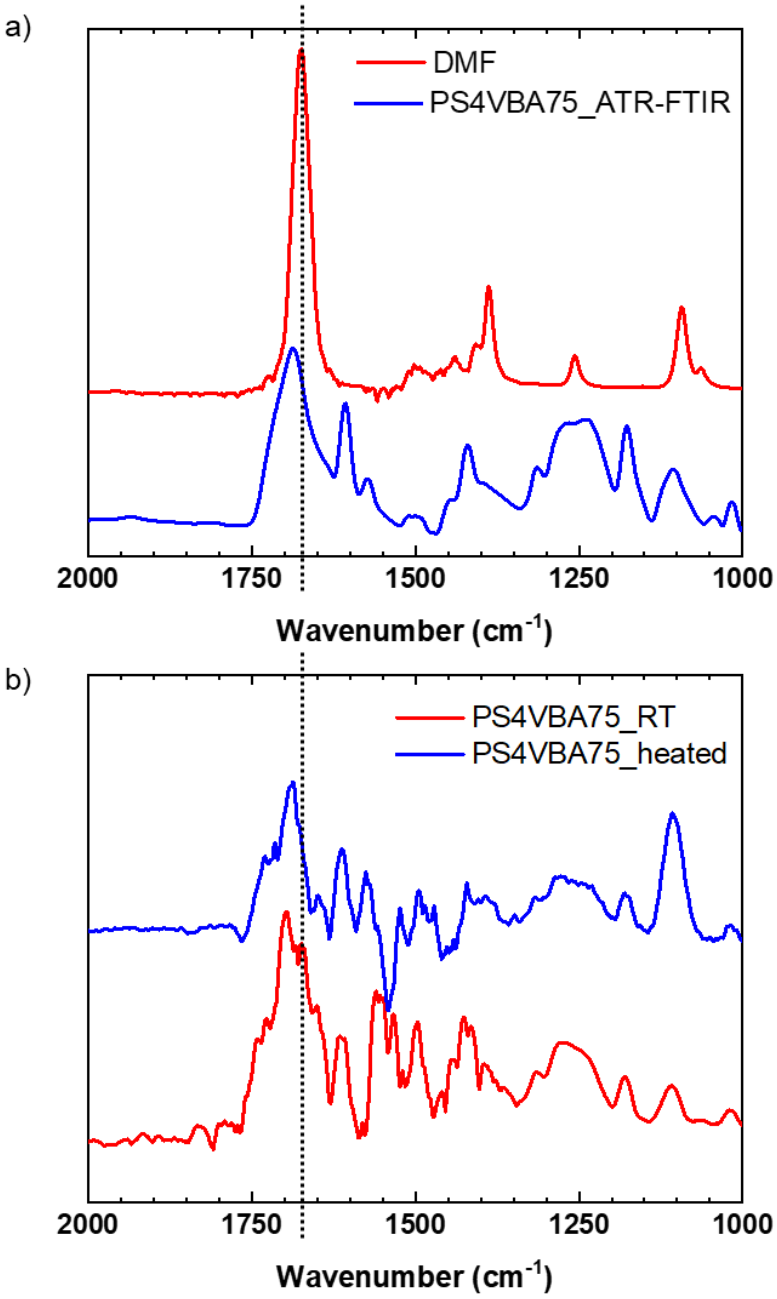

Figure 2.17. a) IR spectra represent the different peak positions of the carboxylic acid group in DMF and PS4VBA75. b) The IR spectra of PS4VBA75 thin film after spin-coated at room temperature (RT) (red) and after heating the film under vacuum at 60 °C (blue).

Moreover, as shown in Figure 2.18, an IR pMAIRS technique was used to examine the polymers' thin-film structure. The different bands' shapes between in-plane (IP)×2 and out-of-plane (OP) directions of the carbonyl (C=O) group from 1670 to 1750 cm^{-1} were observed. The strong absorption band at 1691 cm^{-1} and 1729 cm^{-1} were respectively assigned as the carbonyl groups of carboxylic acids in a cyclic dimer and free carboxylic acid group.[49,50]

In various carboxylic acid concentration polymers, the absorbance ratios of free carboxylic acid groups to cyclic dimer carboxylic acid groups were observed (Table 2.4). The larger the amount of free carboxylic acid groups, the higher the ratio values of polymeric thin films increase with carboxylic acid concentration. This superior amount of free carboxylic acid groups might benefit the internal proton conduction because the free carboxylic acid group can interact with water molecules and facilitate the hydrogen bonding network formation. The lower ratio in polymers with lower carboxylic acid concentrations refers to the thin films' significantly bigger number of cyclic-dimer carboxylic groups. In polymers with lower carboxylic acid concentrations, the increased number of cyclic-dimer carboxylic acid groups may hinder internal proton conduction. Because cyclic dimers do not provide a free proton carrier for long-distance transit, lesser water molecules can engage with carboxylic acid groups to extend the hydrogen bonding network.

By comparing the absorbance ratios of free to dimer carboxylic acid groups with decreasing thicknesses in PS4VBA50 and 33 thin films, the distribution of carboxylic acid groups in thin films was examined. The more influence of the film interfaces region was expected to be found when the film has lower thickness. Figure 2.18 shows that the absorbance ratios increase with decreasing of film thickness in both IP and OP directions. The fact that the free carboxylic acid groups are more concentrated at the interfacial film area is suggested by this film thickness-dependent trend.

The averaged orientational angle, as the angle from the surface normal, from pMAIR spectra was estimated to investigate the molecular orientation of the carboxylic acid group using the following equation.[50]

$$\varphi = tan^{-1}\sqrt{2I_{IP}/I_{OP}} \quad (5)$$

The estimated angles are about 40° for the free carboxylic acid group and about 45° for the dimer carboxylic acid group, respectively. Since the angle of the free carboxylic acid group is far from the magic angle of 54.7°,[51] assuming that the C=O stretching vibration mode is oriented in the thin films. Considering the direction of the C=O stretching vibration mode along with the orientational angle, it is suggested that carboxylic acid groups are oriented in a direction perpendicular to the substrate surface rather than parallel to the substrate since the stronger absorbance was observed in the OP direction. The perpendicular orientation of the carboxylic acid group with respect to the substrate may contribute to proton transport at the interface.

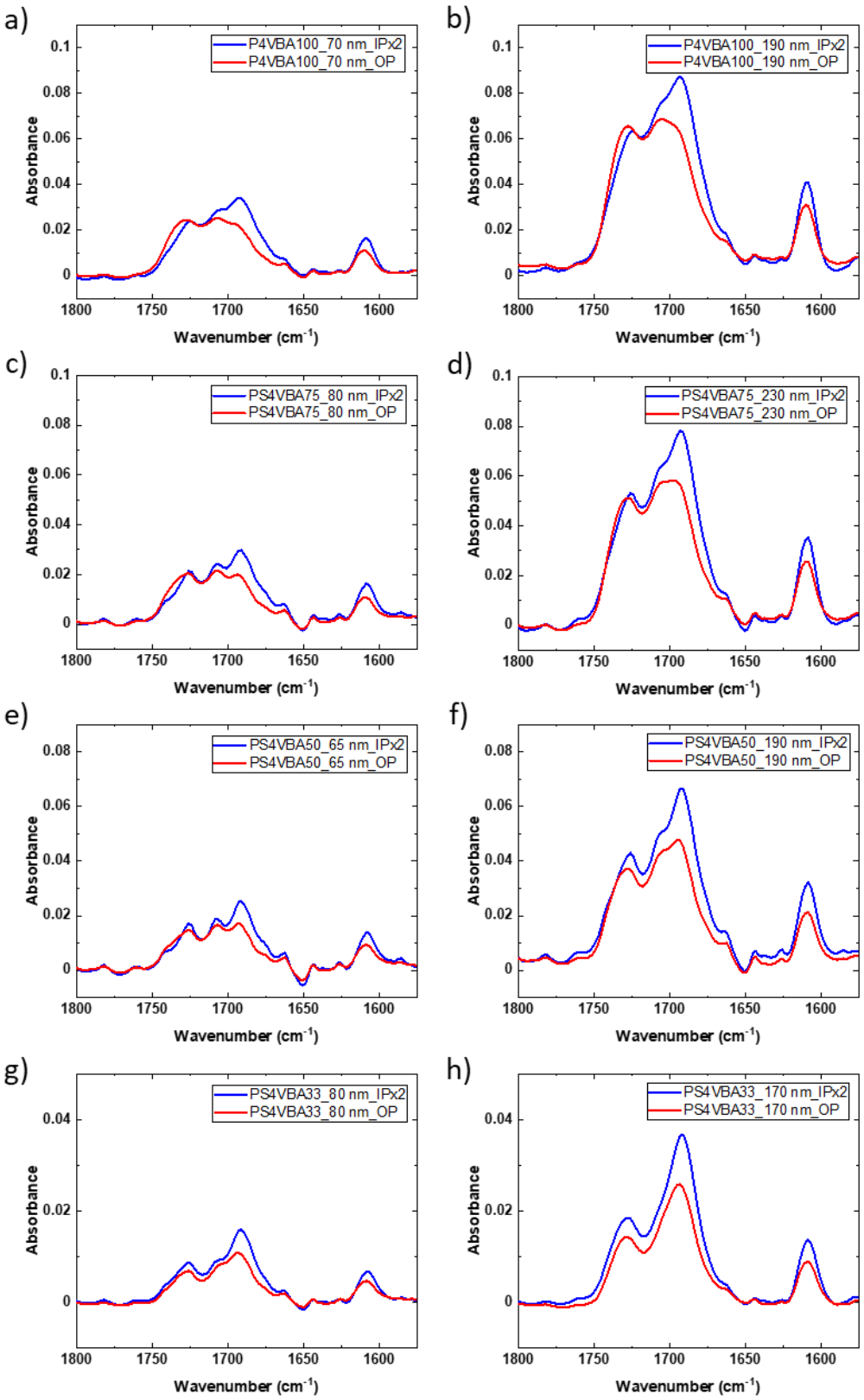

Figure 2.18. IR pMAIR spectra of prepared polymers thin films with various film thicknesses. P4VBA100 a) 70 nm, b) 190 nm; PS4VBA75 c) 80 nm, d) 230 nm; PS4VBA50 e) 65 nm, f) 190 nm; and PS4VBA33 g) 80 nm, h) 170 nm.

Table 2.4 IR pMAIR absorbance ratio of free carboxylic acid groups (1729 cm^{-1}) to dimer carboxylic acid groups (1691 cm^{-1}).

Polymers	Film thickness (nm)	Free to dimer carboxylic acid group absorbance ratio	
		IP×2	OP
P4VBA100	70	0.70	1.17
	190	0.73	1.11
PS4VBA75	80	0.72	1.06
	230	0.68	0.94
PS4VBA50	65	0.67	0.88
	190	0.63	0.79
PS4VBA33	80	0.55	0.65
	170	0.50	0.56

Moreover, C 1s XPS spectra (Figure 2.19) of polymer thin films confirm the various carboxylic acid concentrations at the surface of films. The presence of C-C, C-O, and C=O bands was respectively shown at the binding energy of 284.5 eV, 285.7 eV, and 288.9 eV. The weak band of π-π* interaction presences at a binding energy of 291.0 eV for all polymers. The P4VBA100 polymer with the highest carboxylic acid concentration shows the highest C=O (289±0.1 eV)[52–54] relative intensity, respectively following by PS4VBA75, 50, and 33. Thus, the various carboxylic acid concentrations for each polymer thin film are confirmed by all of the data. We summarize that the free-radical polymerization of styrene-based monomer in ester form was able to control the ester or carboxylic acid concentration in the styrene-based copolymers.

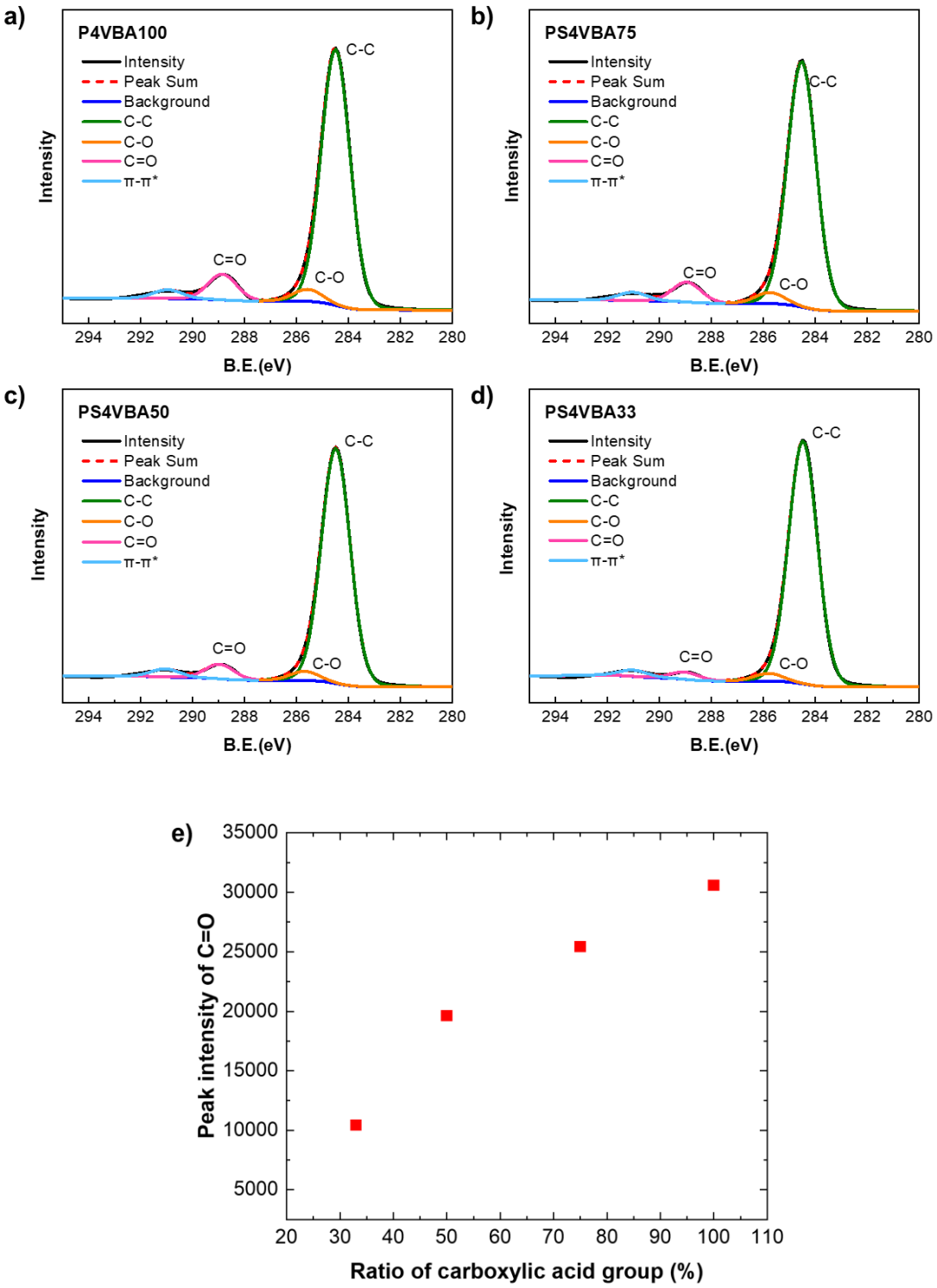

Figure 2.19. XPS spectra of a) P4VBA100, b) PS4VBA75, c) PS4VBA50, and d) PS4VBA33. e) The dependence of XPS peak intensity of C=O on the ratio of the carboxylic acid concentration of synthesized polymers.

2.3.4 Influence of carboxylic acid concentration on water uptake

Because water molecules can form a hydrogen bonding network, the water adsorption behavior of polymers must be considered. These networks operate as a proton-conducting pathway that facilitates proton conduction. The carboxylic acid group can adsorb and interact with water molecules to form the hydrogen bonding network.[4–7,18] Therefore, the presence of the carboxylic acid group in the materials is intended to influence its water uptake behaviors. The water uptake ability of prepared polymers was examined using a QCM system under varied RH. Due to the few water molecules in the atmosphere at low RH, all thin films have identical water adsorption capabilities, as shown in Figure 2.20. After that, increasing the RH resulted in an increase in water uptake. The high carboxylic acid concentration might improve the water uptake of P4VBA100 thin-film by enhancing the film hydrophilicity and providing better extensive hydrogen bonding networks. P4VBA100, on the other hand, has a water uptake that is nearly identical to that of other PS4VBA polymers. For all polymers at 60 % RH, at least one water molecule was adsorbed by half of the carboxylic acid groups. It is also worth noting that when the carboxylic acid concentration rises, the total amount of water molecules adsorb in the polymer thin film. The information mentioned above can be stated as follows: the carboxylic acid groups of all manufactured polymers can adsorb water molecules and may act as a transporter for protons.

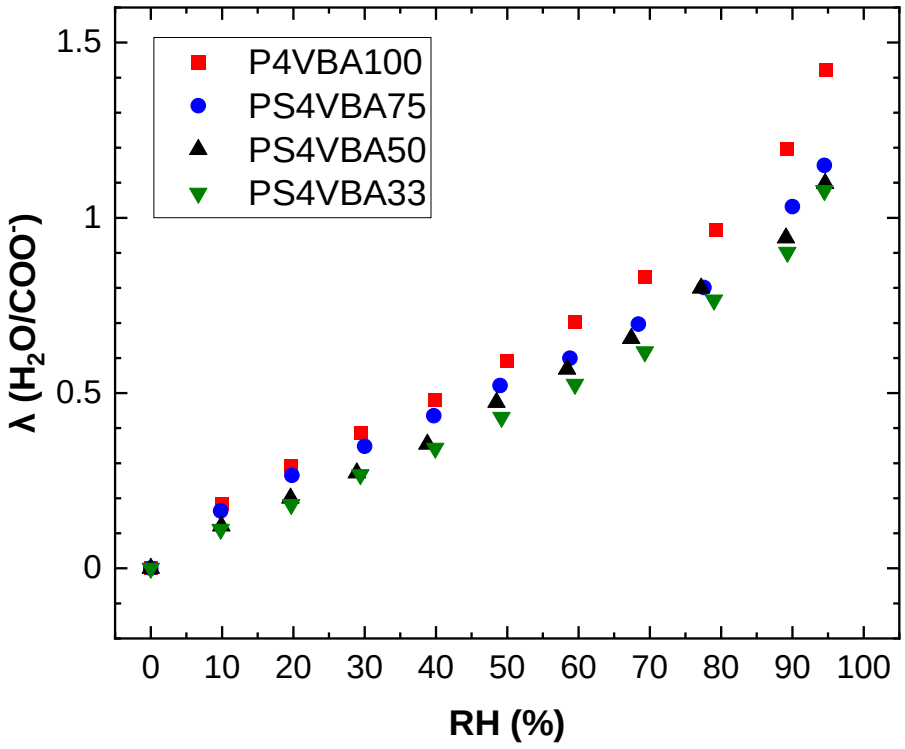

Figure 2.20. The relationship of humidity and the number of adsorbed water molecules per carboxylate group for polymer thin films (70-80 nm): P4VBA100 (red), PS4VBA75 (blue), PS4VBA50 (black), and PS4VBA33 (green).

2.3.5 Influence of carboxylic acid concentration on in-plane proton transport properties of polymer thin films

The effect of carboxylic acid concentrations on proton transport properties was examined using the in-plane proton conductivity of manufactured polymeric thin films. As stated by the water uptake at 60 % RH, 50% of the carboxylic acid groups might be able to adsorb water molecules. As a result, there is a chance that 50% of the proton will dissociate from the carboxylic acid group and become transportable. The interfacial proton conduction might happen in the case of a high pK_a weak carboxylic acid, depending on the concentration of the acid group and the number of adsorbed water molecules. Proton transport at the surface of fully protonated poly(aspartic acid) thin films had previously been reported.[30] Consequently, it is possible that interfacial conductivity occurs in thin films that have been created rather than internal conductivity. The hydration number of four polymer thin films was found to be almost comparable. As a result, the proton transport mechanism and the effect of carboxylic acid concentrations were examined. The interfacial proton conductivity of all-polymer thin films was examined using the same approach. The conductivities of polymer thin films of various thicknesses were then investigated. Figure 2.21 shows the RH dependence of polymer thin films' proton conductivity. Only P4VBA100 has a conductivity independent of film thickness, whereas all PS4VBA thin films have a conductivity dependent on film thickness, with decreased conductivity in thicker films. Internal conductivity is usually expected to be unchanged regardless of film thickness.[30] Therefore, interfacial proton transport must be taken into account.[55,56]

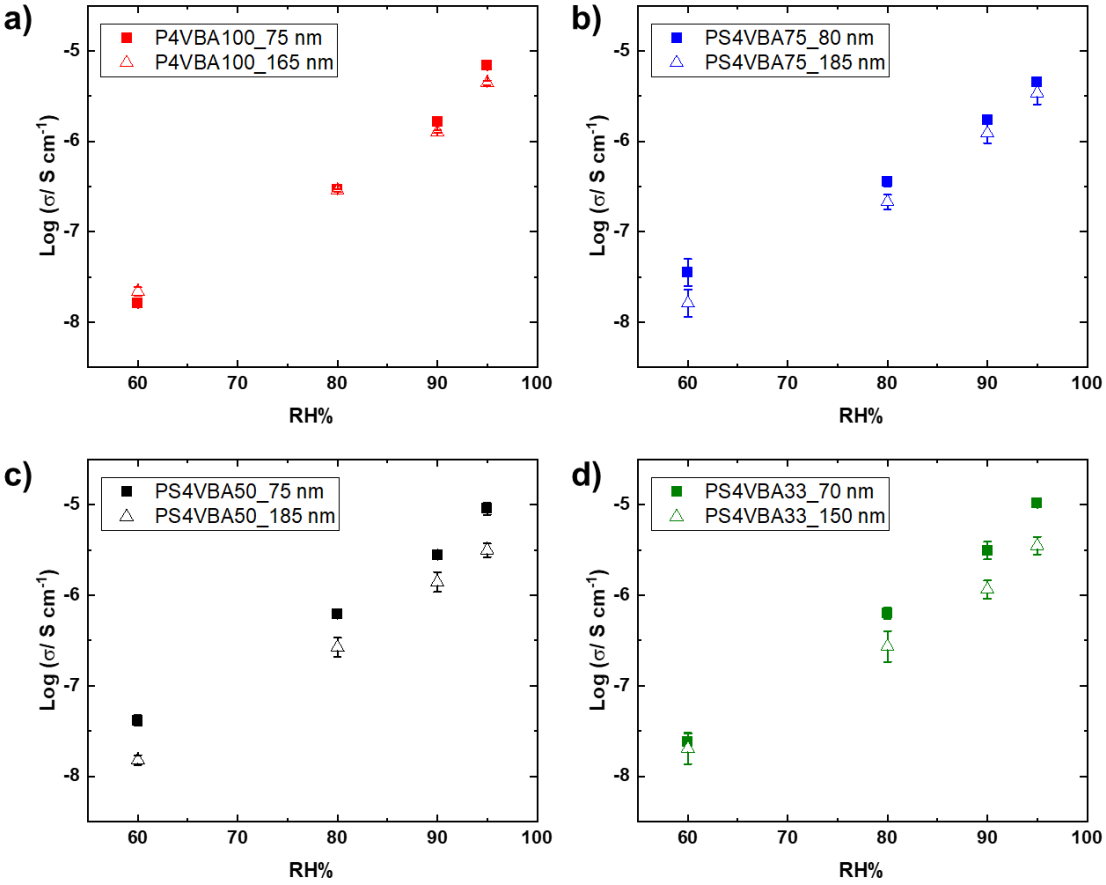

Figure 2.21. Relative humidity dependence of an in-plane proton conductivity for polymer thin films with different film thicknesses: P4VBA100 (red), PS4VBA75 (blue), PS4VBA50 (black), and PS4VBA33 (green).

The normalized resistance or *R*' was then estimated to explain the interfacial proton conduction. Figure 2.22 displays the impact of film thickness on *R*'. As displayed in Figure 2.21, P4VBA100 thin film had a unique tendency than PS4VBA thin films. The *R*' dependence of the film thickness was discovered in P4VBA100, which indicates the internal proton transport. PS4VBA50 and 33, on the other hand, show a similar pattern of film thickness independence. The interfacial proton conduction of PS4VBA50 and 33 films is confirmed by the film thickness dependence of conductivity. It is important to note that PS4VBA75 thin film shows film thickness-dependence of *R*' and proton conductivity (Fig. 2.21). The PS4VBA75 thicker film has lower *R*', which provides both internal and interfacial proton conduction.

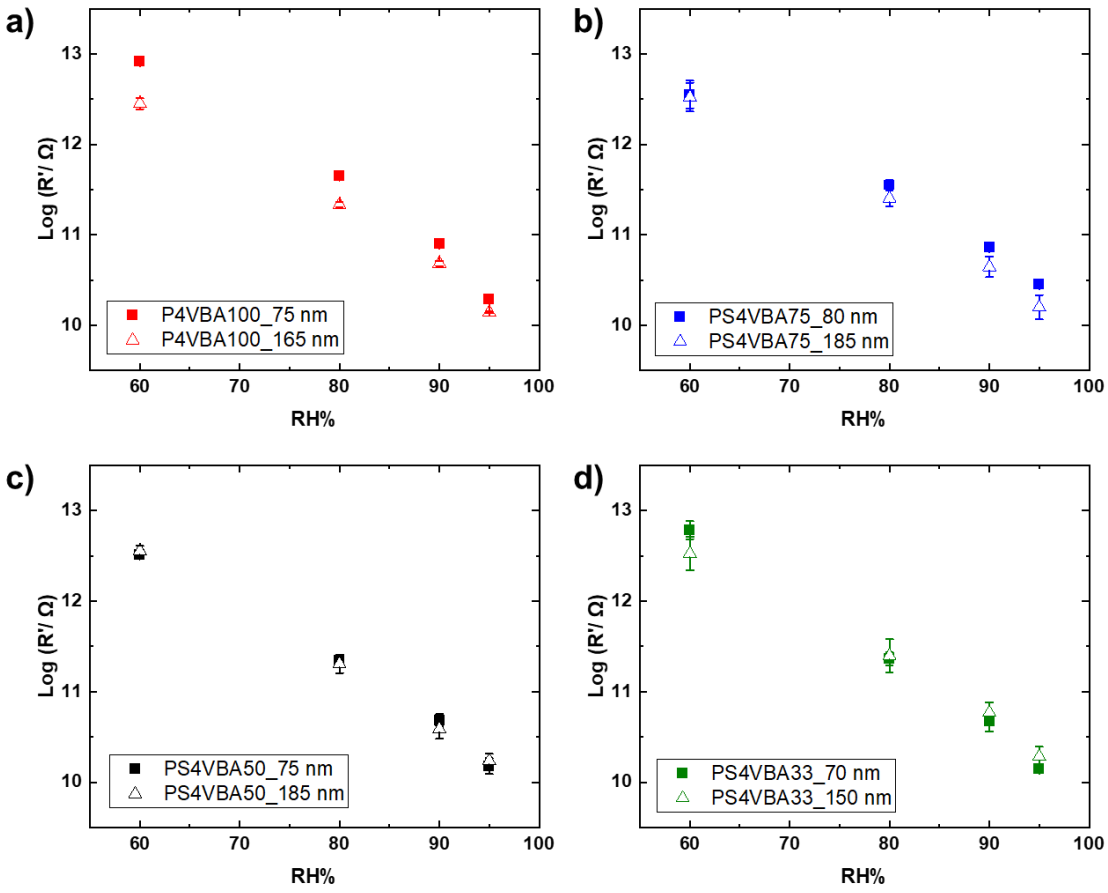

Figure 2.22. Relative humidity dependence of the normalized interfacial resistance for polymer thin films with various film thicknesses: P4VBA100 (red), PS4VBA75 (blue), PS4VBA50 (black), and PS4VBA33 (green).

The presence of a high carboxylic acid group encourages proton carrier density, improves proton transport characteristics.[4] Additionally, the water molecules induce the expansive hydrogen-bonding network and carboxylic acid group dissociation to provide proton carriers.[57] Therefore, it was hypothesized that films with a high carboxylic acid content would have higher proton transport abilities. The conductivity of all polymers was examined at a similar film thickness of 70–80 nm, as shown in Figure 2.23. The RH dependence of proton conductivity was discovered in all polymers which the conductivity enhanced with the increasing of RH. This RH-dependent proton conductivity can be clarified by the improvement of the hydrogen bonding network. When the quantity of water molecules in the polymer thin film grows, the

hydrogen bonding network can extend more effectively under high RH circumstances, promotes proton conduction, and improves proton conductivity. Despite the fact that the proton carrier density was predicted to be variable, the conductivity of all polymers is nearly the same. It is worthy to note that the conductivity shown in Fig. 2.23 originates from different proton conduction pathways. The proton conductivities of PS4VBA50 and 33 films were originated from the interfacial proton conduction. Due to the fewer water molecules and the high number of cyclic dimer carboxylic acid groups, the hydrogen bonding network inside the polymers' film was severed at low RH.

Moreover, free carboxylic acid groups are more positioned at the thin film interfaces. Even though the number of water molecules in the polymers' film increased under higher RH, the continuous hydrogen bonding network was not significantly improved due to the poor density of the carboxylic acid group. Therefore, in low carboxylic acid concentration polymeric thin films such as PS4VBA50 and 33, interfacial proton conduction was dominant for all RH regions. The conductivity of the P4VBA100 thin-film dominantly originated from internal proton conduction. Inside the film, a highly effective hydrogen bonding network can emerge, resulting in internal proton conduction and increased conductivity with RH. In the PS4VBA75 thin film, however, both internal and interfacial proton conduction occurred. Because the lower carboxylic acid content may result in a less efficient hydrogen bonding network inside the film than the P4VBA100 thin film, interfacial conductivity is preferred at low RH. Then, the internal transport happened due to the hydrogen bonding network expansion inside the film at high RH (Fig.2.22b). Furthermore, the internal proton conductivity is influenced by proton carrier density. As shown in Fig. 2.23, at 95% RH, the proton conductivity of PS4VBA75 was lower than that of P4VBA100. The increased proton carrier density of P4VBA100 compared to PS4VBA75 may have influenced the difference in internal proton conductivity, resulting in better internal proton conductivity.

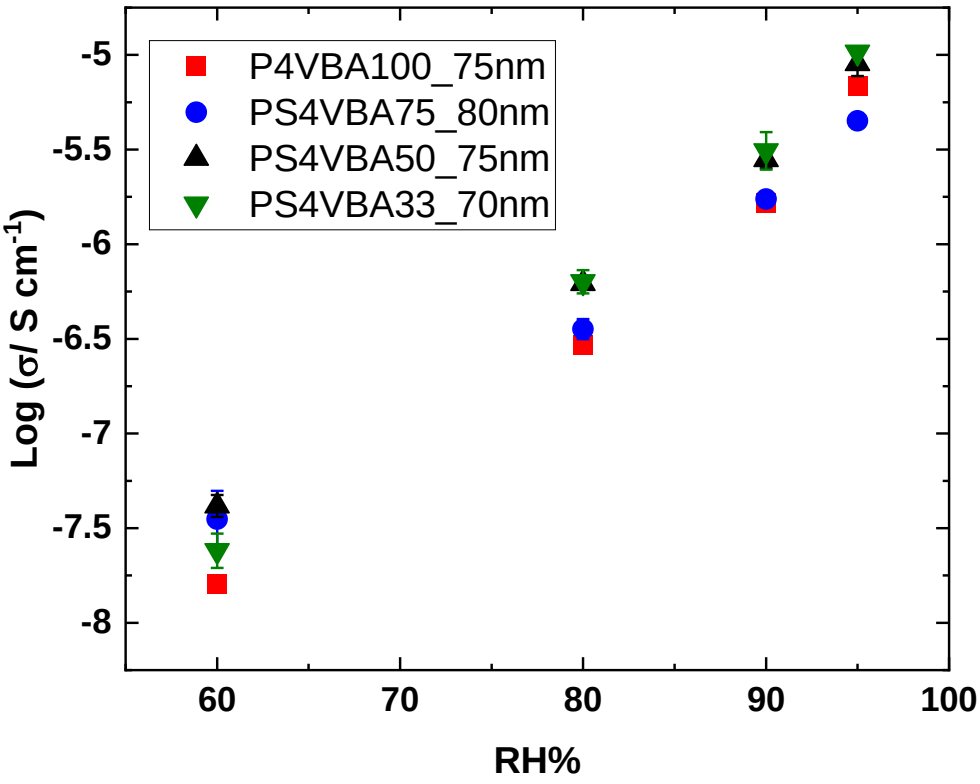

Figure 2.23. Relative humidity dependence of an in-plane proton conductivity for polymer thin films (70-80 nm): P4VBA100 (red), PS4VBA75 (blue), PS4VBA50 (black), and PS4VBA33 (green). It is important to note that the conductivity derives from different proton transport behaviors. The conductivities of PS4VBA50 and 33 were derived from the interfacial proton conduction.

The fact that the results above lead to the supposition of a relationship between carboxylic acid content and the proton transport characteristics is particularly interesting. Table 2.5 shows the summarized main proton conduction pathway of fabricated thin films. The polymer films with high carboxylic acid concentrations, P4VBA100 and PS4VBA75, tend to allow internal proton transport. While the films of lower carboxylic acid concentration polymers, such as PS4VBA50 and 33, prefer interfacial proton conduction over internal proton transport. The carboxylic acid concentration, which affects the water channel or the proton transport pathway, is responsible for this difference in the main proton conduction behavior. A large number of

free carboxylic acid groups in high carboxylic acid concentration polymers (Figure 2.18 and Table 2.4) benefit the hydrogen bonding network formation between water molecules and free carboxylic acid functional groups, thereby facilitating internal proton transport.

Table 2.5. The summarized main proton transport pathway of the synthesized polymer thin films with various carboxylic acid concentrations (+, observed; -, non-observed).

Polymers	Proton transport	
	Internal	Interfacial
P4VBA100	+	-
PS4VBA75	+	+
PS4VBA50	-	+
PS4VBA33	-	+

Low carboxylic acid concentration films with a high amount of cyclic dimer carboxylic acid groups, on the other hand, resulted in poor proton transport channels inside the films, as shown in Figure 2.24. Therefore, the internal proton conduction is not favored in PS4VBA50 and 33 thin films. The interfacial proton transport occurred since the free carboxylic acid is more located at the film's interfaces. On the other hand, PS4VBA75 prefers both internal and interfacial proton conduction. Because of relatively high carboxylic acid concentration, the hydrogen-bonding network can be boosted under high RH. The internal proton transport can also occur together with the interfacial proton transport. This discussion is supported by the fact that the number of free carboxylic acid groups in the film has grown.

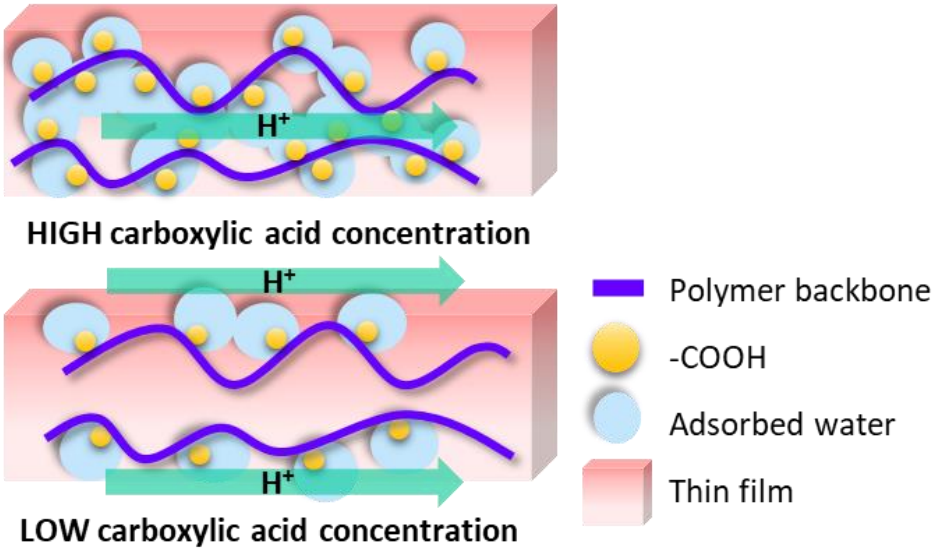

Figure 2.24. Schematic representation of the dependence of main proton transport pathway in polymer thin film on the carboxylic acid group concentration.

The influence of carboxylic acid concentration on the activation energy of polymer thin films was investigated. The conductivity measurement was performed under 90% RH, where P4VBA100 and PS4VBA75 exhibit internal proton conduction, whereas PS4VBA50 and 33 provide interfacial proton conduction. As shown in Figure 2.25, the activation energy of thin films with internal proton conduction has slightly lower activation energy than that of the films with interfacial proton conduction. This trend of higher activation energy in interfacial proton transport thin films might be caused by the low carboxylic acid group density, resulting in more difficulty for proton transportation in the films. While the films with high carboxylic acid concentration, which facilitates the proton conduction under high RH, show lower activation energy. The information above supports the influence of the carboxylic acid group on the proton transport properties of the films.

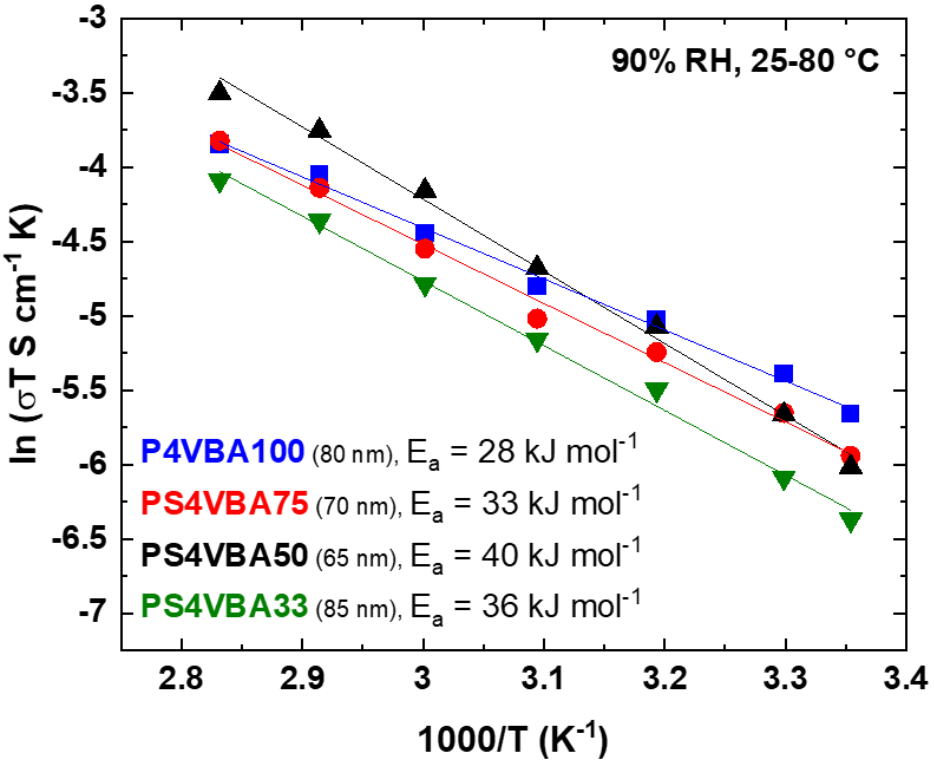

Figure 2.25. Temperature dependence of an in-plane proton conductivity for polymer thin films (65-80 nm): P4VBA100 (red), PS4VBA75 (blue), PS4VBA50 (black), and PS4VBA33 (green).

2.4 Conclusions

Several St-based copolymers were synthesized via free-radical polymerization of ester derivative monomers, ^{1}H-NMR, TGA, and XPS techniques were applied to verify the carboxylic acid concentrations of the prepared polymers. Free and cyclic dimer carboxylic acid groups can be found in the IR pMAIR spectra. In films with larger concentrations of carboxylic acid groups, a superior ratio of free carboxylic acid groups to dimers was identified, facilitating the extension of hydrogen bonding networks in the films. In all thin films, approximately the same number of water molecules were adsorbed per carboxylic acid group, according to the water uptake results. The in-plane proton transport was studied via impedance spectroscopy. The *R*' was also estimated to study the possibility of proton conduction through interfaces. Internal proton transport was observed in the films containing high carboxylic acid concentrations, while interfacial proton transport was found in films containing low carboxylic acid concentrations. The two forms of carboxylic acid groups, free and cyclic dimer, were addressed in connection to differences in proton conduction pathways. Polymers thin films with high carboxylic acid concentration contain appropriate free carboxylic acid groups inside, facilitating an internal proton transport. Low carboxylic acid concentration polymers thin films contain a relatively high number of cyclic dimer carboxylic acid. Interfacial proton conduction is also caused by more free carboxylic acid groups on the film interfaces. The results above show that carboxylic acid concentration in polymers influences the proton transport behavior of the thin films.

References

(1) Selberg, J.; Jia, M.; Rolandi, M. Proton Conductivity of Glycosaminoglycans. *PLoS One* **2019**, *14* (3), 1–8. https://doi.org/10.1371/journal.pone.0202713.

(2) Pena-Francesch, A.; Jung, H.; Hickner, M. A.; Tyagi, M.; Allen, B. D.; Demirel, M. C. Programmable Proton Conduction in Stretchable and Self-Healing Proteins. *Chem. Mater.* **2018**, *30* (3), 898–905. https://doi.org/10.1021/acs.chemmater.7b04574.

(3) Wang, H.; Ma, Y.; Cheng, B.; Kang, W.; Li, X.; Shi, L.; Cai, Z.; Zhuang, X. Solution Blown Biofunctionalized Poly(Vinylidene Fluoride) Nanofibers for Application in Proton Exchange Membrane Fuel Cells. *Electrochim. Acta* **2017**, *258*, 24–33. https://doi.org/10.1016/j.electacta.2017.10.071.

(4) Mondal, S.; Agam, Y.; Amdursky, N. Enhanced Proton Conductivity across Protein Biopolymers Mediated by Doped Carbon Nanoparticles. *Small* **2020**, *2005526* (16), 2005526. https://doi.org/10.1002/smll.202005526.

(5) Mondal, S.; Agam, Y.; Nandi, R.; Amdursky, N. Exploring Long-Range Proton Conduction, the Conduction Mechanism and Inner Hydration State of Protein Biopolymers. *Chem. Sci.* **2020**, *11* (13), 3547–3556. https://doi.org/10.1039/c9sc04392f.

(6) Deng, Y.; Josberger, E.; Jin, J.; Rousdari, A. F.; Helms, B. A.; Zhong, C.; Anantram, M. P.; Rolandi, M. H + -Type and OH - -Type Biological Protonic Semiconductors and Complementary Devices. *Sci. Rep.* **2013**, *3*. https://doi.org/10.1038/srep02481.

(7) Ordinario, D. D.; Phan, L.; Van Dyke, Y.; Nguyen, T.; Smith, A. G.; Nguyen, M.; Mofid, N. M.; Dao, M. K.; Gorodetsky, A. A. Photochemical Doping of

Protonic Transistors from a Cephalopod Protein. *Chem. Mater.* **2016**, *28* (11), 3703–3710. https://doi.org/10.1021/acs.chemmater.6b00336.

(8) Sato, T.; Tsukamoto, M.; Yamamoto, S.; Mitsuishi, M.; Miyashita, T.; Nagano, S.; Matsui, J. Acid-Group-Content-Dependent Proton Conductivity Mechanisms at the Interlayer of Poly(N-Dodecylacrylamide-Co-Acrylic Acid) Copolymer Multilayer Nanosheet Films. *Langmuir* **2017**, *33* (45), 12897–12902. https://doi.org/10.1021/acs.langmuir.7b03160.

(9) Tsuksamoto, M.; Ebata, K.; Sakiyama, H.; Yamamoto, S.; Mitsuishi, M.; Miyashita, T.; Matsui, J. Biomimetic Polyelectrolytes Based on Polymer Nanosheet Films and Their Proton Conduction Mechanism. *Langmuir* **2019**, *35* (9), 3302–3307. https://doi.org/10.1021/acs.langmuir.8b04079.

(10) Kautz, R.; Ordinario, D. D.; Tyagi, V.; Patel, P.; Nguyen, T. N.; Gorodetsky, A. A. Cephalopod-Derived Biopolymers for Ionic and Protonic Transistors. *Adv. Mater.* **2018**, *30* (19), 1–15. https://doi.org/10.1002/adma.201704917.

(11) Nagao, Y.; Naito, N.; Iguchi, F.; Sata, N.; Yugami, H. Synthesis of Oligomeric Poly [(1 , 2-Propanediamine) - Alt - (Oxalic Acid)] and Anomalous Proton Conductivities of the Thin Fi Lms. *Solid State Ionics* **2009**, *180* (6–8), 589–591. https://doi.org/10.1016/j.ssi.2008.09.022.

(12) Li, Q.; Jensen, J. O.; Savinell, R. F.; Bjerrum, N. J. High Temperature Proton Exchange Membranes Based on Polybenzimidazoles for Fuel Cells. *Prog. Polym. Sci.* **2009**, *34* (5), 449–477. https://doi.org/10.1016/j.progpolymsci.2008.12.003.

(13) Yang, C.; Costamagna, P.; Srinivasan, S.; Benziger, J.; Bocarsly, A. B. Approaches and Technical Challenges to High Temperature Operation of

Proton Exchange Membrane Fuel Cells. *J. Power Sources* **2001**, *103* (1), 1–9. https://doi.org/10.1016/S0378-7753(01)00812-6.

(14) Greaves, T. L.; Drummond, C. J. Protic Ionic Liquids: Properties and Applications. *Chem. Rev.* **2008**, *108* (1), 206–237. https://doi.org/10.1021/cr068040u.

(15) Nagao, Y.; Haneda, A.; Naito, N.; Iguchi, F.; Sata, N.; Yugami, H. Synthesis and Protonic Conductivity of the Oligomeric Amides with Different Average Molecular Weights. *Solid State Ionics* **2008**, *179*, 1142–1145. https://doi.org/10.1016/j.ssi.2008.01.051.

(16) Huang, H.; Nia, L.; Xu, S.; Luo, F.; Fan, J.; Li, H.; Wang, H. Novel Proton Exchange Membrane with Long-Range Acid–Base-Pair Proton Transfer Pathways Based on Functionalized Polyethyleneimine. *ACS Sustain. Chem. Eng.* **2021**, *9* (10), 3963–3974. https://doi.org/10.1021/acssuschemeng.1c00154.

(17) Wang, H.; Li, X.; Zhuang, X.; Cheng, B.; Wang, W.; Kang, W.; Shi, L.; Li, H. Modification of Nafion Membrane with Biofunctional SiO2 Nanofiber for Proton Exchange Membrane Fuel Cells. *J. Power Sources* **2017**, *340*, 201–209. https://doi.org/10.1016/j.jpowsour.2016.11.072.

(18) Zhong, C.; Deng, Y.; Roudsari, A. F.; Kapetanovic, A.; Anantram, M. P.; Rolandi, M. A Polysaccharide Bioprotonic Field-Effect Transistor. *Nat. Commun.* **2011**, *2* (1), 2–6. https://doi.org/10.1038/ncomms1489.

(19) Mehta, S. C.; Somasundaran, P.; Maldarelli, C.; Kulkarni, R. Effects of Functional Groups on Surface Pressure - Area Isotherms of Hydrophilic Silicone Polymers. *Langmuir* **2006**, *22* (23), 9566–9571.

https://doi.org/10.1021/la061265f.

(20) Pelto, J. M.; Haimi, S. P.; Siljander, A. S.; Miettinen, S. S.; Tappura, K. M.; Higgins, M. J.; Wallace, G. G. Surface Properties and Interaction Forces of Biopolymer-Doped Conductive Polypyrrole Surfaces by Atomic Force Microscopy. *Langmuir* **2013**, *29* (20), 6099–6108. https://doi.org/10.1021/la4009366.

(21) Sakurai, I.; Kawamura, Y. Lateral Electrical Conduction along a Phosphatidylcholine Monolayer. *Biochim. Biophys. Acta - Biomembr.* **1987**, *904* (2), 405–409. https://doi.org/10.1016/0005-2736(87)90391-9.

(22) Morgan, H.; Martin Taylor, D.; Oliveira, O. N. Proton Transport at the Monolayer-Water Interface. *Biochim. Biophys. Acta - Biomembr.* **1991**, *1062* (2), 149–156. https://doi.org/10.1016/0005-2736(91)90386-M.

(23) Polle, A.; Junge, W. Proton Diffusion along the Membrane Surface of Thylakoids Is Not Enhanced over That in Bulk Water. *Biophys. J.* **1989**, *56* (1), 27–31. https://doi.org/10.1016/S0006-3495(89)82649-9.

(24) Teissié, J.; Prats, M.; Soucaille, P.; Tocanne, J. F. Evidence for Conduction of Protons along the Interface between Water and a Polar Lipid Monolayer. *Proc. Natl. Acad. Sci.* **1985**, *82* (10), 3217 LP – 3221. https://doi.org/10.1073/pnas.82.10.3217.

(25) Leberle, K.; Kempf, I.; Zundel, G. An Intramolecular Hydrogen Bond with Large Proton Polarizability within the Head Group of Phosphatidylserine. An Infrared Investigation. *Biophys. J.* **1989**, *55* (4), 637–648. https://doi.org/10.1016/S0006-3495(89)82861-9.

(26) Blomberg, M. R. A.; Siegbahn, P. E. M. Different Types of Biological Proton

Transfer Reactions Studied by Quantum Chemical Methods. *Biochim. Biophys. Acta - Bioenerg.* **2006**, *1757* (8), 969–980. https://doi.org/10.1016/j.bbabio.2006.01.002.

(27) Georgievskii, Y.; Medvedev, E. S.; Stuchebrukhov, A. A. Proton Transport via the Membrane Surface. *Biophys. J.* **2002**, *82* (6), 2833–2846. https://doi.org/10.1016/S0006-3495(02)75626-9.

(28) Amdursky, N.; Lin, Y.; Aho, N.; Groenhof, G. Exploring Fast Proton Transfer Events Associated with Lateral Proton Diffusion on the Surface of Membranes. *Proc. Natl. Acad. Sci. U. S. A.* **2019**, *116* (7), 2443–2451. https://doi.org/10.1073/pnas.1812351116.

(29) Agam, Y.; Nandi, R.; Bulava, T.; Amdursky, N. The Role of the Protein-Water Interface in Dictating Proton Conduction across Protein-Based Biopolymers. *Mater. Adv.* **2021**, 1739–1746. https://doi.org/10.1039/d0ma00951b.

(30) Nagao, Y.; Kubo, T. Surface Proton Transport of Fully Protonated Poly(Aspartic Acid) Thin Films on Quartz Substrates. *Appl. Surf. Sci.* **2014**, *323*, 19–24. https://doi.org/10.1016/j.apsusc.2014.06.085.

(31) Ono, Y.; Nagao, Y. Interfacial Structure and Proton Conductivity of Nafion at the Pt-Deposited Surface. *Langmuir* **2016**, *32* (1), 352–358. https://doi.org/10.1021/acs.langmuir.5b02623.

(32) Krishnan, K.; Iwatsuki, H.; Hara, M.; Nagano, S.; Nagao, Y. Influence of Molecular Weight on Molecular Ordering and Proton Transport in Organized Sulfonated Polyimide Thin Films. *J. Phys. Chem. C* **2015**, *119* (38), 21767–21774. https://doi.org/10.1021/acs.jpcc.5b03292.

(33) Hutchins, K. M. Functional Materials Based on Molecules with Hydrogen-

Bonding Ability: Applications to Drug Co-Crystals and Polymer Complexes. *R. Soc. Open Sci.* **2018**, *5* (6). https://doi.org/10.1098/rsos.180564.

(34) Heisler, I. A.; Mazur, K.; Yamaguchi, S.; Tominaga, K.; Meech, S. R. Measuring Acetic Acid Dimer Modes by Ultrafast Time-Domain Raman Spectroscopy. *Phys. Chem. Chem. Phys.* **2011**, *13* (34), 15573–15579. https://doi.org/10.1039/C1CP20990F.

(35) Francis, B. R.; Watkins, K.; Kubelka, J. Double Hydrogen Bonding between Side Chain Carboxyl Groups in Aqueous Solutions of Poly (β-L-Malic Acid): Implication for the Evolutionary Origin of Nucleic Acids. *Life* **2017**, *7* (3). https://doi.org/10.3390/life7030035.

(36) Lommerse, J. P. M.; Price, S. L.; Taylor, R. Hydrogen Bonding of Carbonyl, Ether, and Ester Oxygen Atoms with Alkanol Hydroxyl Groups. *J. Comput. Chem.* **1997**, *18* (6), 757–774. https://doi.org/10.1002/(SICI)1096-987X(19970430)18:6<757::AID-JCC3>3.0.CO;2-R.

(37) Besseau, F.; Laurence, C.; Berthelot, M. Hydrogen-Bond Basicity of Esters, Lactones and Carbonates. *J. Chem. Soc. Perkin Trans. 2* **1994**, No. 3, 485–489. https://doi.org/10.1039/P29940000485.

(38) Naddeo, M.; Sorrentino, A.; Pappalardo, D. Thermo-Rheological and Shape Memory Properties of Block and Random Copolymers of Lactide and ε-Caprolactone. *Polymers (Basel).* **2021**, *13* (4), 1–19. https://doi.org/10.3390/polym13040627.

(39) Tripathi, L.; Wu, L. P.; Chen, J.; Chen, G. Q. Synthesis of Diblock Copolymer Poly-3-Hydroxybutyrate -Block-Poly-3-Hydroxyhexanoate [PHB-b-PHHx] by a β-Oxidation Weakened Pseudomonas Putida KT2442. *Microb. Cell Fact.* **2012**,

11 (mcl), 1–11. https://doi.org/10.1186/1475-2859-11-44.

(40) Noble, K. F.; Troya, D.; Talley, S. J.; Ilavsky, J.; Moore, R. B. High-Resolution Comonomer Sequencing of Blocky Brominated Syndiotactic Polystyrene Copolymers Using 13C NMR Spectroscopy and Computer Simulations. *Macromolecules* **2020**, *53* (21), 9539–9552. https://doi.org/10.1021/acs.macromol.0c01630.

(41) Fineman, M.; Ross, S. D. Linear Method for Determining Monomer Reactivity Ratios in Copolymerization. *J. Polym. Sci.* **1950**, *5* (2), 259–262. https://doi.org/https://doi.org/10.1002/pol.1950.120050210.

(42) Yilmaz, E.; Küçükyavuz, Z. Monomer Reactivity Ratios of Styrene-4-Vinylpyridine Copolymers at Low and High Conversions. *Polymer (Guildf).* **1993**, *34* (1), 145–149. https://doi.org/10.1016/0032-3861(93)90297-N.

(43) Ziaee, F.; Nekoomanesh, M. Monomer Reactivity Ratios of Styrene-Butyl Acrylate Copolymers at Low and High Conversions. *Polymer (Guildf).* **1998**, *39* (1), 203–207. https://doi.org/10.1016/S0032-3861(97)00249-8.

(44) Ozaydin-Ince, G.; Coclite, A. M.; Gleason, K. K. CVD of Polymeric Thin Films: Applications in Sensors, Biotechnology, Microelectronics/Organic Electronics, Microfluidics, MEMS, Composites and Membranes. *Reports Prog. Phys.* **2012**, *75* (1). https://doi.org/10.1088/0034-4885/75/1/016501.

(45) Lin, Y. C.; Yu, K. H.; Huang, S. L.; Liu, Y. H.; Wang, Y.; Liu, S. T.; Chen, J. T. Alternating Ethylene-Norbornene Copolymerization Catalyzed by Cationic Organopalladium Complexes Bearing Hemilabile Bidentate Ligands of α-Amino-Pyridines. *Dalt. Trans.* **2009**, No. 41, 9058–9067. https://doi.org/10.1039/b912068h.

(46) Hanumansetty, S.; O'Rear, E.; Resasco, D. E. Encapsulation of Multi-Walled Carbon Nanotubes with Copolymer to Disperse in Aqueous Media. *J. Polym. Res.* **2017**, *24* (12), 1–10. https://doi.org/10.1007/s10965-017-1363-8.

(47) Abreu, A. S.; Oliveira, M.; Rodrigues, P. V.; Moura, I.; Botelho, G.; Machado, A. V. Synthesis and Characterization of Polystyrene-Block-Poly(Vinylbenzoic Acid): A Promising Compound for Manipulating Photoresponsive Properties at the Nanoscale. *J. Mater. Sci.* **2015**, *50* (7), 2788–2796. https://doi.org/10.1007/s10853-015-8835-1.

(48) Yang, Y.; Li, H.; Zhang, Y.; Wang, H.; Xu, L.; Zhao, H. Poly(p-Vinylbenzoic Acid)-Block-Polystyrene Self-Assembled Structures as Templates in the Synthesis of ZIF-8. *Chem. - An Asian J.* **2017**, *12* (7), 753–758. https://doi.org/10.1002/asia.201700011.

(49) Hasegawa, T. Advanced Multiple-Angle Incidence Resolution Spectrometry for Thin-Layer Analysis on a Low-Refractive-Index Substrate. *Anal. Chem.* **2007**, *79* (12), 4385–4389. https://doi.org/10.1021/ac070676d.

(50) Hasegawa, T. A Novel Measurement Technique of Pure Out-of-Plane Vibrational Modes in Thin Films on a Nonmetallic Material with No Polarizer. *J. Phys. Chem. B* **2002**, *106* (16), 4112–4115. https://doi.org/10.1021/jp013751b.

(51) Hasegawa, T.; Takeda, S.; Kawaguchi, A.; Umemura, J. Quantitative Analysis of Uniaxial Molecular Orientation in Langmuir-Blodgett Films by Infrared Reflection Spectroscopy. *Langmuir* **1995**, *11* (4), 1236–1243. https://doi.org/10.1021/la00004a032.

(52) Xiao, S.; Xu, P.; Peng, Q.; Chen, J.; Huang, J.; Wang, F.; Noor, N. Layer-by-Layer Assembly of Polyelectrolyte Multilayer onto PET Fabric for Highly

Tunable Dyeing Withwater Soluble Dyestuffs. *Polymers (Basel).* **2017**, *9* (12). https://doi.org/10.3390/polym9120735.

(53) Hamilton, R. F.; Wu, N.; Xiang, C.; Li, M.; Yang, F.; Wolfarth, M.; Porter, D. W.; Holian, A. Synthesis, Characterization, and Bioactivity of Carboxylic Acid-Functionalized Titanium Dioxide Nanobelts. *Part. Fibre Toxicol.* **2014**, *11* (1), 1–15. https://doi.org/10.1186/s12989-014-0043-7.

(54) Yu, S.; Liu, J.; Zhu, W.; Hu, Z. T.; Lim, T. T.; Yan, X. Facile Room-Temperature Synthesis of Carboxylated Graphene Oxide-Copper Sulfide Nanocomposite with High Photodegradation and Disinfection Activities under Solar Light Irradiation. *Sci. Rep.* **2015**, *5* (November). https://doi.org/10.1038/srep16369.

(55) Schoonman, J. Nanoionics. *Solid State Ionics* **2003**, *157* (1), 319–326. https://doi.org/10.1016/S0167-2738(02)00228-X.

(56) Maier, J. Defect Chemistry and Ionic Conductivity in Thin Films. *Solid State Ionics* **1987**, *23* (1–2), 59–67. https://doi.org/10.1016/0167-2738(87)90082-8.

(57) Wu, G. D.; Zhou, H. L.; Fu, Z. H.; Li, W. H.; Xiu, J. W.; Yao, M. S.; Li, Q. hong; Xu, G. MOF Nanosheet Reconstructed Two-Dimensional Bionic Nanochannel for Protonic Field-Effect Transistors. *Angew. Chemie - Int. Ed.* **2021**, 1–6. https://doi.org/10.1002/anie.202100356.

Chapter 3

The development of the parallel-shaped field-effect transistor electrodes for alternative current impedance measurement

Abstract

The investigation of proton transport properties is essential for better understanding the various biological systems. The use of protonic field-effect transistors (H^+-FETs), which an applied voltage can modulate the proton transport, is a promising candidate for bridging biological and electronic systems. In previous H^+-FETs, the protonic current was generated from a PdH_x electrode under the H_2 atmosphere and a direct current (DC). This Pd electrode reaction might affect the electrical properties of proton conductive material in H^+-FETs. Therefore, in this study, the electrical properties measurement of relatively low proton conductivity material in devices with Au electrode and alternative current (AC) was newly developed to avoid the effect of electrode reaction. Compared to the DC method, the AC method gives us more information and separation of each component depending on the frequency. The H^+-FET-like devices were designed as a small parallel-shaped of 500-750 µm width and 50-150 µm length, named PFET. The fabricated weak-acid functionalized styrene-based copolymer's electrical properties from the previous chapter were successfully investigated using Au electrodes and AC-impedance measurement. However, due to the relatively low proton conductivity and high resistance of the fabricated polymer thin film, the electrical response of polymer thin film was dominated by the electrode/ polymer thin film interfacial response. In order to improve the H^+-FETs performance, the modification of PFETs design with short channel length and wide channel width or long electrode length was expected to reduce the resistance of polymer thin film.

3.1 Introduction

Proton transport plays an essential role in many biological systems.[1–14] To understand more insight into proton transport in biological systems, the investigation of proton transport is necessary. Protonic field-effect transistors (H^+-FETs) have recently received much attention from the researcher because of their ability in the proton transport controlling through an applied voltage.[15–19] With this reason, the H^+-FETs are promising candidates for bridging biological and electronic systems.[18–21] As shown in Figure 3.1, the H^+-FETs also consist of three electrodes of source (S), drain (D), and gate (G) as same as other types of FETs, but the charge carrier in this device is positive charge protons (H^+) instead of electrons.[19] Therefore, the proton conductive materials that can support proton conduction are critical parts of H^+-FETs.

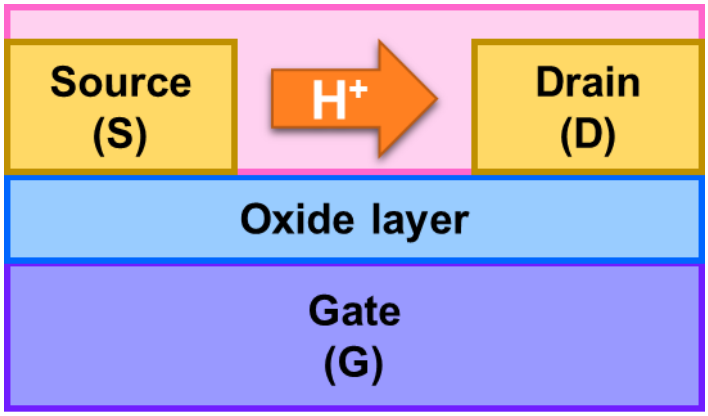

Figure 3.1 The schematic represents protonic field-effect transistor (H^+-FETs). The pink area represents the proton conductive material. The yellow part denotes the metal electrode. The blue and purple areas represent the insulating oxide layer (i.e., SiO_2) and a gate electrode.

The H^+-FETs with biopolymers that can support the proton transport have been intensively investigated. Zhong et al. developed a polysaccharide-based bioprotonic transistor that can conduct proton (H^+).[20] Deng and co-workers fabricated an H^+-FET with a maleic-chitosan as an active layer.[22] The H^+-FETs with a reflectin film containing amino acid groups were reported.[18,23] The proton conductivity of electrospun chitosan nanofibers in FETs was also

reported.[19] However, the critical part of these devices is a pair of palladium (Pd) electrodes, hydrogen (H_2) atmosphere, and direct current (DC) because the Pd electrodes can react with H_2 and continuously provide protons as charge carriers by forming PdH_x, as shown below.[19,21,22,24]

$$PdH_x \rightleftharpoons Pd + H^+ + e^-$$

Therefore, this Pd electrode reaction is necessary for the relatively low proton conductivity materials, including biopolymers. However, the proton produced by the Pd electrode reaction as an extra proton might affect the amount of proton carrier or proton carrier density of conductive material, which might also affect the electrical properties of proton conductive materials.[20]

In this study, to avoid the effect of the electrode reaction, the gold (Au) was selected as an electrode material since Au is considered as one of the suitable contact metal FET with no significant contribution from electrode reaction.[25,26] And the impedance measurement was performed under an alternative current (AC) for electrical properties investigation. In this case, the effect of the extra proton carrier produced by the Pd electrode reaction on the material's electrical properties can be prevented. Therefore, the development of proton transport properties investigation in H^+-FET using Au electrodes and AC conditions is challenging and promising. The H^+-FETs with small parallel-shaped channels were designed and named as PFETs. The relatively low proton conductivity carboxylic acid functionalized styrene-based copolymers from the previous chapter were applied to the FETs, and the electrical properties of these H^+-FETs were studied. The carboxylic acid functionalized polymers are suitable for application with PFETs due to their low water adsorption ability, leading to less suffering from the swelling effect of polymer thin film.

3.2 Materials and methods

3.2.1 Materials

Silicon wafer (Si-wafer) with 100 nm thick thermal oxide insulating layer and <100> crystal direction was purchased from Seiren KST Corp., Japan. The Microposit™ LOL™ 2000 liftoff layers and Microposit™ remover 1165 were purchased from Dow Chemical Company. Positive photoresist TSMR-8900 and tetramethylammonium hydroxide (NMD-W, 2.38% w/w) were purchased from Tokyo Ohka Kogyo Co., Ltd. Acetone (99.8%, EL grade) was purchased from Kanto Chemical Co., Inc. Hydrofluoric acid (HF, 48 wt% in H_2O) was purchased from Sigma-Aldrich Co., LLC. All the chemicals were used as received. The fabricated proton conductive polymer functionalized with a carboxylic acid group from Chapter 2, PS4VBA50, was used in this chapter study.

3.2.2 PFETs pattern design

The parallel-shaped channel FET or PFETs were designed with two parallel electrodes, as shown in Figure 3.2a. Figure 3.2b shows the pattern designed using Autodesk AutoCAD 2021. The channel length of 150, 100, and 50 µm and width of 750, 500, and 300 µm were chosen. As shown in Figure 3.2, the PFETs were designed on the substrate size of 2 cm × 2 cm and the electrodes were designed with a long straight line of 0.4 mm and a small square for the electrical connection.

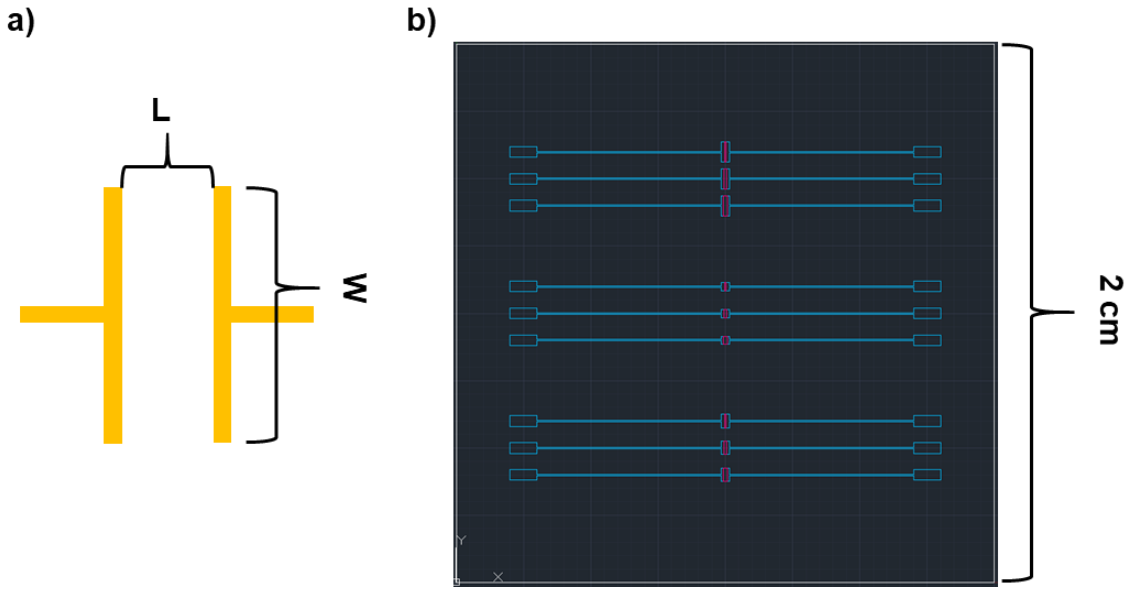

Figure 3.2 a) The schematic shows the design of PFET's channel shape. b) The pattern design of PFETs with the channel length 150,100 and 50 µm, and channel width of 750, 500, and 300 µm on the area of 2 cm × 2 cm.

3.2.3 Preparation of PFETs

The surface of the Si wafer was cleaned by plasma treatment (FA-1 plasma etching system; Samco) of 15 W for 3 min. The liftoff material, MICROPOSIT™ LOL™ 2000, was spin-coated (1H-DX2 Mikasa spincoater; Mikasa) on the Si-wafer then baked on a hot plate at 180°C for 3 min. The photoresist, TSMR-8900, was then spin-coated on top of the liftoff material layer then baked on a hot plate at 110°C for another 1.5 min. After cooled down, the prepared wafer was protected from ultraviolet (UV) light by wrapping it with aluminum foil. The photolithography was done using the radiation wavelength of 504 nm on the designed electrode pattern area. The exposure parts of photoresist and liftoff material layers were washed away with 2.38% w/w NMD-W solution for 55 seconds, followed by rinsing with water for a minute and dried with a nitrogen blower. Then the devices' surface was cleaned again by plasma treatment at 50 W for 1 min.

The source (S) and drain (D) metal electrodes were prepared by radio frequency (RF) sputtering technique. A layer of titanium (Ti) was sputtered as a first layer, followed by a gold

(Au) layer, in which the total thickness of the metal electrode is 180 nm. The non-electrode part was removed by immersed in MICROPOSIT™ remover 1165 at 80°C. Figure 3.3 shows the PFETs preparation from the photolithography process (Mark Less Aligner, Heidelberg Instruments MLA150) to wash photoresist and liftoff material. After that, the devices were sonicated in acetone, rinsed with water, and dried with a nitrogen blower. Each set of devices on the Si-wafer was separated in the size of 3.5 cm × 3.5 cm. A small part of the SiO_2 layer at the edge of the Si wafer substrate was etched by buffered HF for the gate (G) connection. The metal electrode thickness was examined using a step profiler (Alphastep D-500).

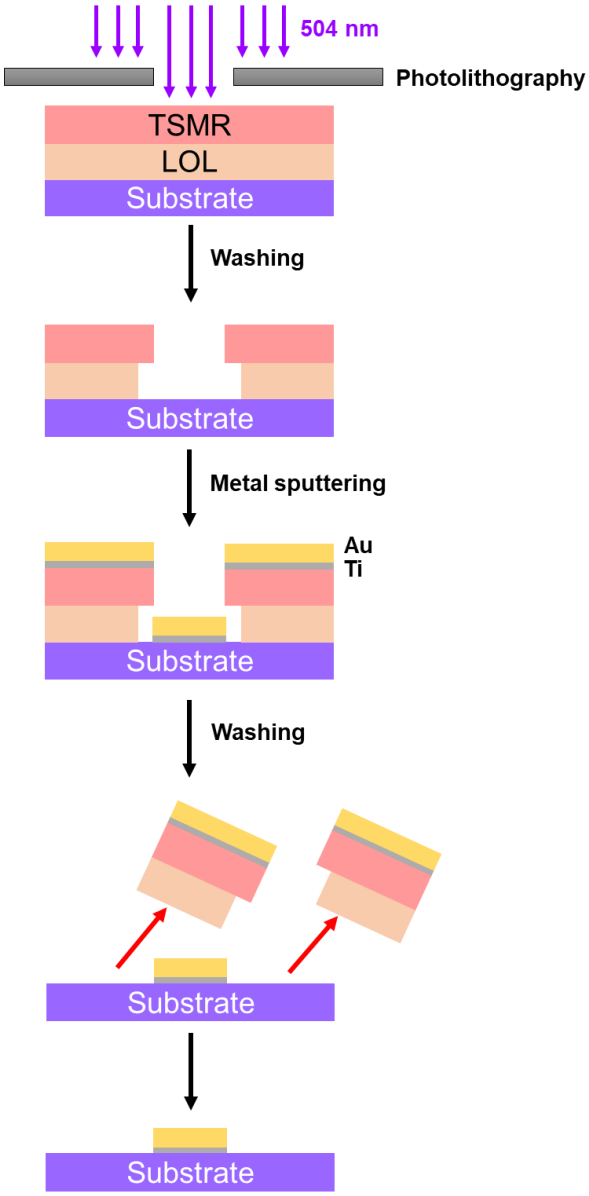

Figure 3.3 The schematic diagram represents the electrode patterning process.

3.2.4 Preparation of polymer thin film on PFETs

The surface of PFET was cleaned by the plasma treatment before use. Then the polymer functionalized with a carboxylic acid group, PS4VBA50, was dissolved, spin-coated, and dried on the prepared PFETs using the same procedure as in Chapter 2. The polymer thin films were prepared with a similar thickness of 70-80 nm. The excess film outside the channel and gate (G) area was removed using methanol as a solvent, as shown in Figure 3.4.

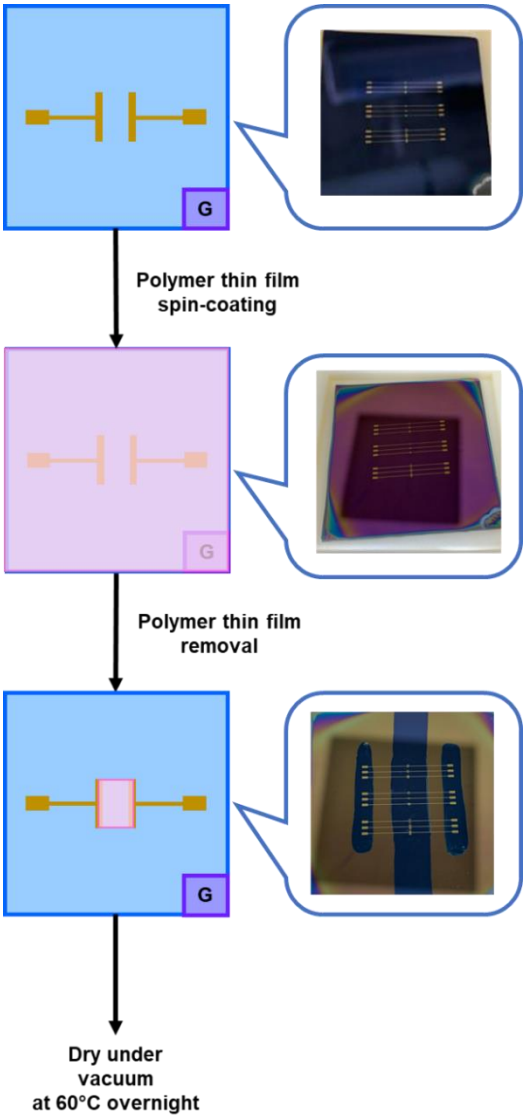

Figure 3.4 The schematic diagram represents the thin film preparation on the PFETs process. The pink, gold, and blue areas represent proton conductive polymer thin film, electrodes, and silicon wafer substrate, respectively. The small area of SiO_2 at the edge of the substrate as a gate (G) was removed.

3.2.5 Proton conductivity measurements

The polymer thin film's proton conductivity on PFET was investigated in the relative humidity (RH)-controlled and temperature-controlled chamber (SH-221; Espec Corp.) using an AC-impedance spectroscopy measurement system obtained with a frequency response analyzer equipped with a high-frequency dielectric interface (SI1260 and SI1293; Solartron Analytical). Both electrodes were connected with Au wire and substrate holder using a porous gold paste, as shown in Figure 3.5. The gate electrode (G) was connected with Au wire by porous paste for the S-G resistivity measurement.

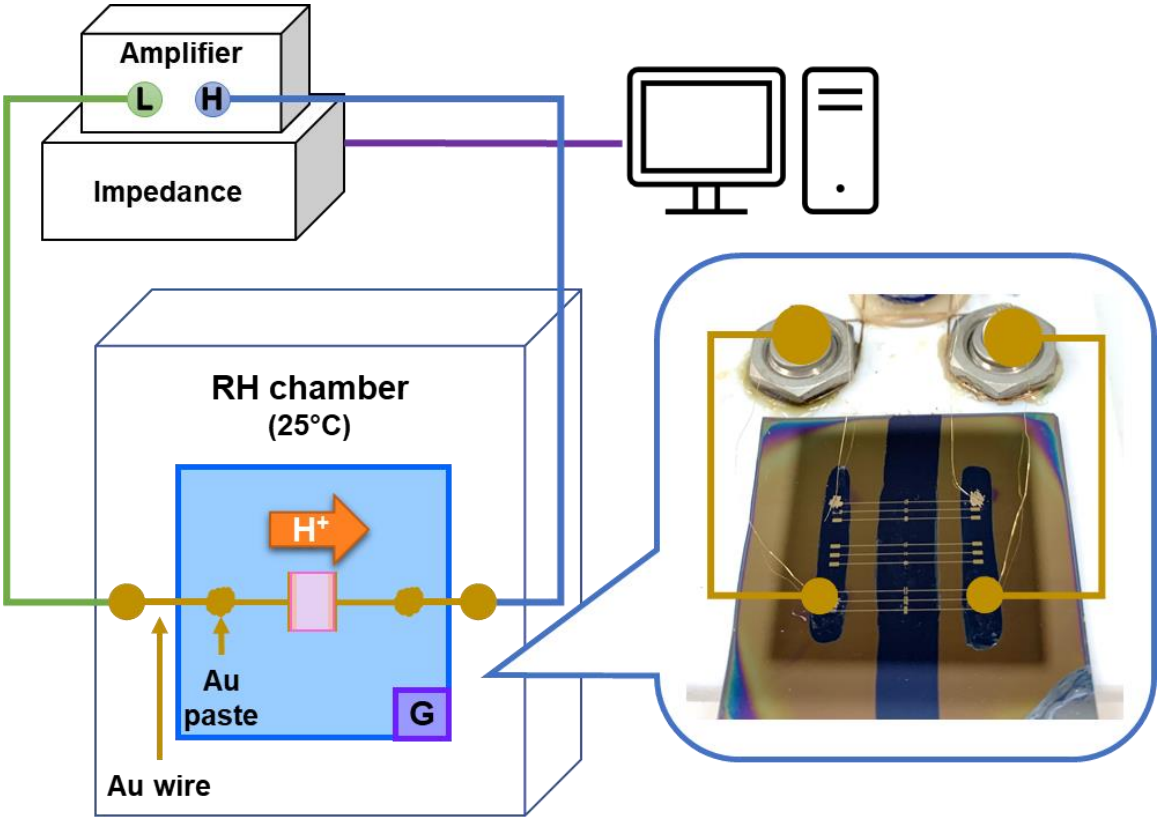

Figure 3.5 The schematic displays the impedance measurement setup for study the electrical properties of PFETs.

3.3 Results and discussion

3.3.1 The preparation of PFETs

The PFETs with parallel-shaped electrodes were successfully fabricated on Si-wafer substrate, as shown in Figure 3.6a. The thickness of the Ti and Au sputtered electrode was examined using a step profiler. Figure 3.6b shows the thickness profile of the metal electrode, which is around 180 nm.

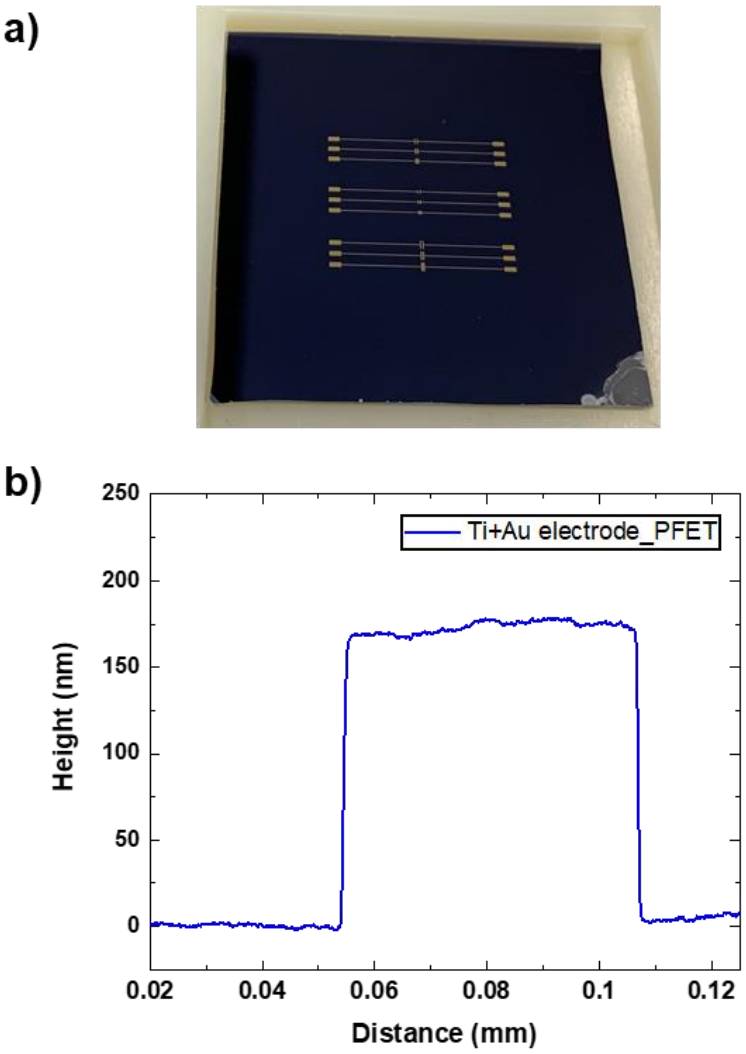

Figure 3.6. a) The image of prepared PFETs. b) The thickness of metal deposited electrode on PFET measured by step profiler.

3.3.2 Electrical properties of weak-acid functionalized styrene-based copolymer thin films in PFETs

3.3.2.1 The impedance response in PFETs

The electrical properties of polymer thin film on PFETs with different channel sizes were successfully investigated using an AC-impedance spectroscopy measurement system. Figure 3.7 shows the Nyquist plots of PS4VBA50 thin film on 500×50 and 750×150 PFETs. According to the polymer thin film's resistance on quartz substrate from Chapter 2, the expected resistance of the film on 500×50 and 750×150 PFETs at 60%RH were around 3×10^{11} Ω and 6×10^{11} Ω, respectively. However, the impedance response of PS4VBA50 thin films on both PFETs channel sizes did not show the semicircle response. Usually, the impedance response of conductive materials should have shown a semicircle response at the high-frequency region and a vertical-line-like response at the low-frequency region.[27–33] The semicircle response provides the film resistance and capacitance, while the vertical-line-like response represents the capacitive behavior.[25,33–38] The electrical properties of polymer thin film as the resistance and capacitance can be observed from the semicircle response, which changes with temperature, film thickness, chemical atmosphere, and RH.[25] The observed vertical-line-like response of PS4VBA50 thin film on PFETs may be caused by the polymer thin film's high resistance and low conductivity, as predicted above according to the previous chapter data. Figure 3.8 shows the impedance and capacitance, which are possible to present in our measurement.[25,39] R_f and C_f respectively represent the resistance and capacitance of polymer thin film. The resistance originating from the Au wire connection was assigned as R_s. It is necessary to consider the Si-wafer substrate and interface region between Au electrode and Si-wafer substrate. R_{eSi} and C_{eSi} are the resistance and capacitance of the Au electrode/ Si-wafer substrate interface. The resistance of the Si-wafer substrate (R_{Si}) is significantly high, so only the SiO_2 capacitance of the substrate (C_{Si}) was considered. The response from the polymer thin films in Figure 3.7 might be dominated by the double layer capacitance response between polymer thin film and Au electrode interface (C_{fe}), as shown in Figure 3.8. R_{fe} could be ignored because the faradaic charge across the interface was negligible since Au is a non-

reactive electrode and acts as a blocking electrode.[25] Therefore, due to the high resistance, only C_{fe} can be observed at this interface region.

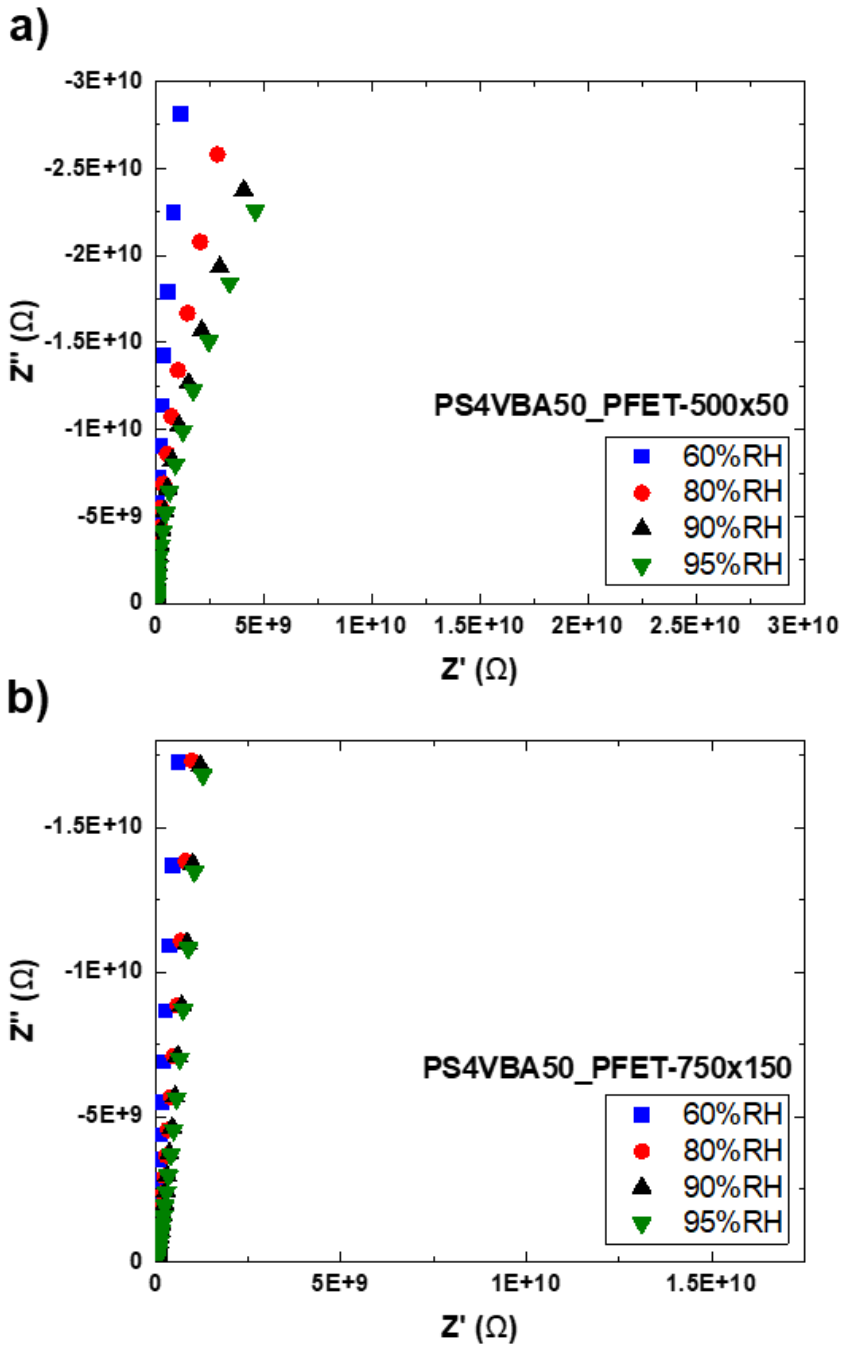

Figure 3.7 The Nyquist plots of PS4VBA50 thin film at various RH on the PFETs with the channel size of a) 500 µm width and 50 µm length (500×50) and b) 750 µm width and 150 µm length (750×150).

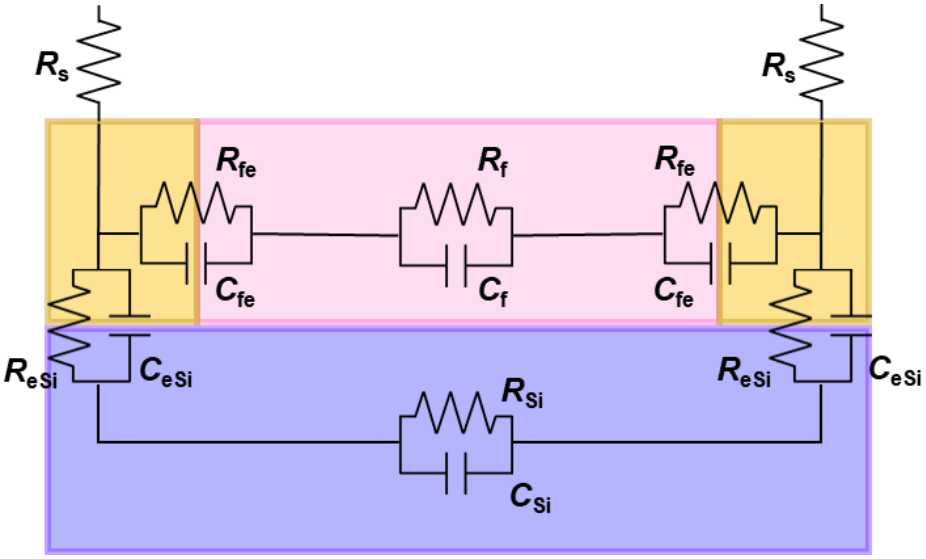

Figure 3.8 The schematic represents the possible impedance and capacitance components in the polymer thin film on silicon wafer (Si-wafer) substrate with gold electrodes. Yellow, pink, and purple areas represent the gold electrodes, proton conductive polymer thin film, and SiO_2 layer of Si-wafer substrate, respectively. *R* and *C* denote resistance and capacitance, respectively. R_s represent a serial resistance originated from the electrode contact. The subscripted f and Si represent the *R*/ *C* of the film and SiO_2 layer, respectively. The *R* and *C* of the interfacial region between the polymer film/ Au electrode were written as R_{fe} and C_{fe}. R_{eSi} and C_{eSi} denote the *R* and *C* of Au electrode/ Si-wafer substrate.[25,39]

It is essential to consider the resistance of the dielectric layer (R_{eSi}). If the impedance response was obtained from the dielectric layer, the impedance response from PFETs with different channel lengths should be the same. In contrast, the impedance response should change with the device's channel length if the response was derived from the polymer thin film. The PFETs with the same channel width of 750 µm but different channel lengths of 50 and 150 µm were examined, as shown in Figure 3.9. The change of impedance response with PFET's channel length while the channel width was fixed referring to the impedance responses of the polymer thin film. However, even at high RH, where the conductivity of polymer thin film was expected to be improved, the semicircle response still cannot be observed in both PFETs. Therefore, even both PFETs with a smaller channel size of 500 µm

width and 50 µm length (500×50) and a larger channel size of 750 µm width and 150 µm length (750×150) tend to show the RH dependence response, referring to the response obtained from the polymer thin film, the resistance of polymer thin film (R_f) could not be estimated.

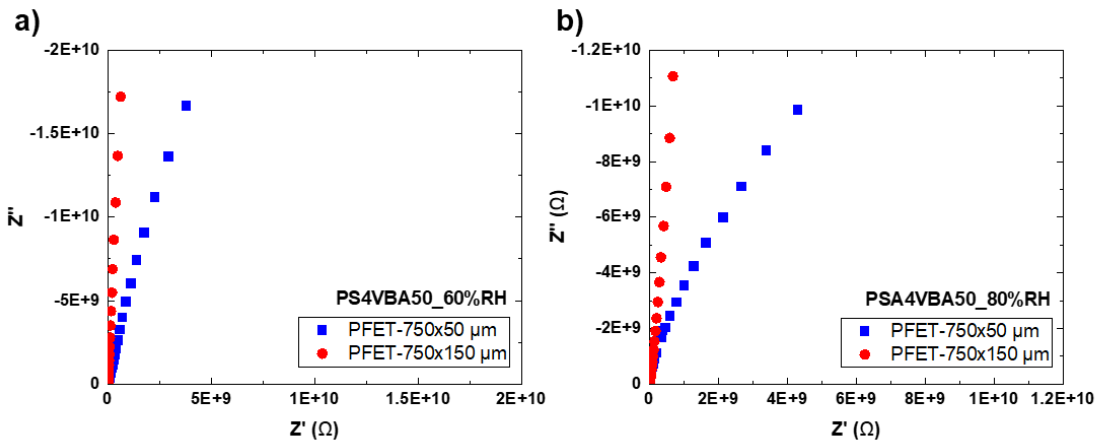

Figure 3.9 The Nyquist plots of PS4VBA50 thin film at a) 60%RH and b) 80%RH on the PFET with a fixed channel width of 750 µm but different channel length of 50 µm (blue ■) and 150 µm (red ●).

The impedance response between two Au electrodes without polymer thin film, S-D, was investigated and compared with the response of polymer thin film, as shown in Figure 3.10a. The S-D impedance response shows a similar vertical-line-like response to the response of polymer thin film. This information confirms that the resistance of polymer thin film is excessively high and comparable to the Au electrode/ air resistance. Moreover, the impedance response between electrode and gate, S-G, or the resistance of the insulating layer was observed, as shown in Figure 3.10b. The curve-line response was observed, referring to the partially short-circuit between S-G. This result confirms the high resistance of polymer thin film, which is comparable to or higher than the insulating layer's resistance. Therefore, the reduction of polymer thin film resistance on PFETs is necessary to investigate low conductivity polymer thin film.

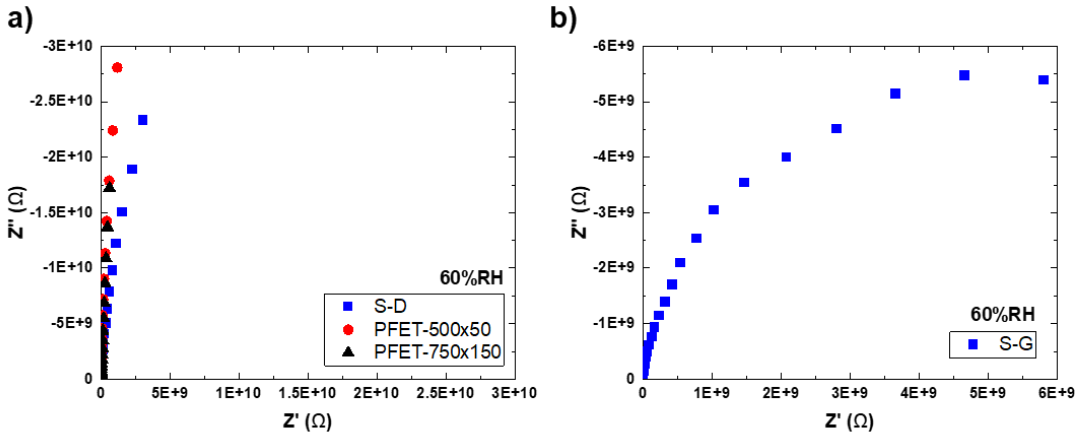

Figure 3.10 a) The Nyquist plots of PS4VBA50 thin film at 60%RH on the PFETs with 500 µm width and 50 µm length (500×50) and 750 µm width and 150 µm length (750×150) channel sizes comparing to the impedance of source (S) and drain (D). b) The impedance of S and gate (G) at 60%RH.

3.3.2.2 The effect of channel size on impedance response in PFETs and the proposed method for the performance improvement

The influence of PFET's channel size on the impedance response was investigated. The Nyquist plots of smaller channel size, 500×50, and larger channel size, 750×150, were compared in Figure 3.11a-d to evaluate the influence of channel size. Even though the channel size was different, a similar response was obtained. However, the response of PFET with 500×50 channel size tends to show a more RH dependence trend. The impedance response of 500×50 and 750×150 PFETs were compared with 750 µm width and 50 µm length (750×50) PFET to identify more in detail of the effect of channel size, as shown in Figure 3.11e. The response of polymer thin film on 750×50 PFET shows different impedance responses from polymer thin film responses on 500×50 and 750×150 PFETs. The response of polymer thin film on a wide channel width of 750 µm and a short channel length of 50 µm PFET might be less suppressed by the double layer capacitance response. If this assumption was correct, the impedance response of the polymer thin film might be able to improve by reducing channel length and increasing channel width.

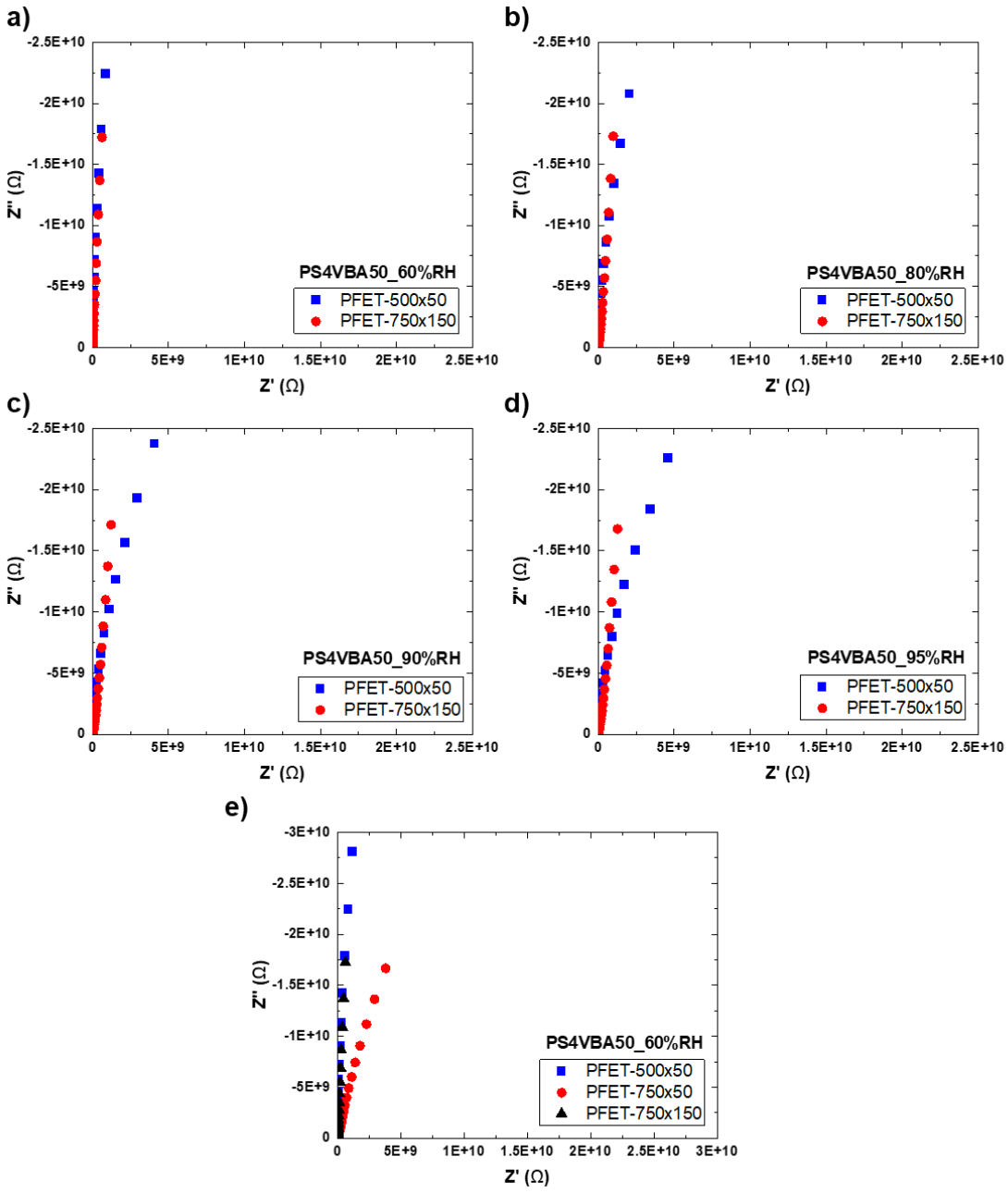

Figure 3.11 The comparison of the Nyquist plots of PS4VBA50 thin film between PFET with the channel size of 500 µm × 50 µm (500×50) and 750 µm × 150 µm (750×150) at a) 60%RH, b) 80%RH, c) 90%RH, and d) 95%RH. e) The Nyquist plots of PS4VBA50 thin film on 500×50, 750 µm × 50 µm (750×50), and 750×150 PFETs at 60%RH.

The channel's design needs to be adjusted to improve PFETs performance with low conductivity polymer thin film. According to the conductivity equation below (equation 1), the width (*W*) and length (*L*) of the channel or the channel size directly affect the resistance.

$$\sigma = {}^{L}/_{RWt}, \quad (1)$$

Where σ, *R*, and t represent the proton conductivity of polymer thin film, the resistance value collected from the impedance, and the film's thickness, respectively.

In order to improve the performance in electrical properties investigation, one possible method is to reduce the resistance of polymer thin film. Equation 1 can be rearranged as below.

$$R = {}^{L}/_{\sigma Wt}, \quad (2)$$

From equation 2, it was shown that the resistance increased with the increase of the channel length ($L \propto W$) but decreased with the increase of the channel width ($R \propto {}^{1}/_{W}$). Consistent with the above assumption, the device with a short channel length provided a better polymer thin film impedance response. Therefore, the design of FET with short channel length and wide channel width was expected to reduce the resistance of polymer thin film.

3.4 Conclusions

The devices for electrical properties investigation of polymer thin film with a parallel-shaped channel, PFETs, were successfully fabricated with different channel sizes. The electrical properties of the fabricated weak-acid functionalized styrene-based copolymer thin film, PS4VBA50, in PFETs were investigated using AC-impedance measurement to prevent the electrode reaction. The Nyquist plots of polymer thin film on the PFETs show the vertical-line response, indicating that Au electrodes/ polymer thin film interfacial double layer capacitance was involved and dominated. This dominant response might be caused by the relatively low proton conductivity of fabricated PS4VBA50 thin film. The PFET with a short channel length and wide channel width tends to provide a slightly better RH dependence impedance response. The method for RH dependence response improvement was discussed. The reduction of channel length and the extension of the channel or electrode width were expected to reduce the polymer thin film's resistance. After the device's channel structure modification, the semicircle-response, which represents the response of polymer thin film, might be obtained using the AC-impedance measurement and Au electrodes.

References

(1) Lozier, R. H.; Bogomolni, R. A.; Stoeckenius, W. Bacteriorhodopsin: A Light-Driven Proton Pump in Halobacterium Halobium. *Biophys. J.* **1975**, *15* (9), 955–962. https://doi.org/10.1016/S0006-3495(75)85875-9.

(2) Krimm, S.; Dwivedi, A. M. Infrared Spectrum of the Purple Membrane: Clue to a Proton Conduction Mechanism? *Science* **1982**, *216* (4544), 407–408. https://doi.org/10.1126/science.6280277.

(3) Morgan, H.; Martin Taylor, D.; Oliveira, O. N. Proton Transport at the Monolayer-Water Interface. *Biochim. Biophys. Acta - Biomembr.* **1991**, *1062* (2), 149–156. https://doi.org/10.1016/0005-2736(91)90386-M.

(4) Dér, A.; Száraz, S.; Tóth-Boconádi, R.; Tokaji, Z.; Keszthelyi, L.; Stoeckenius, W. Alternative Translocation of Protons and Halide Ions by Bacteriorhodopsin. *Proc. Natl. Acad. Sci. U. S. A.* **1991**, *88* (11), 4751–4755. https://doi.org/10.1073/pnas.88.11.4751.

(5) Tittor, J.; Schweiger, U.; Oesterhelt, D.; Bamberg, E. Inversion of Proton Translocation in Bacteriorhodopsin Mutants D85N, D85T, and D85,96N. *Biophys. J.* **1994**, *67* (4), 1682–1690. https://doi.org/10.1016/S0006-3495(94)80642-3.

(6) Nachliel, E.; Gutman, M.; Kiryati, S.; Dencher, N. A. Protonation Dynamics of the Extracellular and Cytoplasmic Surface of Bacteriorhodopsin in the Purple Membrane. *Proc. Natl. Acad. Sci. U. S. A.* **1996**, *93* (20), 10747–10752. https://doi.org/10.1073/pnas.93.20.10747.

(7) Váró, G.; Keszthelyi, L. Photoelectric Signals from Dried Oriented Purple Membranes of Halobacterium Halobium. *Biophys. J.* **1983**, *43* (1), 47–51.

https://doi.org/10.1016/S0006-3495(83)84322-7.

(8) Teissié, J.; Prats, M.; Soucaille, P.; Tocanne, J. F. Evidence for Conduction of Protons along the Interface between Water and a Polar Lipid Monolayer. *Proc. Natl. Acad. Sci.* **1985**, *82* (10), 3217 LP – 3221. https://doi.org/10.1073/pnas.82.10.3217.

(9) Sakurai, I.; Kawamura, Y. Lateral Electrical Conduction along a Phosphatidylcholine Monolayer. *Biochim. Biophys. Acta - Biomembr.* **1987**, *904* (2), 405–409. https://doi.org/10.1016/0005-2736(87)90391-9.

(10) Leberle, K.; Kempf, I.; Zundel, G. An Intramolecular Hydrogen Bond with Large Proton Polarizability within the Head Group of Phosphatidylserine. An Infrared Investigation. *Biophys. J.* **1989**, *55* (4), 637–648. https://doi.org/10.1016/S0006-3495(89)82861-9.

(11) Polle, A.; Junge, W. Proton Diffusion along the Membrane Surface of Thylakoids Is Not Enhanced over That in Bulk Water. *Biophys. J.* **1989**, *56* (1), 27–31. https://doi.org/10.1016/S0006-3495(89)82649-9.

(12) Butt, H. J.; Fendler, K.; Bamberg, E.; Tittor, J.; Oesterhelt, D. Aspartic Acids 96 and 85 Play a Central Role in the Function of Bacteriorhodopsin as a Proton Pump. *EMBO J.* **1989**, *8* (6), 1657–1663. https://doi.org/10.1002/j.1460-2075.1989.tb03556.x.

(13) Trissl, H. W. Photoelectric Measurements of Purple Membranes. *Photochem. Photobiol.* **1990**, *51* (6), 793–818. https://doi.org/10.1111/php.1990.51.6.793.

(14) Needleman, R.; Chang, M.; Ni, B.; Váró, G.; Fornés, J.; White, S. H.; Lanyi, J. K. Properties of Asp212—-Asn Bacteriorhodopsin Suggest That Asp212 and Asp85 Both Participate in a Counterion and Proton Acceptor Complex near the

Schiff Base. *J. Biol. Chem.* **1991**, *266* (18), 11478–11484. https://doi.org/10.1016/S0021-9258(18)98982-9.

(15) Strakosas, X.; Selberg, J.; Hemmatian, Z.; Rolandi, M. Taking Electrons out of Bioelectronics: From Bioprotonic Transistors to Ion Channels. *Adv. Sci.* **2017**, *4* (7), 1–7. https://doi.org/10.1002/advs.201600527.

(16) Hemmatian, Z.; Miyake, T.; Deng, Y.; Josberger, E. E.; Keene, S.; Kautz, R.; Zhong, C.; Jin, J.; Rolandi, M. Taking Electrons out of Bioelectronics: Bioprotonic Memories{,} Transistors{,} and Enzyme Logic. *J. Mater. Chem. C* **2015**, *3* (25), 6407–6412. https://doi.org/10.1039/C5TC00502G.

(17) Zhu, L. Q.; Wan, C. J.; Guo, L. Q.; Shi, Y.; Wan, Q. Artificial Synapse Network on Inorganic Proton Conductor for Neuromorphic Systems. *Nat. Commun.* **2014**, *5*, 3158. https://doi.org/10.1038/ncomms4158.

(18) Ordinario, D. D.; Phan, L.; Van Dyke, Y.; Nguyen, T.; Smith, A. G.; Nguyen, M.; Mofid, N. M.; Dao, M. K.; Gorodetsky, A. A. Photochemical Doping of Protonic Transistors from a Cephalopod Protein. *Chem. Mater.* **2016**, *28* (11), 3703–3710. https://doi.org/10.1021/acs.chemmater.6b00336.

(19) Lee, W.-K.; Pietron, J. J.; Kidwell, D. A.; Robinson, J. T.; McGann, C. L.; Sheehan, P. E.; Mulvaney, S. P. Enhanced Protonic Conductivity and IFET Behavior in Individual Proton-Doped Electrospun Chitosan Fibers. *J. Mater. Chem. C* **2019**, *7* (35), 10833–10840. https://doi.org/10.1039/C9TC02452B.

(20) Zhong, C.; Deng, Y.; Roudsari, A. F.; Kapetanovic, A.; Anantram, M. P.; Rolandi, M. A Polysaccharide Bioprotonic Field-Effect Transistor. *Nat. Commun.* **2011**, *2* (1), 2–6. https://doi.org/10.1038/ncomms1489.

(21) Zhong, H.; Wu, G.; Fu, Z.; Lv, H.; Xu, G.; Wang, R. Flexible Porous Organic

Polymer Membranes for Protonic Field-Effect Transistors. *Adv. Mater.* **2020**, *32* (21), 1–7. https://doi.org/10.1002/adma.202000730.

(22) Deng, Y.; Josberger, E.; Jin, J.; Rousdari, A. F.; Helms, B. A.; Zhong, C.; Anantram, M. P.; Rolandi, M. H + -Type and OH - -Type Biological Protonic Semiconductors and Complementary Devices. *Sci. Rep.* **2013**, *3*. https://doi.org/10.1038/srep02481.

(23) Ordinario, D. D.; Phan, L.; Walkup IV, W. G.; Jocson, J.-M.; Karshalev, E.; Hüsken, N.; Gorodetsky, A. A. Bulk Protonic Conductivity in a Cephalopod Structural Protein. *Nat. Chem.* **2014**, *6* (7), 596–602. https://doi.org/10.1038/nchem.1960.

(24) Wu, G. D.; Zhou, H. L.; Fu, Z. H.; Li, W. H.; Xiu, J. W.; Yao, M. S.; Li, Q. hong; Xu, G. MOF Nanosheet Reconstructed Two-Dimensional Bionic Nanochannel for Protonic Field-Effect Transistors. *Angew. Chemie - Int. Ed.* **2021**. https://doi.org/10.1002/anie.202100356.

(25) Paul, D. K.; McCreery, R.; Karan, K. Proton Transport Property in Supported Nafion Nanothin Films by Electrochemical Impedance Spectroscopy. *J. Electrochem. Soc.* **2014**, *161* (14), F1395–F1402. https://doi.org/10.1149/2.0571414jes.

(26) Huang, F.; Liu, A.; Zhu, H.; Xu, Y.; Balestra, F.; Ghibaudo, G.; Noh, Y. Y.; Chu, J.; Li, W. Reliable Mobility Evaluation of Organic Field-Effect Transistors with Different Contact Metals. *IEEE Electron Device Lett.* **2019**, *40* (4), 605–608. https://doi.org/10.1109/LED.2019.2901315.

(27) Ushiba, S.; Miyakawa, N.; Okino, T.; Shinagawa, A.; Oka, Y.; Kimura, M.; Ono, T.; Kanai, Y.; Inoue, K.; Matsumoto, K. Biosensing Platforms Based on

Graphene Field Effect Transistors. *Vac. Surf. Sci.* **2020**, *63*, 358–363. https://doi.org/10.1380/vss.63.358.

(28) Kwon, J.; Lee, Y.; Lee, T.; Ahn, J.-H. Aptamer-Based Field-Effect Transistor for Detection of Avian Influenza Virus in Chicken Serum. *Anal. Chem.* **2020**, *92* (7), 5524–5531. https://doi.org/10.1021/acs.analchem.0c00348.

(29) Kim, D.; Zhu, H.; Liu, A.; Kim, H. S.; Noh, Y. Y.; Hwang, D. H. Highly Ambient-Stable Organic Thin-Film Transistors Fabricated Using Naphthalene Diimide and Thienylene-Vinylene-Thienylene-Based n-Type Polymers with Different Electron-Withdrawing Groups. *J. Phys. Chem. C* **2020**, *124* (38), 20784–20793. https://doi.org/10.1021/acs.jpcc.0c06531.

(30) Kim, S.; Kwon, M. S.; Han, J. H.; Yuk, J.; Lee, J. Y.; Lee, K. T.; Kim, T. H. Poly(Ethylene-Co-Vinyl Acetate)/Polyimide/Poly(Ethylene-Co-Vinyl Acetate) Tri-Layer Porous Separator with High Conductivity and Tailored Thermal Shutdown Function for Application in Sodium-Ion Batteries. *J. Power Sources* **2021**, *482* (July 2020). https://doi.org/10.1016/j.jpowsour.2020.228907.

(31) Huang, H.; Nia, L.; Xu, S.; Luo, F.; Fan, J.; Li, H.; Wang, H. Novel Proton Exchange Membrane with Long-Range Acid–Base-Pair Proton Transfer Pathways Based on Functionalized Polyethyleneimine. *ACS Sustain. Chem. Eng.* **2021**, *9* (10), 3963–3974. https://doi.org/10.1021/acssuschemeng.1c00154.

(32) Wu, G. D.; Zhou, H. L.; Fu, Z. H.; Li, W. H.; Xiu, J. W.; Yao, M. S.; Li, Q. hong; Xu, G. MOF Nanosheet Reconstructed Two-Dimensional Bionic Nanochannel for Protonic Field-Effect Transistors. *Angew. Chemie - Int. Ed.* **2021**, 1–6. https://doi.org/10.1002/anie.202100356.

(33) Agam, Y.; Nandi, R.; Bulava, T.; Amdursky, N. The Role of the Protein–Water Interface in Dictating Proton Conduction across Protein-Based Biopolymers. *Mater. Adv.* **2021**, *2* (5), 1739–1746. https://doi.org/10.1039/d0ma00951b.

(34) Halim, J.; Büchi, F. N.; Haas, O.; Stamm, M.; Scherer, G. G. Characterization of Perfluorosulfonic Acid Membranes by Conductivity Measurements and Small-Angle x-Ray Scattering. *Electrochim. Acta* **1994**, *39* (8), 1303–1307. https://doi.org/10.1016/0013-4686(94)E0051-Z.

(35) Slade, S.; Campbell, S. A.; Ralph, T. R.; Walsh, F. C. Ionic Conductivity of an Extruded Nafion 1100 EW Series of Membranes. *J. Electrochem. Soc.* **2002**, *149* (12), A1556. https://doi.org/10.1149/1.1517281.

(36) Lee, C. H.; Park, H. B.; Lee, Y. M.; Lee, R. D. Importance of Proton Conductivity Measurement in Polymer Electrolyte Membrane for Fuel Cell Application. *Ind. Eng. Chem. Res.* **2005**, *44* (20), 7617–7626. https://doi.org/10.1021/ie0501172.

(37) Soboleva, T.; Xie, Z.; Shi, Z.; Tsang, E.; Navessin, T.; Holdcroft, S. Investigation of the Through-Plane Impedance Technique for Evaluation of Anisotropy of Proton Conducting Polymer Membranes. *J. Electroanal. Chem.* **2008**, *622* (2), 145–152. https://doi.org/10.1016/j.jelechem.2008.05.017.

(38) Yadav, R.; Fedkiw, P. S. Analysis of EIS Technique and Nafion 117 Conductivity as a Function of Temperature and Relative Humidity. *J. Electrochem. Soc.* **2012**, *159* (3), B340–B346. https://doi.org/10.1149/2.104203jes.

(39) Nadia E, T.; Roya, M.; Mohammad, S. Three-Dimensional Impedance-Based Sensors for Detection of Chemicals in Aqueous Solutions. *Int. J. Anal. Bioanal.*

Methods **2020**, *2* (1). https://doi.org/10.35840/ijabm/2412.

Chapter 4

The development of comb-shaped field-effect transistors electrodes for low conductivity polymer thin films investigation

Abstract

The investigation of proton transport in biopolymers or bioinspired materials is essential since these materials can be applied in many applications and leads to more understanding of the mechanism in biological systems. However, due to the low proton conductivity of these biomaterials, the investigation of electrical properties without using the influence of extra proton from the Pd electrode is challenging. The devices with highly extended channel width and short channel length comb-shaped gold electrodes (CFETs) were fabricated to reduce the resistance of polymer thin films. The low proton conductivity polymer thin film was applied to the designed CFETs, and its electrical properties were successfully investigated using the AC-impedance measurement. The polymer thin film's impedance response obtained from CFETs was clearly shown without the dominated by the double layer capacitance response. The semicircle and relative humidity (RH) dependence responses were also observed, confirming the response of polymer thin film's proton conduction, and the electrical properties of low conductive polymer thin film can be estimated. The influence of channel length shows that CFETs with shorter channel lengths are better in the polymer thin film's resistance reduction. Moreover, the effect of the substrate surface on the films' electrical properties was discovered. The type of substrate surface strongly influences the main proton transportation at the film/ substrate surface interface region. This study overcomes the drawbacks of dominating double layer capacitance response and the short circuit between two electrodes through the thin dielectric layer in the AC-impedance measurement method.

4.1 Introduction

Even though these bioinspired materials provide relatively low proton conductivity compared to the proton conductivity of commercial Nafion™, the study of proton transport properties in biopolymers is still gaining much attention from many researchers to its efficient proton transfer along the amino acid pathway.[1–3] The study of proton transport in biomaterials also leads to more understanding of proton translocation in biological systems. For example, Zhong and co-workers studied the proton transport in maleic-chitosan nanofibers.[4] The proton conductivity of pyridine chitosan, a biomaterial, has been investigated.[5] The electrical properties of cephalopod biopolymers also have been examined recently.[6–10] Amdursky and co-workers examined the proton conduction across the bovine serum albumin mat.[11] Table 4.1 summarized proton conductivity of the reported biomaterials in a range of 1×10^{-5}-0.7 mS cm^{-1}. Therefore, due to the low conductivity of these biomaterials, many studies used the palladium (Pd) electrodes for electrical properties investigation since Pd electrodes can provide extra protons when reacting with H_2 using a direct current (DC) measurement.[6,12–14] To prevent the influence of electrode reaction that can affect the electrical properties of proton conductive materials, developing the device for biopolymer's electrical properties measurement without using Pd electrode is challenging.

Table 4.1 The summarized proton conductivity of Nafion™ and reported biomaterials.

Materials	Proton conductivity (mS cm^{-1})
Nafion™[15]	78
Keratin Sulfate[3]	0.5
Maleic-chitosan nanofibers[4]	0.7
Pyridine chitosan[5]	1×10^{-5}
Melanin[8]	0.02
Reflectin[9]	0.1
Bovine Serum Albumin[11]	0.05

From the previous chapter, Chapter 3, the parallel-shaped FETs (PFETs) were successfully fabricated for the alternative current (AC)-impedance measurement using gold (Au) electrodes. The effect of electrode reaction can be prevented using an AC-measurement system, and the information of each component, depending on the frequency, can be investigated. However, the electrical properties of polymer thin film cannot be identified due to its high resistance and low conductivity. The response of double layer capacitance dominated the response of polymer thin film. The proposed solution to improve this situation is to reduce the channel length and extend the channel width.

Previously, many studies of charge transport in a small device as FETs were published. For example, maleic chitosan proton transport properties were investigated in FET devices with channel width and length of 3.5µm and 8.6 µm, respectively.[4] Mondal and co-workers studied the proton transport of protein biopolymer using devices with only 70-100 µm channel length.[16,17] The proton conductivity of thiourea-based polymer membranes was examined in the transistor device with a narrow channel length of 100 µm and wide channel width of 5 cm.[6] The channel size of FET for investigation of cephalopod protein's proton transport properties also relatively small with 50 µm long and 400 µm width.[18] The FETs for organic semiconductor thin films were also reported with a broad channel width of 1000-2000 µm and a short channel length of 10-20 µm.[19–21] This trend of channel size suggests that a relatively wide and short channel might be preferable for the electrical properties' investigation of conductive materials with low proton conductivity and high resistance. Even though our previous PFETs were comparable to the size of these devices, 50-150 µm long and 500-750 µm wide. It is important to note that we use a gold electrode and AC-impedance system for our measurement, which no extra proton involved. Therefore, increasing channel width and decreasing channel length of FETs were expected to improve polymer thin film impedance response.

A shorter and broader channel is required to change the PFET pattern. In this chapter, the devices with comb-shaped electrodes or CFETs were designed and fabricated. The channel width can be dramatically increased using comb-shaped electrodes. At the same time, the channel length was designed to be narrower in order to decrease the polymer thin film

resistance. Moreover, the relatively low proton conductivity carboxylic acid functionalized styrene-based copolymer from the Chapter 2 was applied to the CFETs to examine electrical properties using a gold electrode and AC-impedance measurement.

4.2 Materials and methods

4.2.1 Materials

Silicon wafer (Si-wafer) with 100 nm thick thermal oxide insulating layer and <100> crystal direction was purchased from Seiren KST Corp., Japan. 1,1,1,3,3,3-Hexamethyldisilazane (HMDS) was purchased from Tokyo Chemical Industry Co. Ltd., Japan. Positive photoresist TSMR-8900 and tetramethylammonium hydroxide (NMD-W, 2.38% w/w) were purchased from Tokyo Ohka Kogyo Co., Ltd. Microposit^{TM} remover 1165 was purchased from Dow Chemical Company. Acetone (99.8%, EL grade) was purchased from Kanto Chemical Co., Inc. All the chemicals were used as received. The fabricated proton conductive polymers functionalized with a carboxylic acid group from Chapter 2, P4VBA100 and PS4VBA33, were selected for study in this chapter.

4.2.2 Comb-shaped FETs pattern design

The FET with the comb-shaped electrode, as shown in Figure 4.1a, was designed to increase the channel width or electrode length of FETs. The CFET patterns with different channel lengths were drawn by Autodesk AutoCAD 2021. The total channel width was fixed at around 22 cm. The channel length was varied from 5, 10, and 15 μm to investigate the influence of channel length on the resistance of polymer thin film. As shown in Figure 4.1b-d, the CFETs were designed on the substrate size of 1.5 cm × 1.5 cm, and the electrodes contact area was designed as same as in the previous design of PFETs.

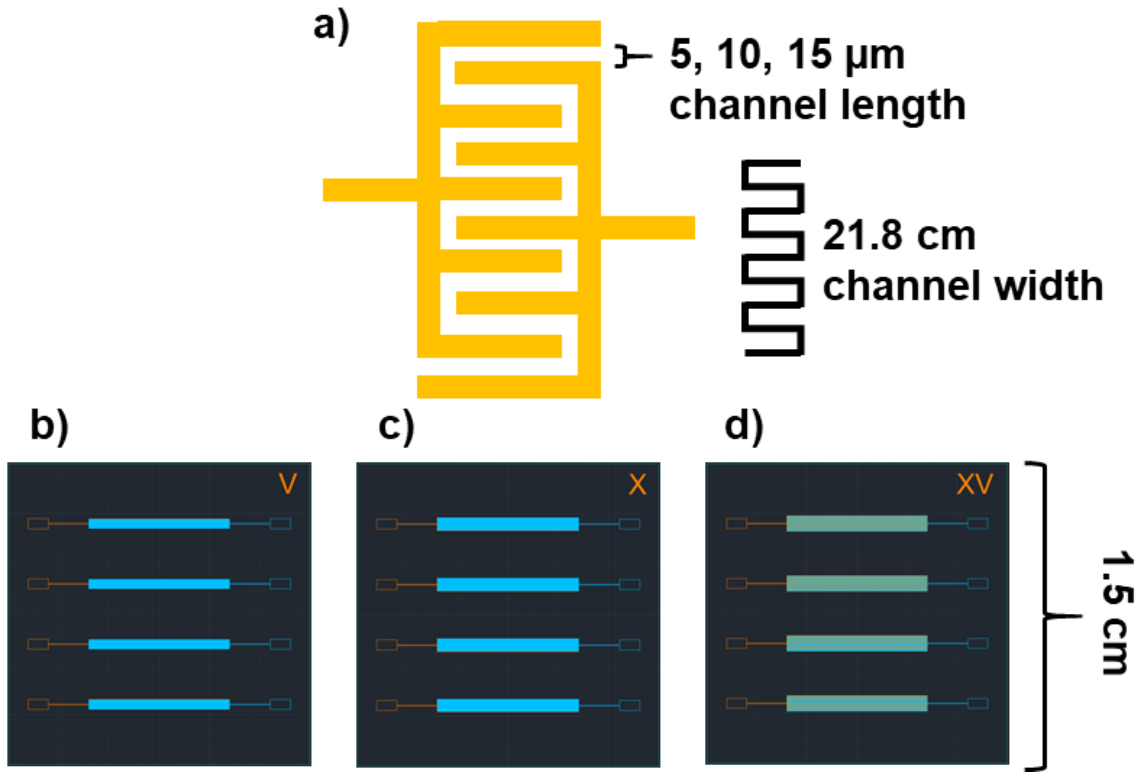

Figure 4.1 a) The schematic shows the design of CFET's channel shape. And the pattern design of CFETs with the channel length of b) 5 µm, c) 10 µm, and d) 15 µm.

4.2.3 Preparation of CFETs

The preparation of CFETs was similar to the preparation of PFETs in the previous chapter. Start from the surface cleaning of Si-wafer substrate by plasma treatment. HMDS was spin-coated on the Si-wafer surface for better adhesion of the photoresist layer, baked at 110°C for 5 min. After cooled down, the photoresist TSMR-8900 was spin-coated as a top layer then baked at 110°C for another 1.5 min. The photolithography was done using the same radiation wavelength of 504 nm on the designed electrode pattern area (Mark Less Aligner, Heidelberg Instruments MLA150). The exposure parts were washed away with NMD-W 2.38% w/w solution and rinsed with water for a minute before being dried with a nitrogen blower. The devices' surface was cleaned by plasma treatment before the metal sputtering. Titanium (Ti) was sputtered as a first layer by radio frequency (RF) sputtering technique, followed by a gold (Au) layer. The photoresist layer was removed by MICROPOSIT^{TM} remover 1165, then

sonicated in acetone, rinsed with water, and dried. Each set of devices on the Si-wafer was separated in the size of 2 cm × 2 cm.

4.2.4 Preparation of polymer thin film on CFETs

The surface of CFET was cleaned by solvent and plasma treatment before use. Then the thin film of styrene-based polymer functionalized with a carboxylic acid group was prepared on CFETs using the same procedure as in Chapter 2. The polymer thin films were prepared with various thicknesses by spin-coating technique. The excess film outside the channel was removed using methanol as a solvent, as shown in Figure 4.2.

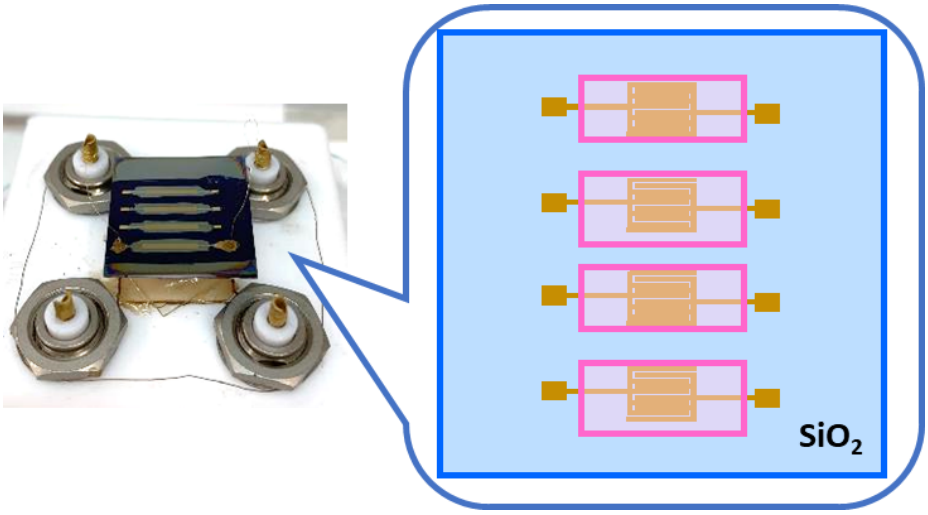

Figure 4.2 The schematic diagram represents the thin film prepared on the CFETs. The pink, gold, and blue areas represent proton conductive polymer thin film, electrodes, and SiO_2 layer of wafer substrate, respectively.

4.2.5 Proton conductivity measurements

As same as in the electrical properties investigation of PFETs from the previous chapter, the proton conductivity of polymer thin film on CFET was investigated in the RH-controlled and temperature-controlled chamber (SH-221; Espec Corp.) using an AC-impedance spectroscopy measurement system obtained with a frequency response analyzer equipped with a high-frequency dielectric interface (SI1260 and SI1293; Solartron Analytical). The CFET's Au electrodes were connected with Au wire and substrate holder using a porous gold

paste, as shown in Figure 4.3. The proton conductivity (σ) of polymer thin film was calculated using the following equation.

$$\sigma = {}^{L}/_{RWt}, \quad (1)$$

L and W respectively denote the channel length or the distance between the electrodes and channel width or the length of the electrode. R, and t represent the resistance value collected from the impedance and the film's thickness, respectively.

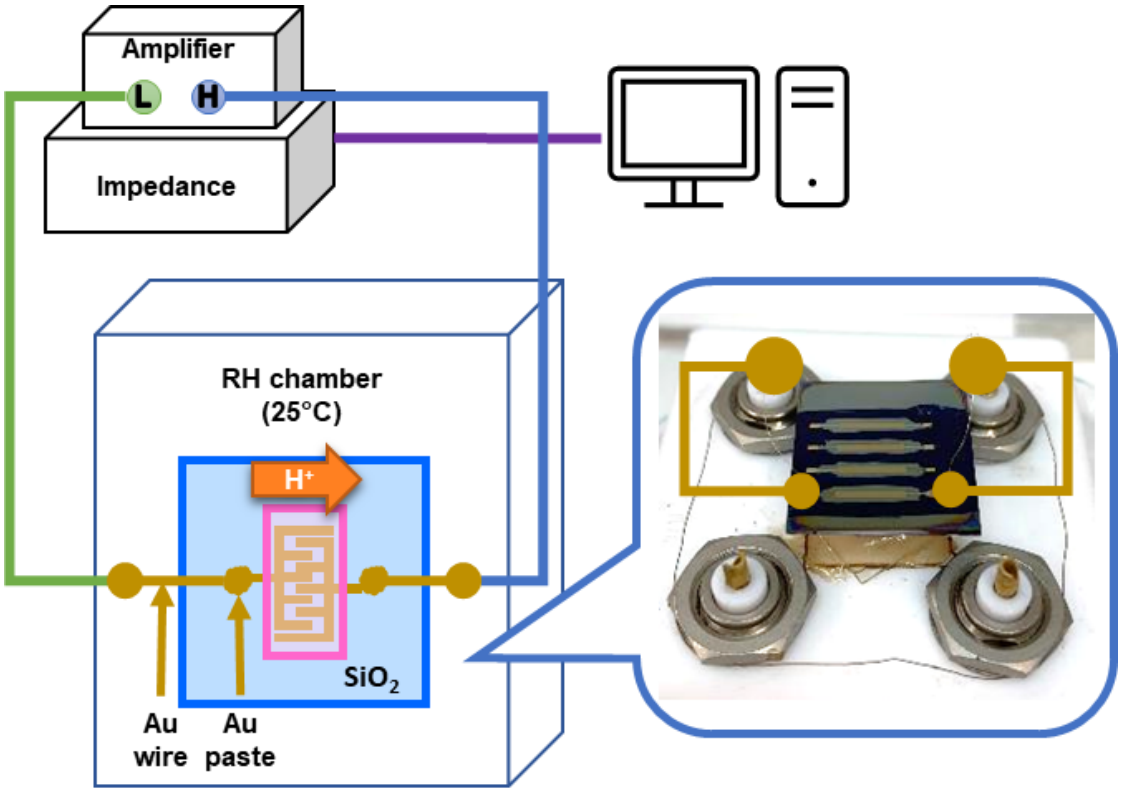

Figure 4.3 The schematic displays the impedance measurement setup for the polymer thin film's electrical properties investigation on CFETs.

The normalized resistance (*R*') was calculated using the following equation to investigate the interfacial proton conduction.[22]

$$R' = {}^{RW}/_{L}, \quad (2)$$

4.3 Results and discussion

4.3.1 The preparation of CFETs

The CFETs with extremely wide channel width and narrow channel length were successfully prepared. As shown in Figure 4.4a, four CFETs with the same channel length were deposited together on one substrate. The comb-shaped electrodes were checked using an optical microscope to confirm that there was no connected part of two electrodes which caused a short circuit. Figure 4.4b-d show that the comb-shaped electrodes were successfully deposited without any connection between electrodes in all devices. The thickness of deposited metal electrodes was observed using a step profiler. The thickness profile in Figure 4.5 shows the uniform thickness metal electrode of around 100 nm. The above data confirms the readiness of fabricated CFETs for the polymer thin film's electrical properties investigation.

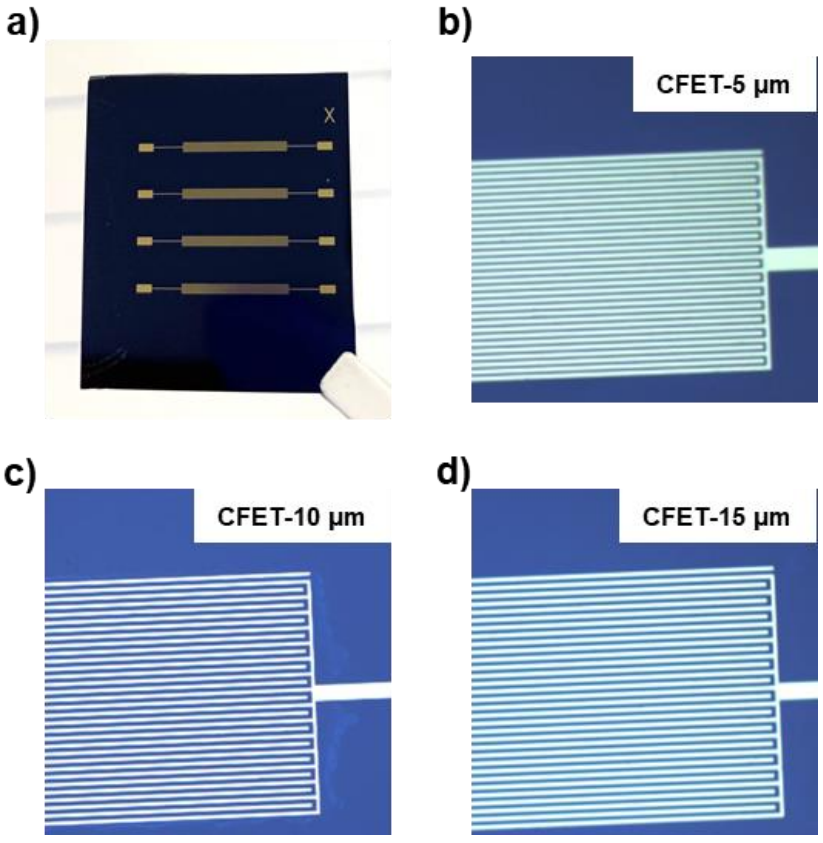

Figure 4.4 a) The image of prepared CFET with 10 µm channel length. And the optical microscopic images of b) 5 µm, c) 10 µm, and d) 15 µm channel length CFETs.

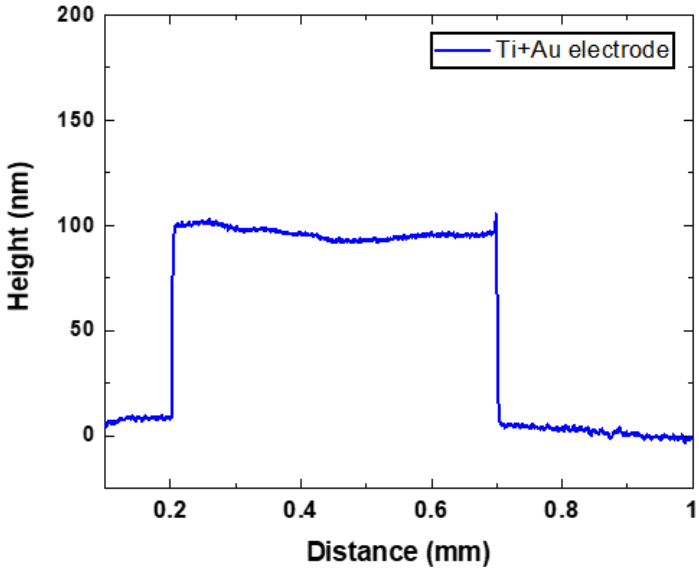

Figure 4.5. The thickness of metal deposited electrode on CFET measured by step profiler.

4.3.2 Electrical properties of weak-acid functionalized styrene-based copolymer thin films in CFETs

4.3.2.1 The impedance response in CFETs

The electrical properties of styrene-based copolymer functionalized with the carboxylic acid group thin film, P4VBA100, was successfully examined on the new CFETs using the AC-impedance measurement. The proton conductivity of polymer thin film was observed with a fixed temperature of 25°C and under various RH from 60-95%. Figure 4.6a and b show the impedance response of the polymer thin film on CFET with 15 µm channel length at various RH. The semicircle response, which derives from the film resistance and capacitance, and the vertical-line response or a tail part representing the capacitive behavior at the low-frequency region were presented at all RH.[23,24] The impedance response with two parts of a semicircle and a tail part was found in conductive materials.[16,17,23–28] Usually, the electrical properties of a low proton conductivity polymer thin film need to be observed at the low-frequency region, which might be dominated by the response from the double layer capacitance between polymer thin film and Au electrode interface.[23,24] However, in this measurement, the semicircle and tail responses were separated. The separation between the two responses indicates that

the semicircle response of the polymer thin film did not dominate by the double layer capacitance response and was derived only from the polymer thin film.

Moreover, the dielectric layer's resistance (R_{eSi}) also decreased when the electrode length increased because of the high contact area between the metal electrode and substrate. Figure 4.7 presents the possible equivalent circuit model of CFET with R_{eSi}.[24,29] It is essential to consider the RH dependence of the impedance response since the response from the dielectric layer does not change with RH while the conductive materials do.[23,24,30–32] As shown in Figure 4.6, the semicircle response shows the RH dependence, in which the resistance decreased with the increasing of RH. The end of the semicircle response, or the joint between the semicircle and tail response, moved to the lower resistance region when the RH increased. This RH dependence trend was consistent with the results when the proton conductivity of polymer thin film was observed on a quartz substrate (Chapter 2). Furthermore, this RH dependence of the obtained impedance response confirms that the semicircle response was obtained from proton conduction in the polymer thin film. The CFETs with 5 and 10 µm channel lengths also show both semicircle and tail part in their impedance response, and a similar trend of RH dependent was also observed.

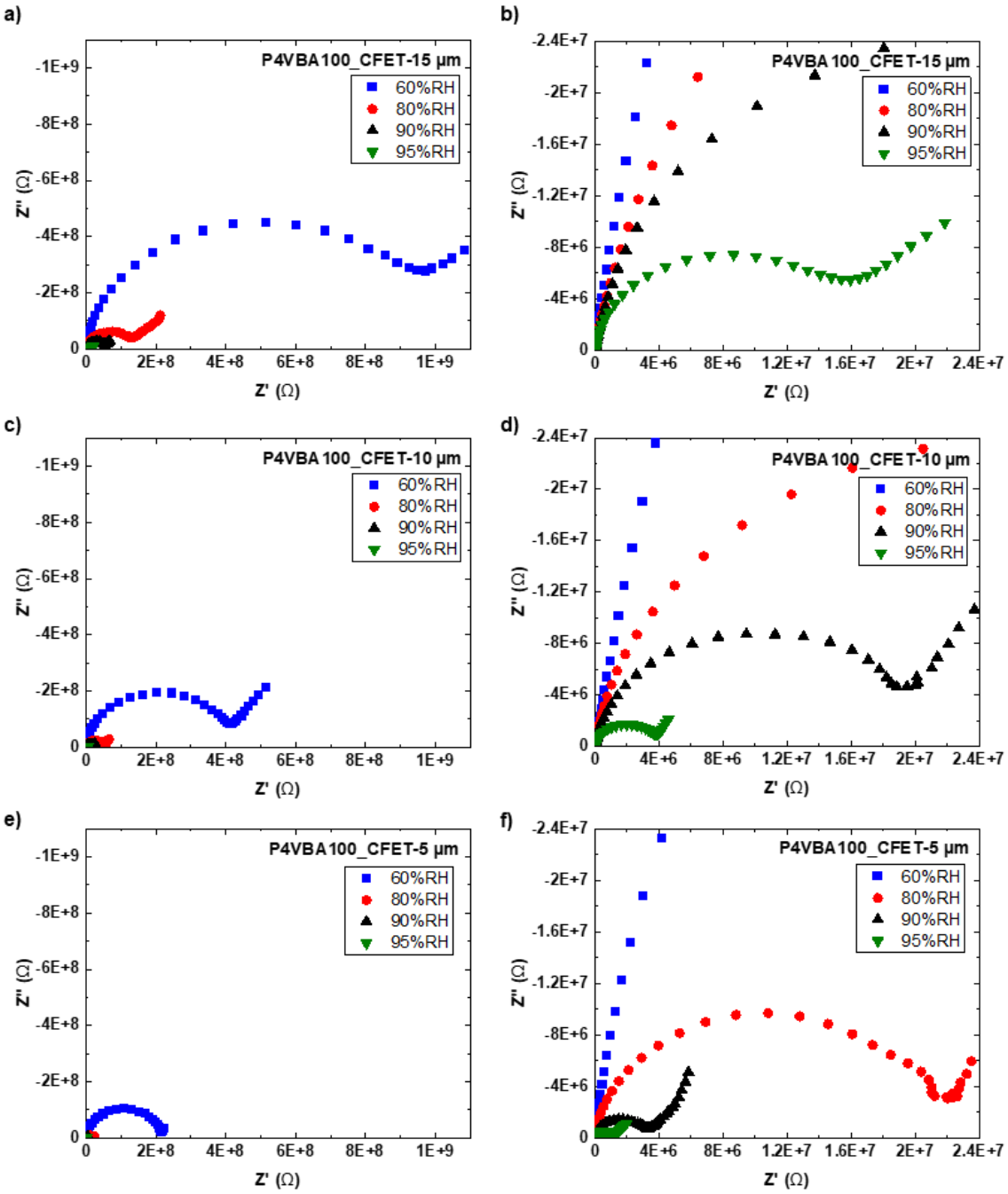

Figure 4.6 The Nyquist plots of P4VBA100 thin film at various RH on the CFETs with the channel length of a) and b) 15 µm, c) and d) 10 µm, and e) and f) 5 µm. b), d), and f) are zoom-in of the low resistance region.

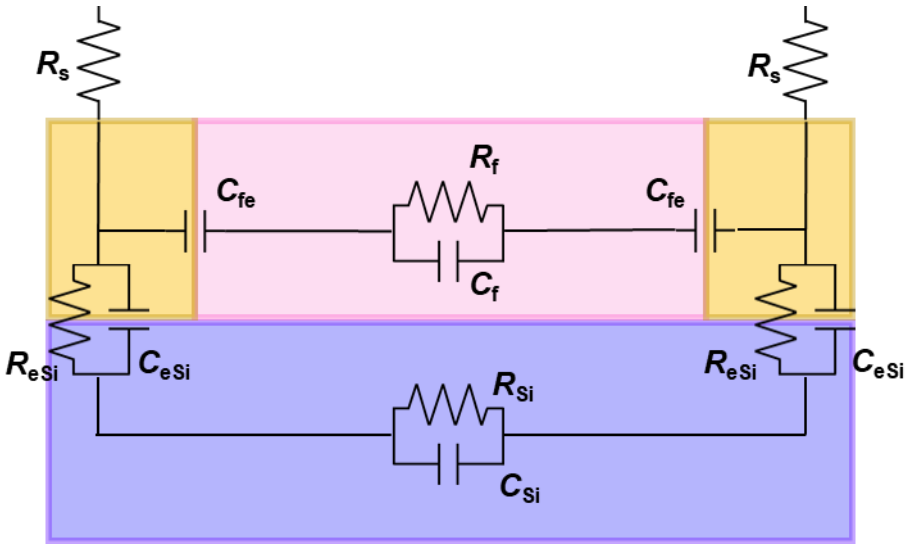

Figure 4.7 The schematic represents the possible impedance and capacitance components in the polymer thin film on silicon wafer (Si-wafer) substrate with gold electrodes. Yellow, pink, and purple areas represent the gold electrodes, proton conductive polymer thin film, and SiO_2 layer of Si-wafer substrate, respectively. *R* and *C* denote resistance and capacitance, respectively. R_s represent a serial resistance originated from the electrode contact. The subscripted f and Si represent the *R*/ *C* of the film and SiO_2 layer, respectively. The *C* of the interfacial region between the polymer film/ Au electrode was written as C_{fe}. R_{eSi} and C_{eSi} denote the *R* and *C* of Au electrode/ Si-wafer substrate interface. Only C_{fe} and C_{Si} were shown here since the R_{fe} and R_{Si} could be negligible, as explained in the previous chapter.

The impedance of the electrode and gate electrode (S-G) was examined to confirm the resistance of the dielectric layer. The gate electrode was prepared by etched the SiO_2 layer then connected the Au wire with Au paste. Figure 4.8 shows the impedance response between electrode and gate electrode. The impedance response almost did not change with RH, and no semicircle response was observed at both RH. This S-G impedance affirms that the impedance responses in Figure 4.6 were obtained from the polymer thin film.

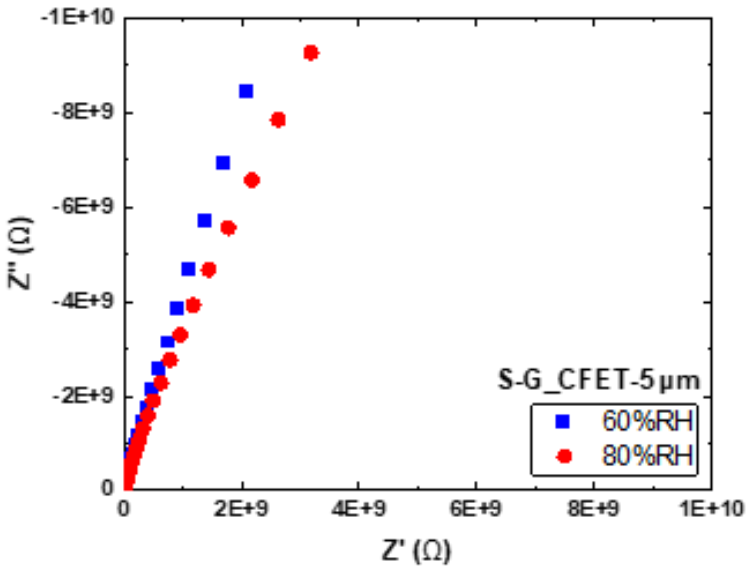

Figure 4.8 The Nyquist plot of the source and gate electrodes (S-G) at 60%RH (blue ■) and 80%RH (red ●).

The impedance response between two Au electrodes, without polymer thin film, of 15 µm channel length CFET was examined and compared with the response of polymer thin film on the CFETs with the same channel length. As shown in Figure 4.9, the different response shape between S-D and polymer thin film response was observed at all RH. The S-D impedance did not show a semicircle response, which can be observed in polymer thin film's impedance. This information also affirms that the response of polymer thin film was collected. From the above information, it can be concluded that the CFETs with the long channel can be used for the electrical properties' investigation of low proton conductivity polymer thin film using the AC-impedance with Au electrode measurement. Moreover, the resistance measurement between two electrodes is a piece of evidence that these CFETs overcome the drawback of the short circuit through the thin dielectric layer (SiO_2 100 nm) in the AC method.

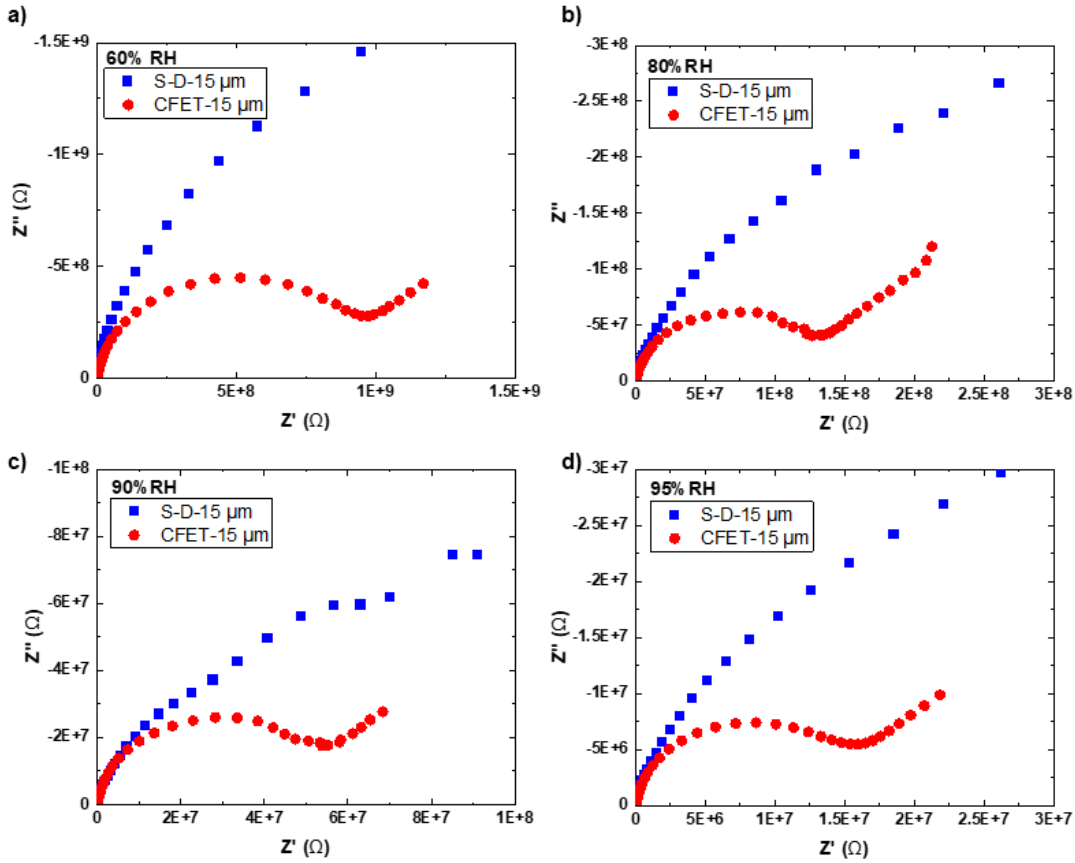

Figure 4.9 The Nyquist plot of P4VBA100 thin film compared with the plot of source-drain (S-D) electrodes at various RH of a) 60%RH, b) 80%RH, c) 90%RH, and d) 95%RH.

The impedance response of PS4VBA33 thin films was also examined using CFETs with different channel lengths under various RH. Figure 4.10 shows the semicircle and RH-dependent responses, confirming the response of polymer thin film. Similar to polymer thin film with internal proton conduction, the electrical properties of polymer thin film with interfacial proton conduction can also be observed and estimated using CFETs with Au-electrodes and an AC impedance system.

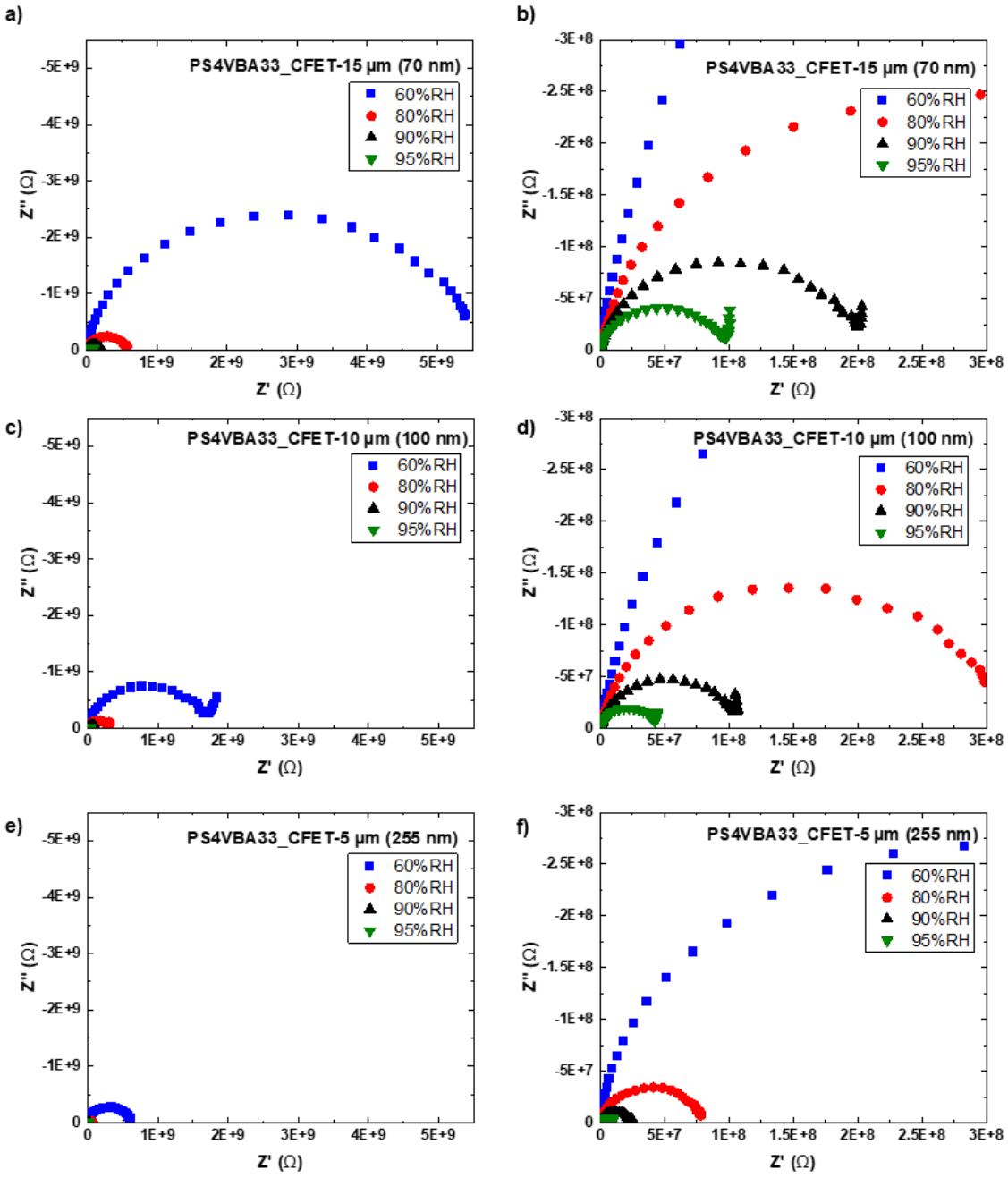

Figure 4.10 The Nyquist plots of PS4VBA33 thin film at various RH on the CFETs with the channel length of a) and b) 15 µm, c) and d) 10 µm, and e) and f) 5 µm. b), d), and f) are zoom-in of the low resistance region.

4.3.2.2 The influence of channel length on the decreasing of resistance in CFETs

The influence of channel length on the resistance of polymer thin film was examined. Since the channel length of CFET was expected to reduce the resistance of polymer thin film, the impedance of polymer thin film on different channel length CFETs was compared. As shown in Figure 4.11, 12, and Table 4.2, both internal and interfacial portion conductive thin films show the decreasing resistance of polymer thin film when the channel length decreased. The CFET with 5 µm channel length provides the lowest polymer thin film's resistance in all RH range. On the other hand, the highest polymer thin film's resistance was observed in the film on 15 µm length CFET. Consistent with the assumption that the short channel would lower the polymer thin film's resistance.

Therefore, the decreasing distance between electrodes or the reducing channel length is one of the promising ways to lower the resistance of polymer thin film with low proton conductivity and high resistance, preventing the dominant of double-layer capacitance between polymer thin film and Au electrode interface when measuring at low-frequency region.[24]

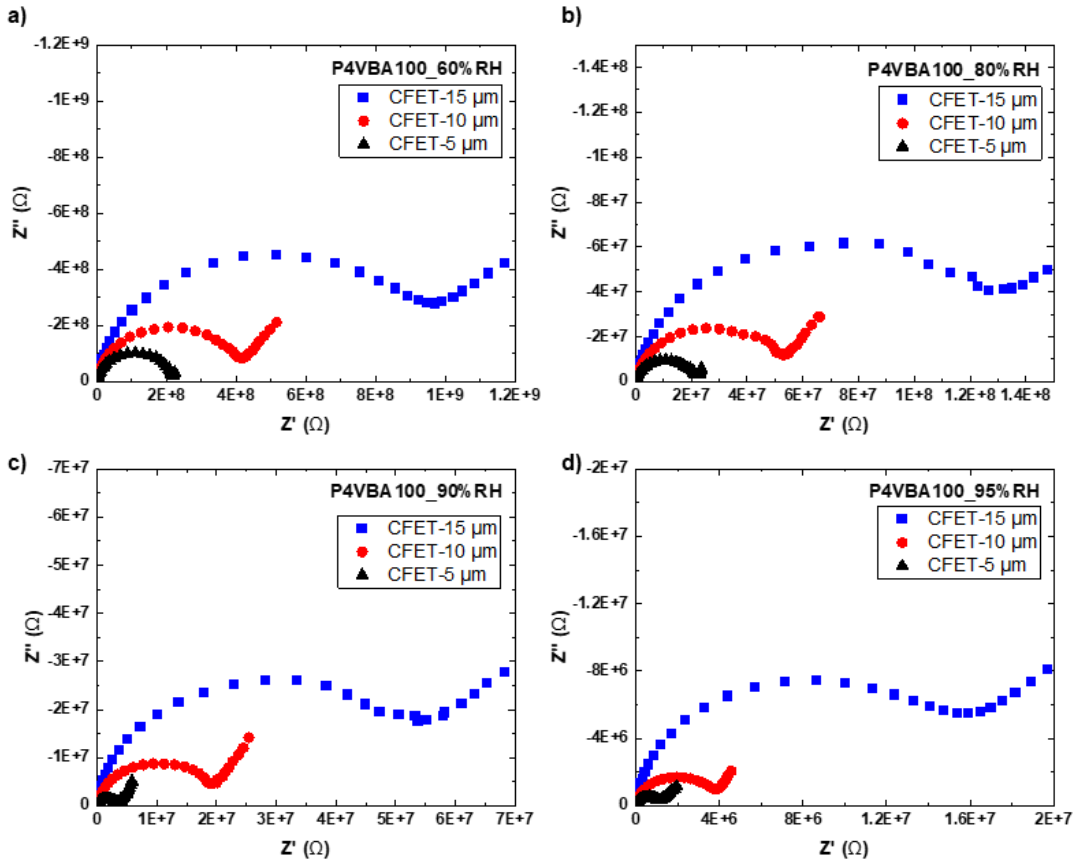

Figure 4.11 The Nyquist plot of P4VBA100 thin film compared between 15, 10, and 5 µm channel length at a) 60%RH, b) 80%RH, c) 90%RH, and d) 95%RH.

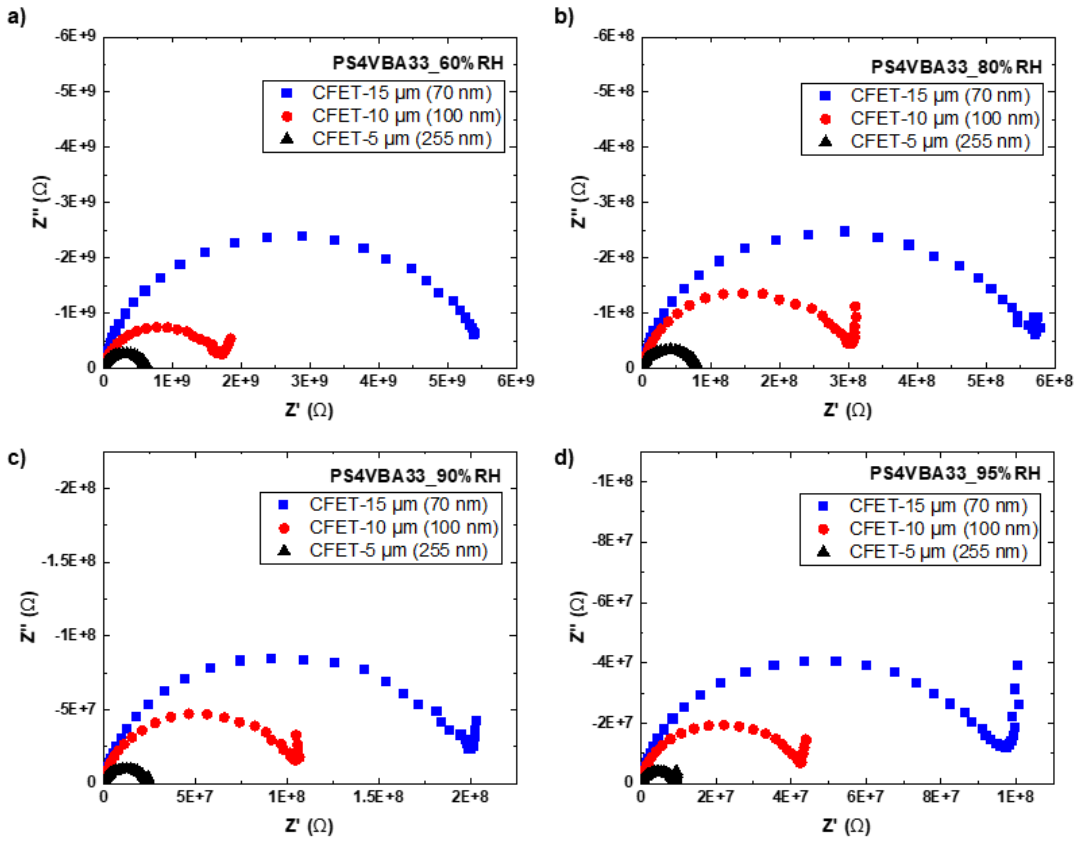

Figure 4.12 The Nyquist plot of PS4VBA33 thin film compared between 15, 10, and 5 µm channel length at a) 60%RH, b) 80%RH, c) 90%RH, and d) 95%RH.

Table 4.2 Resistance of polymer thin film on different CFETs with channel length at various RH.

Polymers	Device		CFETs		
	Channel length (μm)		5	10	15
P4VBA100	Resistance (*R*/ Ω)	%RH 60	2.2×10^{8}	4.1×10^{8}	9.5×10^{8}
		%RH 80	2.1×10^{7}	5.3×10^{7}	1.3×10^{8}
		%RH 90	3.1×10^{6}	1.9×10^{7}	4.7×10^{7}
		%RH 95	1.1×10^{6}	3.8×10^{6}	1.7×10^{7}
PS4VBA33	Resistance (*R*/ Ω)	%RH 60	6.1×10^{8}	1.7×10^{9}	5.5×10^{9}
		%RH 80	7.8×10^{7}	3.0×10^{8}	5.7×10^{8}
		%RH 90	2.3×10^{7}	1.1×10^{8}	2.0×10^{8}
		%RH 95	9.1×10^{6}	4.2×10^{7}	9.7×10^{7}

4.3.2.3 The electrical properties of polymer thin film on CFETs

The proton conductivity of P4VBA100 polymer thin film on both CFET and quartz substrate was estimated and compared. Figure 4.13a shows the proton conductivity comparison of the polymer thin film on quartz substrate and CFETs. Typically, P4VBA100 polymer thin film proton conductivity, which provides internal proton conduction, should show a film thickness independent. Therefore, polymer thin film proton conductivity on both quartz substrate and CFETs should be similar regardless of film thickness. However, Figure 4.13a displays the slightly lower conductivity of polymer thin film on CFETs than the polymer thin film on quartz substrate at high RH, while it was comparable at 60%RH. This difference in the conductivity at high RH might be due to the different water adsorption behavior in the polymer thin films on the different substrate surfaces of quartz substrate and CFETs. The more hydrophobicity of the thermal oxide layer on CFETs might cause a poor water adsorption ability at the polymer thin film/ substrate interface, resulting in lower proton conductivity of the polymer thin film on CFETs than that on the quartz substrate.

PS4VBA33 polymer thin film with interfacial proton conduction shows a significant difference in conductivity compared to the film's conductivity on a quartz substrate, as shown in Figure 4.13b. Interestingly, the films of 85 and 255 nm thickness on 5 µm CFETs also show a trend of film thickness independent of proton conductivity, referring to the internal proton conduction even though PS4VBA33 should provide a film thickness dependent of proton conductivity referring to the interfacial proton conduction.[22] This information might suggest that, in this case, the internal proton conduction dominates the interfacial proton conduction due to the change of substrate surface.

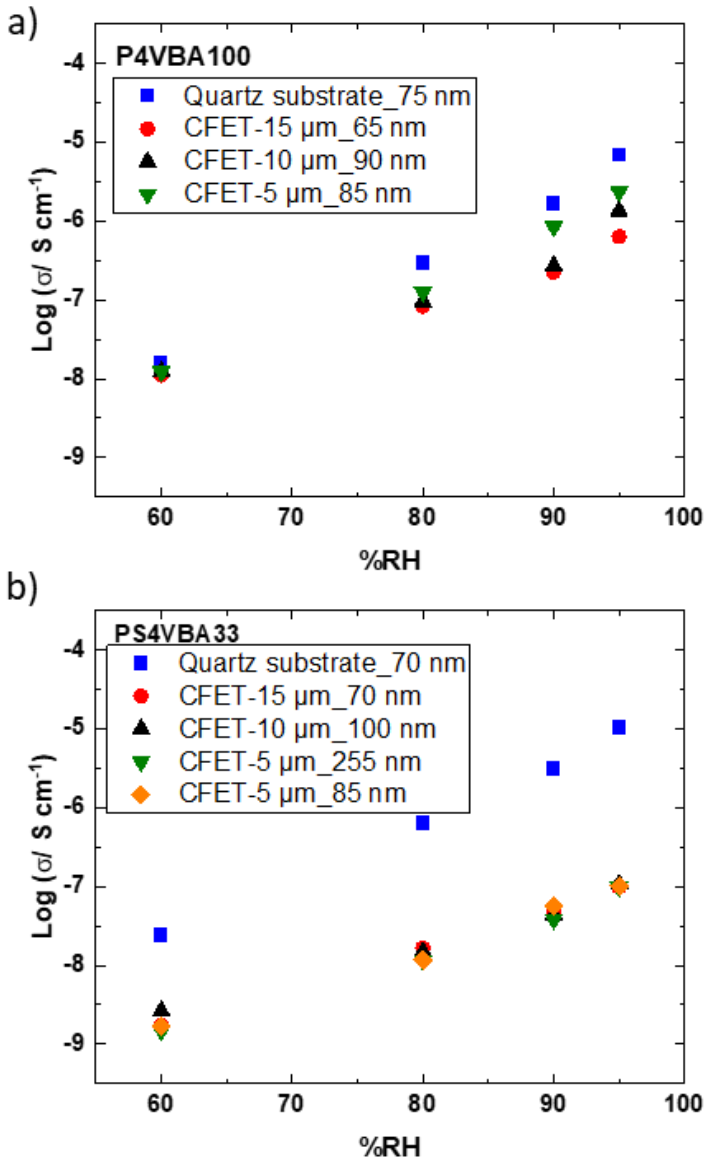

Figure 4.13 The proton conductivity of a) P4VBA100 and b) PS4VBA33 thin films on quartz substrate obtained from Chapter 2 (blue ■), CFET with 15 µm channel length (red ●), CFET with 10 µm channel length (black ▲), and CFET with 5 µm channel length (green ▼).

Furthermore, the normalized resistance, *R*', of polymer thin films on CFETs was also considered and compared with the films on the quartz substrate. Figure 4.14 and Table 4.3 show that *R*' of both P4VBA100 and PS4VBA33 thin films on all CFETs are higher than the *R*' of the film on the quartz substrate, especially at high RH. The difference of *R*' between P4VBA100 thin film on quartz and CFETs, as shown in Figure 4.14a, supports the different

water adsorption behavior of the thin film on quartz substrate and on CFETs. The difference in substrate surface hydrophilicity might be one of the factors for the different water adsorption.

From Figure 4.14b, *R*' of PS4VBA33 thin films also show the difference of *R*' between quartz and CFETs, referring to the effect of the substrate surface on the *R*' values. Also, the film thickness dependent of *R*' confirms the internal proton conduction of PS4VBA33 thin film on CFETs. The change of proton transport pathway from an interfacial to internal conduction supports the substrate surface effect on thin films' electrical properties. The poor water adsorption ability at the film/ CFET substrate surface interface was unsuitable for interfacial proton conduction, so the transport pathway shifted from interfacial to internal conduction. The lower proton conductivity than the film on quartz substrate might be caused by the low density of the free carboxylic acid group at the film's internal region. Moreover, the shift of the proton transport pathway when changing the substrate surface might indicate that the proton transport at the film/ substrate surface interface region is dominating rather than the proton transport at the air/ film interface. The above result attributes a strong effect of the substrate surface on the polymer thin film's electrical properties. Especially for the film with interfacial proton conduction as PS4VBA33, the substrate surface effect was more significant since the interfacial region is the main proton transport pathway.

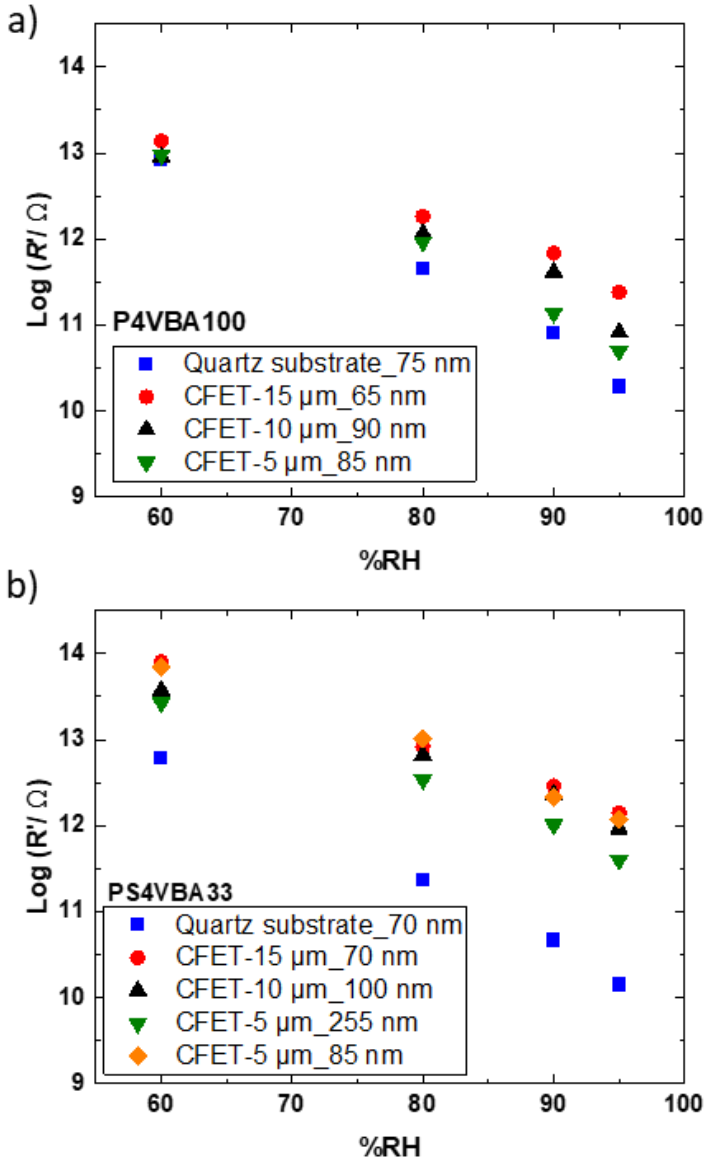

Figure 4.14 The normalized resistance of a) P4VBA100 and b) PS4VBA33 thin films on quartz substrate obtained from Chapter 2 (blue ■), CFET with 15 µm channel length (red ●), CFET with 10 µm channel length (black ▲), and CFET with 5 µm channel length (green ▼).

Table 4.3 Resistance, proton conductivity, and normalized resistance of polymer thin film on different channel lengths CFETs compared with polymer thin film on the quartz substrate. Two different PS4VBA33 film thicknesses of 85 and 255 nm on 5 µm CFET were investigated.

Polymers	Device		Quartz	CFETs			
	Channel length		5 mm	5 µm (85* and 255** nm)		10 µm	15 µm
P4VBA100	Resistance (R/ Ω)	%RH					
		60	7.7×10^{12}	2.2×10^{8}		4.1×10^{8}	9.5×10^{8}
		80	4.2×10^{11}	2.1×10^{7}		5.3×10^{7}	1.3×10^{8}
		90	7.5×10^{10}	3.1×10^{6}		1.9×10^{7}	4.7×10^{7}
		95	1.8×10^{10}	1.1×10^{6}		3.8×10^{6}	1.7×10^{7}
	Log (σ/ S cm^{-1})	%RH					
		60	-7.8	-7.9		-7.9	-8.0
		80	-6.5	-6.9		-7.0	-7.1
		90	-5.8	-6.1		-6.6	-6.7
		95	-5.2	-5.6		-5.9	-6.2
	Log (R'/ Ω)	%RH					
		60	12.9	13.1		13.0	13.0
		80	11.7	12.3		12.1	12.0
		90	10.9	11.8		11.6	11.1
		95	10.3	11.4		10.9	10.7
PS4VBA33	Resistance (R/ Ω)	%RH					
		60	6.0×10^{12}	1.7×10^{9}*	6.1×10^{8}**	1.7×10^{9}	5.5×10^{9}
		80	2.2×10^{11}	1.2×10^{8}*	7.8×10^{7}**	3.0×10^{8}	5.7×10^{8}
		90	4.6×10^{10}	5.6×10^{8}*	2.3×10^{7}**	1.1×10^{8}	2.0×10^{8}
		95	1.2×10^{10}	1.0×10^{7}*	9.1×10^{6}**	4.2×10^{7}	9.7×10^{7}
	Log (σ/ S cm^{-1})	%RH					
		60	-7.6	-8.8*	-8.8**	-8.6	-8.8
		80	-6.2	-7.9*	-7.9**	-7.8	-7.8
		90	-5.5	-7.3*	-7.4**	-7.4	-7.3
		95	-5.0	-7.0*	-7.0**	-7.0	-7.0
	Log (R'/ Ω)	%RH					
		60	12.8	13.8*	13.4**	13.6	13.9
		80	11.4	13.0*	12.5**	12.8	12.9
		90	10.7	12.3*	12.0**	12.4	12.5
		95	10.1	12.1*	11.6**	12.0	12.1

4.4 Conclusions

The devices with highly long electrodes length and short channel lengths of a few microns were successfully fabricated for the electrical properties' investigation of low proton conductivity polymer thin film. The Au-deposited electrodes were designed as comb-shaped with around 22 cm long. The channel length or the distance between the two electrodes was varied from 5 to 15 μm. The electrical properties of the fabricated weak-acid functionalized styrene-based copolymer thin film, P4VBA100 and PS4VBA33, on CFETs were investigated using AC-impedance measurement. The Nyquist plots of polymer thin film on all CFETs clearly show a semicircle response of proton conduction in polymer thin film and a tail response of the capacitance. The RH dependence of semicircle response was also observed, confirmed that the obtain impedance response was derived from the polymer thin film and did not dominate by the double layer capacitance, as included in Chapter 3. Thus, these CFETs overcome the drawbacks of dominated double layer capacitance response and the short circuit between two electrodes through the thin dielectric layer in the AC-impedance measurement method.

Furthermore, the influence of CFET's channel length was investigated. The CFET with the shortest channel length of 5 μm provides the lowest polymer thin film's resistance, consistent with the assumption from the proton conductivity equation. This difference in proton conductivity and normalized resistance of the films on quartz and CFETs might cause by the different water adsorption abilities on the surface of the substrates. The film with interfacial proton conduction shifted to internal proton conduction due to the poor water adsorption ability at the film/ substrate surface interface region. In conclusion, the CFETs were successfully prepared and used for the electrical properties' investigation of relatively low proton conductivity using AC-impedance measurement and Au electrodes.

References

(1) Leem, H.; Dorbandt, I.; Rojas-Chapana, J.; Fiechter, S.; Tributsch, H. Bio-Analogue Amino Acid-Based Proton-Conduction Wires for Fuel Cell Membranes. *J. Phys. Chem. C* **2008**, *112* (7), 2756–2763. https://doi.org/10.1021/jp077547l.

(2) Wu, H.; Cao, Y.; Shen, X.; Li, Z.; Xu, T.; Jiang, Z. Preparation and Performance of Different Amino Acids Functionalized Titania-Embedded Sulfonated Poly (Ether Ether Ketone) Hybrid Membranes for Direct Methanol Fuel Cells. *J. Memb. Sci.* **2014**, *463*, 134–144. https://doi.org/https://doi.org/10.1016/j.memsci.2014.03.058.

(3) Selberg, J.; Jia, M.; Rolandi, M. Proton Conductivity of Glycosaminoglycans. *PLoS One* **2019**, *14* (3), e0202713. https://doi.org/10.1371/journal.pone.0202713.

(4) Zhong, C.; Deng, Y.; Roudsari, A. F.; Kapetanovic, A.; Anantram, M. P.; Rolandi, M. A Polysaccharide Bioprotonic Field-Effect Transistor. *Nat. Commun.* **2011**, *2* (1), 2–6. https://doi.org/10.1038/ncomms1489.

(5) Deng, Y.; Helms, B. A.; Rolandi, M. Synthesis of Pyridine Chitosan and Its Protonic Conductivity. *J. Polym. Sci. Part A Polym. Chem.* **2015**, *53* (2), 211–214. https://doi.org/10.1002/pola.27430.

(6) Zhong, H.; Wu, G.; Fu, Z.; Lv, H.; Xu, G.; Wang, R. Flexible Porous Organic Polymer Membranes for Protonic Field-Effect Transistors. *Adv. Mater.* **2020**, *32* (21), 1–7. https://doi.org/10.1002/adma.202000730.

(7) Ordinario, D. D.; Phan, L.; Walkup IV, W. G.; Van Dyke, Y.; Leung, E. M.; Nguyen, M.; Smith, A. G.; Kerr, J.; Naeim, M.; Kymissis, I.; et al. Production

and Electrical Characterization of the Reflectin A2 Isoform from Doryteuthis (Loligo) Pealeii. *RSC Adv.* **2016**, *6* (62), 57103–57107. https://doi.org/10.1039/C6RA05405F.

(8) Wünsche, J.; Deng, Y.; Kumar, P.; Di Mauro, E.; Josberger, E.; Sayago, J.; Pezzella, A.; Soavi, F.; Cicoira, F.; Rolandi, M.; et al. Protonic and Electronic Transport in Hydrated Thin Films of the Pigment Eumelanin. *Chem. Mater.* **2015**, *27* (2), 436–442. https://doi.org/10.1021/cm502939r.

(9) Ordinario, D. D.; Phan, L.; Walkup IV, W. G.; Jocson, J.-M.; Karshalev, E.; Hüsken, N.; Gorodetsky, A. A. Bulk Protonic Conductivity in a Cephalopod Structural Protein. *Nat. Chem.* **2014**, *6* (7), 596–602. https://doi.org/10.1038/nchem.1960.

(10) Meredith, P.; Tandy, K.; Mostert, A. Organic Electronics. Wiley-VCH Verlag GmbH & Co. KGaA, Weinheim 2013.

(11) Amdursky, N.; Wang, X.; Meredith, P.; Bradley, D. D. C.; Stevens, M. M. Long-Range Proton Conduction across Free-Standing Serum Albumin Mats. *Adv. Mater.* **2016**, *28* (14), 2692–2698. https://doi.org/10.1002/adma.201505337.

(12) Lee, W.-K.; Pietron, J. J.; Kidwell, D. A.; Robinson, J. T.; McGann, C. L.; Sheehan, P. E.; Mulvaney, S. P. Enhanced Protonic Conductivity and IFET Behavior in Individual Proton-Doped Electrospun Chitosan Fibers. *J. Mater. Chem. C* **2019**, *7* (35), 10833–10840. https://doi.org/10.1039/C9TC02452B.

(13) Deng, Y.; Josberger, E.; Jin, J.; Rousdari, A. F.; Helms, B. A.; Zhong, C.; Anantram, M. P.; Rolandi, M. H + -Type and OH - -Type Biological Protonic Semiconductors and Complementary Devices. *Sci. Rep.* **2013**, *3*. https://doi.org/10.1038/srep02481.

(14) Wu, G. D.; Zhou, H. L.; Fu, Z. H.; Li, W. H.; Xiu, J. W.; Yao, M. S.; Li, Q. hong; Xu, G. MOF Nanosheet Reconstructed Two-Dimensional Bionic Nanochannel for Protonic Field-Effect Transistors. *Angew. Chemie - Int. Ed.* **2021**. https://doi.org/10.1002/anie.202100356.

(15) Sone, Y.; Ekdunge, P.; Simonsson, D. Proton Conductivity of Nafion 117 as Measured by a Four-Electrode AC Impedance Method. *J. Electrochem. Soc.* **1996**, *143* (4), 1254–1259. https://doi.org/10.1149/1.1836625.

(16) Mondal, S.; Agam, Y.; Amdursky, N. Enhanced Proton Conductivity across Protein Biopolymers Mediated by Doped Carbon Nanoparticles. *Small* **2020**, *2005526* (16), 2005526. https://doi.org/10.1002/smll.202005526.

(17) Mondal, S.; Agam, Y.; Nandi, R.; Amdursky, N. Exploring Long-Range Proton Conduction, the Conduction Mechanism and Inner Hydration State of Protein Biopolymers. *Chem. Sci.* **2020**, *11* (13), 3547–3556. https://doi.org/10.1039/c9sc04392f.

(18) Ordinario, D. D.; Phan, L.; Van Dyke, Y.; Nguyen, T.; Smith, A. G.; Nguyen, M.; Mofid, N. M.; Dao, M. K.; Gorodetsky, A. A. Photochemical Doping of Protonic Transistors from a Cephalopod Protein. *Chem. Mater.* **2016**, *28* (11), 3703–3710. https://doi.org/10.1021/acs.chemmater.6b00336.

(19) Choi, J. H.; Xie, W.; Gu, Y.; Frisbie, C. D.; Lodge, T. P. Single Ion Conducting, Polymerized Ionic Liquid Triblock Copolymer Films: High Capacitance Electrolyte Gates for N-Type Transistors. *ACS Appl. Mater. Interfaces* **2015**, *7* (13), 7294–7302. https://doi.org/10.1021/acsami.5b00495.

(20) Kumari, N.; Pandey, M.; Nagamatsu, S.; Nakamura, M.; Pandey, S. S. Investigation and Control of Charge Transport Anisotropy in Highly Oriented

Friction-Transferred Polythiophene Thin Films. *ACS Appl. Mater. Interfaces* **2020**, *12* (10), 11876–11883. https://doi.org/10.1021/acsami.9b23345.

(21) Kim, D.; Zhu, H.; Liu, A.; Kim, H. S.; Noh, Y. Y.; Hwang, D. H. Highly Ambient-Stable Organic Thin-Film Transistors Fabricated Using Naphthalene Diimide and Thienylene-Vinylene-Thienylene-Based n-Type Polymers with Different Electron-Withdrawing Groups. *J. Phys. Chem. C* **2020**, *124* (38), 20784–20793. https://doi.org/10.1021/acs.jpcc.0c06531.

(22) Nagao, Y.; Kubo, T. Surface Proton Transport of Fully Protonated Poly(Aspartic Acid) Thin Films on Quartz Substrates. *Appl. Surf. Sci.* **2014**, *323*, 19–24. https://doi.org/10.1016/j.apsusc.2014.06.085.

(23) Agam, Y.; Nandi, R.; Bulava, T.; Amdursky, N. The Role of the Protein–Water Interface in Dictating Proton Conduction across Protein-Based Biopolymers. *Mater. Adv.* **2021**, *2* (5), 1739–1746. https://doi.org/10.1039/d0ma00951b.

(24) Paul, D. K.; McCreery, R.; Karan, K. Proton Transport Property in Supported Nafion Nanothin Films by Electrochemical Impedance Spectroscopy. *J. Electrochem. Soc.* **2014**, *161* (14), F1395–F1402. https://doi.org/10.1149/2.0571414jes.

(25) Halim, J.; Büchi, F. N.; Haas, O.; Stamm, M.; Scherer, G. G. Characterization of Perfluorosulfonic Acid Membranes by Conductivity Measurements and Small-Angle x-Ray Scattering. *Electrochim. Acta* **1994**, *39* (8), 1303–1307. https://doi.org/10.1016/0013-4686(94)E0051-Z.

(26) Slade, S.; Campbell, S. A.; Ralph, T. R.; Walsh, F. C. Ionic Conductivity of an Extruded Nafion 1100 EW Series of Membranes. *J. Electrochem. Soc.* **2002**, *149* (12), A1556. https://doi.org/10.1149/1.1517281.

(27) Soboleva, T.; Xie, Z.; Shi, Z.; Tsang, E.; Navessin, T.; Holdcroft, S. Investigation of the Through-Plane Impedance Technique for Evaluation of Anisotropy of Proton Conducting Polymer Membranes. *J. Electroanal. Chem.* **2008**, *622* (2), 145–152. https://doi.org/10.1016/j.jelechem.2008.05.017.

(28) Yadav, R.; Fedkiw, P. S. Analysis of EIS Technique and Nafion 117 Conductivity as a Function of Temperature and Relative Humidity. *J. Electrochem. Soc.* **2012**, *159* (3), B340–B346. https://doi.org/10.1149/2.104203jes.

(29) Nadia E, T.; Roya, M.; Mohammad, S. Three-Dimensional Impedance-Based Sensors for Detection of Chemicals in Aqueous Solutions. *Int. J. Anal. Bioanal. Methods* **2020**, *2* (1). https://doi.org/10.35840/ijabm/2412.

(30) Krishnan, K.; Iwatsuki, H.; Hara, M.; Nagano, S.; Nagao, Y. Influence of Molecular Weight on Molecular Ordering and Proton Transport in Organized Sulfonated Polyimide Thin Films. *J. Phys. Chem. C* **2015**, *119* (38), 21767–21774. https://doi.org/10.1021/acs.jpcc.5b03292.

(31) Nagao, Y.; Enta, A.; Suwansoontorn, A.; Ono, Y. Proton Conductivity and Oriented Structure of Nafion Thin Films on the Au-Deposited Surface and MgO Substrate. *ECS Trans.* **2018**, *88* (1), 249–258. https://doi.org/10.1149/08801.0249ecst.

(32) Ono, Y.; Nagao, Y. Interfacial Structure and Proton Conductivity of Nafion at the Pt-Deposited Surface. *Langmuir* **2016**, *32* (1), 352–358. https://doi.org/10.1021/acs.langmuir.5b02623.

Chapter 5

General conclusion and future prospects

5.1 General conclusion

First, several St-based copolymers with various carboxylic acid concentrations were successfully synthesized. Then, ^{1}H-NMR, TGA, FTIR, and XPS were applied to verify polymer and thin film's various carboxylic acid concentrations. The IR pMAIR spectra of the polymer thin films provide both free and cyclic dimer carboxylic acid groups. The polymer thin film with a higher concentration of carboxylic acid group had a larger ratio of free carboxylic acid groups to dimers, allowing for more hydrogen bonding networks. The water uptake measurements show a similar quantity of adsorbed water molecules per carboxylic acid group in all thin films. The impedance spectroscopy examined the in-plane proton transport and the normalized interfacial resistance (*R*') of polymer thin film to explore the interfacial proton transport. Thin films with higher carboxylic acid concentrations and a larger ratio of free carboxylic acid groups to dimers were discovered to have internal proton transport. On the other hand, interfacial proton transport was found in lower carboxylic acid concentration films with more free carboxylic acid groups positioned at the interfaces. The above results provide that the polymers' carboxylic acid concentration influences films' proton transport behavior.

Second, the electrical properties of the fabricated carboxylic acid functionalized styrene-based copolymer thin film on the devices with the parallel-shaped channel, PFETs, were investigated using gold (Au) electrodes and AC-impedance measurement. The electrode reaction can be prevented using this measurement method. The Nyquist plots of polymer thin film on the PFETs response were dominated by the Au electrodes/ polymer thin film interfacial double layer capacitance due to the relatively low proton conductivity of the fabricated thin film. In addition, the PFET with a short channel length and wide channel width tends to provide a slightly better RH dependence impedance response. Therefore, the reduction of channel

length and the extension of the channel width or electrode length were expected to reduce the polymer thin film's resistance.

Lastly, the electrical properties of fabricated low proton conductivity polymer thin film were successfully investigated using the highly long electrodes and short channel length devices and AC-impedance measurement. The semicircle and RH dependence impedance response confirm the electrical properties of both internal and interfacial proton conductive polymer thin films without being dominated by double-layer capacitance. In addition, the resistance of the electrode and gate electrode was examined. This study overcomes the drawback of dominating double-layer capacitance response and the short circuit between two electrodes through the thin dielectric layer in the AC-impedance measurement method. The CFET with the shortest channel length provides the lowest polymer thin film's resistance. The substrate surface strongly affects the proton transport properties of the films since the differences in conductivity and normalized resistance were observed between quartz and CFET substrate. However, CFETs were successfully used for the electrical properties' investigation of relatively low proton conductivity using AC-impedance measurement and Au electrodes.

5.2 Future prospects

The results and new findings in this research can provide more opportunities to study various related topics.

First is the investigation of proton conductivity control in carboxylic acid-containing polymer thin films modulated by a field-effect transistor (FETs). Our fabricated copolymer can be applied with our comb-shaped FETs (CFETs). The charge carrier density of the polymer thin film may be modulated through the different external gate voltage (V_G) applying. With the gold electrodes and AC-impedance methods, the electrical properties of polymer thin film when the V_G was applying can be investigated without the effect of palladium (Pd) electrode reaction.

Another related topic is the influence of carboxylic acid group concentration of polymer thin film on the electrical properties of FETs. Many parameters, such as carrier density and mobility, affect the FET's performance. Also, the number of proton donors significantly affects polymer thin film's charge carrier density and mobility. The applied V_G may differently modulate the number of proton carriers in polymer thin film with various carboxylic acid concentrations. Therefore, the influence of different carboxylic acid group concentrations in the synthesized polymer thin films on the CFET's electrical properties is challenging.

Acknowledgments

I would like to express my sincere gratitude to my Ph.D. supervisor, Associate Professor Yuki Nagao of Japan Advanced Institute of Science and Technology (JAIST), for his valuable guidance, appropriate suggestions and kind encouragement, and great support during my doctoral study. During my study, all of my achievements would not be possible without his creative mind and his enthusiastic guidance.

I express my sincere gratitude to Professor Yuzuru Takamura and Assistant Professor Daisuke Hirose of JAIST for their valuable guidance, meaningful suggestions, and crucial support in providing materials and instruments for this study and minor research.

I also profoundly acknowledge Associate Professor Katsuhiro Yamamoto of Nagoya Institute of Technology, Professor Shusaku Nagano of Rikkyo University, and Professor Jun Matsui of Yamagata University for all appreciate comments and suggestions.

I express my thanks to Professor Tatsuo Kaneko of JAIST for being my second supervisor and for his valuable guidance in this study.

I would like to express my appreciation to my referees, Professor Kazuaki Matsumura, Professor Noriyoshi Matsumi, Associate Professor Eijiro Miyako of JAIST, and Professor Kazuhiko Matsumoto of Osaka University, for their valuable suggestions and comments.

I would like to thank the former and present students of Nagao laboratory for their kind support and beneficial discussion with me.

Finally, I profoundly appreciate the support and encouragement from my family, all of my friends, and colleagues.

Athchaya Suwansoontorn

September 2021

Ishikawa, JAPAN

Achievements

Research Publications

1. Athchaya Suwansoontorn, Katsuhiro Yamamoto, Shusaku Nagano, Jun Matsui, Yuki Nagao, “Interfacial and Internal Proton Conduction of Weak-acid Functionalized Styrene-based Copolymer with Various Carboxylic Acid Concentrations”, *Electrochemistry*, **2021**, http://dx.doi.org/10.5796/electrochemistry.21-00042. [*Accepted*]

Other Research Publications

1. Yuki Nagao, Aoi Enta, Athchaya Suwansoontorn, Yutaro Ono, “Proton Conductivity and Oriented Structure of Nafion Thin Films on the Au-deposited Surface and MgO Substrate”, *ECS Trans*., **2018**, *88*, 249-258.

2. Zhongping Li, Yuze Yao, Dongjin Wang, Md. Mahmudul Hasan, Athchaya Suwansoontorn, Yuki Nagao, “Simple and universal synthesis of sulfonated porous organic polymers with high proton conductivity”, *Mater. Chem. Front.*, **2020**, *4*, 2339 - 2345.

3. Zhongping Li, He Li, Dongjin Wang, Athchaya Suwansoontorn, Gang Du, Zhaohan Liu, Md. Mahmudul Hasan, Yuki Nagao, “A simple and cost-effective synthesis of ionic porous organic polymers with excellent porosity for high iodine capture” *Polymer*, **2020**, *204*, 122796(1-7).

4. Zhongping Li, Zhaohan Liu, He Li, Md. Mahmudul Hasan, Athchaya Suwansoontorn, Gang Du, Dongjin Wang, Yuwei Zhang, Yuki Nagao, “Sulfonated Triazine-Based Porous Organic Polymer for Excellent Proton Conductivity” *ACS Appl. Polym. Mater.*, **2020**, *2*, 3267 - 3273.

Conferences

Poster Presentation

1. Athchaya Suwansoontorn and Yuki Nagao, “Positive effects of modified quartz substrates on proton transport in Nafion thin films”, JAIST Japan-India Symposium on Advanced Science 2019, Nomi-shi, Ishikawa, Japan, 7 March 2019.

2. Athchaya Suwansoontorn, Aoi Enta, Yuki Nagao, “Proton Conductivity and Oriented Structure of Nafion Thin Films on the Au-deposited Surface and MgO Substrate”, 68th Symposium on Macromolecules (68th SPSJ), Fukui-shi, Fukui, Japan, 25-27 September 2019.

Abstract of minor research

Biosensors attracted the attention of researchers for use in many applications. Containing nucleic acid biosensor can be used as a high specific sensor for biochemical species due to hybridization events of the target fragments and probe fragments. The use of an amine-functionalized surface is one of the methods to immobilized DNA probes on the biosensor surfaces. The density of DNA probes at the biosensor surface needs to be considered because the efficiency of the hybridization event depends on the number of DNA probes. However, too crowded with DNA probes will hinder the hybridization event. In this study, the effect of different DNA probe ratio between short- and long-chain DNA on DNA probe density and DNA hybridization event were investigated. The surface morphology and electrical response of prepared DNA-based FET biosensor devices was observed. However, the electronic response after the DNA hybridization event was barely changed. Therefore, the DNA immobilization and hybridization techniques significantly affect the performance of the devices and need to be improve.

Keywords: FET; biosensors; DNA hybridization; DNA immobilization